NASA/CR–2001–210761

Application of TURBO-AE to Flutter Prediction

Aeroelastic Code Development

Daniel Hoyniak, Todd A. Simons
Rolls-Royce, Indianapolis, Indiana

May 2001

The NASA STI Program Office . . . in Profile

Since its founding, NASA has been dedicated to the advancement of aeronautics and space science. The NASA Scientific and Technical Information (STI) Program Office plays a key part in helping NASA maintain this important role.

The NASA STI Program Office is operated by Langley Research Center, the Lead Center for NASA's scientific and technical information. The NASA STI Program Office provides access to the NASA STI Database, the largest collection of aeronautical and space science STI in the world. The Program Office is also NASA's institutional mechanism for disseminating the results of its research and development activities. These results are published by NASA in the NASA STI Report Series, which includes the following report types:

- TECHNICAL PUBLICATION. Reports of completed research or a major significant phase of research that present the results of NASA programs and include extensive data or theoretical analysis. Includes compilations of significant scientific and technical data and information deemed to be of continuing reference value. NASA's counterpart of peer-reviewed formal professional papers but has less stringent limitations on manuscript length and extent of graphic presentations.

- TECHNICAL MEMORANDUM. Scientific and technical findings that are preliminary or of specialized interest, e.g., quick release reports, working papers, and bibliographies that contain minimal annotation. Does not contain extensive analysis.

- CONTRACTOR REPORT. Scientific and technical findings by NASA-sponsored contractors and grantees.

- CONFERENCE PUBLICATION. Collected papers from scientific and technical conferences, symposia, seminars, or other meetings sponsored or cosponsored by NASA.

- SPECIAL PUBLICATION. Scientific, technical, or historical information from NASA programs, projects, and missions, often concerned with subjects having substantial public interest.

- TECHNICAL TRANSLATION. English-language translations of foreign scientific and technical material pertinent to NASA's mission.

Specialized services that complement the STI Program Office's diverse offerings include creating custom thesauri, building customized data bases, organizing and publishing research results . . . even providing videos.

For more information about the NASA STI Program Office, see the following:

- Access the NASA STI Program Home Page at ***http://www.sti.nasa.gov***

- E-mail your question via the Internet to help@sti.nasa.gov

- Fax your question to the NASA Access Help Desk at 301–621–0134

- Telephone the NASA Access Help Desk at 301–621–0390

- Write to:
  NASA Access Help Desk
  NASA Center for AeroSpace Information
  7121 Standard Drive
  Hanover, MD 21076

NASA/CR–2001–210761

Application of TURBO-AE to Flutter Prediction

Aeroelastic Code Development

Daniel Hoyniak, Todd A. Simons
Rolls-Royce, Indianapolis, Indiana

Prepared under Contract NAS3-27725 Task 6
EDR-19540

National Aeronautics and
Space Administration

Glenn Research Center

May 2001

Trade names or manufacturers' names are used in this report for identification only. This usage does not constitute an official endorsement, either expressed or implied, by the National Aeronautics and Space Administration.

Available from

NASA Center for Aerospace Information
7121 Standard Drive
Hanover, MD 21076
Price Code: A06

National Technical Information Service
5285 Port Royal Road
Springfield, VA 22100
Price Code: A06

Available electronically at http://gltrs.grc.nasa.gov/GLTRS

Contents

1 SUMMARY 1

2 INTRODUCTION 3

3 Experimental Facilities 5
- 3.1 Linear Cascade . . . 5
- 3.2 TF41-A100 Test Rig . . . 7

4 Computational Algorithms 9
- 4.1 Nonlinear Euler/Navier-Stokes Model, *TURBO-AE* . . . 9
- 4.2 Linear Navier-Stokes Model, *LNS2D* . . . 10
- 4.3 Linearized Euler Model, *SLiQ* . . . 10

5 Task 1: Compressor Cascade 11
- 5.1 Pressure Ratio of 1.04 . . . 12
  - 5.1.1 Steady Flow . . . 12
  - 5.1.2 Unsteady Flow . . . 15
- 5.2 Pressure Ratio of 1.45 . . . 22
  - 5.2.1 Steady Flow . . . 22
  - 5.2.2 Unsteady Flow . . . 22
- 5.3 Unsteady Aerodynamic Work . . . 24
- 5.4 Conclusions . . . 24

6 Task 2: Turbine Cascade 32
- 6.1 Expansion Ratio of 1.531 . . . 32
  - 6.1.1 Steady Flow . . . 32
  - 6.1.2 Unsteady Flow . . . 35
- 6.2 Expansion Ratio of 2.713 . . . 41
  - 6.2.1 Steady Flow . . . 41
  - 6.2.2 Unsteady Flow . . . 48
- 6.3 Aerodynamic Damping . . . 51
- 6.4 Conclusions . . . 56

7 Task 3: Transonic Fan 58
- 7.1 Steady Flow: Flutter Point . . . 59

7.2 Unsteady Flow: Flutter Point 68
7.2.1 Unsteady Aerodynamic Work 68
7.2.2 Time Mean Behavior 69
7.2.3 Unsteady Harmonic Response 71
7.3 Conclusions 74

List of Figures

3.1 Schematic of linear cascade facility showing the turbine test section. 6

3.2 Schematic of linear cascade facility showing the compressor test section. 6

3.3 Cross section of TF41-A100 test rig. 8

5.1 H-mesh used in *TURBO-AE* analysis of compressor cascade. 13

5.2 Multiblocked H-O-H mesh used in *LNS2D* analysis of compressor cascade. . . . 13

5.3 Comparison of steady blade surface pressure predictions from *TURBO-AE* , *LNS2D*, and *ADPAC*with measurements for a static pressure ratio of 1.04. . . . 14

5.4 Steady Mach contours obtained from *LNS2D* for a static pressure ratio of 1.04. 14

5.5 Comparison of unsteady blade surface pressure magnitude and phase predictions from, *LNS2D*, with measurements for a static pressure ratio of 1.04, a torsion mode oscillation at 725 Hz and an interblade phase angle of -30 degrees. . . . 16

5.6 Comparison of unsteady blade surface pressure magnitude and phase predictions from, *LNS2D*, with measurements for a static pressure ratio of 1.04, a torsion mode oscillation at 725 Hz and an interblade phase angle of -50 degrees. . . . 17

5.7 Comparison of unsteady blade surface pressure magnitude and phase predictions from, *LNS2D*, with measurements for a static pressure ratio of 1.04, a torsion mode oscillation at 725 Hz and an interblade phase angle of -90 degrees. . . . 18

5.8 Comparison of unsteady blade surface pressure magnitude and phase predictions from, *LNS2D*, with measurements for a static pressure ratio of 1.04, a torsion mode oscillation at 725 Hz and an interblade phase angle of 0 degrees. 19

5.9 Comparison of unsteady blade surface pressure magnitude and phase predictions from, *LNS2D*, with measurements for a static pressure ratio of 1.04, a torsion mode oscillation at 725 Hz and an interblade phase angle of 80 degrees. 20

5.10 Comparison of unsteady blade surface pressure magnitude and phase predictions from, *LNS2D*, with measurements for a static pressure ratio of 1.04, a torsion mode oscillation at 725 Hz and an interblade phase angle of 180 degrees. . . . 21

5.11 Comparison of steady blade surface pressure predictions with measurements for the 1.45 pressure ratio compressor cascade. 23

5.12 *LNS2D* predicted Mach number contours for the 1.45 pressure ratio compressor cascade. 23

5.13 Blade surface unsteady pressure distribution, magnitude (*top*), and phase (*bottom*) compared to measurements for the 1.45 pressure ratio compressor cascade vibrating in a torsion mode at 725Hz and an interblade phase angle of -170 degrees. The predictions were made using *LNS2D*. 25

5.14 Blade surface unsteady pressure distribution, magnitude (*top*), and phase (*bottom*) compared to measurements for the 1.45 pressure ratio compressor cascade vibrating in a torsion mode at 725Hz and an interblade phase angle of -65 degrees. The predictions were made using *LNS2D*. 26

5.15 Blade surface unsteady pressure distribution, magnitude (*top*), and phase (*bottom*) compared to measurements for the 1.45 pressure ratio compressor cascade vibrating in a torsion mode at 725Hz and an interblade phase angle of 0 degrees. The predictions were made using *LNS2D*. 27

5.16 Blade surface unsteady pressure distribution, magnitude (*top*), and phase (*bottom*) compared to measurements for the 1.45 pressure ratio compressor cascade vibrating in a torsion mode at 725Hz and an interblade phase angle of 60 degrees. The predictions were made using *LNS2D*. 28

5.17 Blade surface unsteady pressure distribution, magnitude (*top*), and phase (*bottom*) compared to measurements for the 1.45 pressure ratio compressor cascade vibrating in a torsion mode at 725Hz and an interblade phase angle of 85 degrees. The predictions were made using *LNS2D*. 29

5.18 Predicted unsteady aerodynamic work per cycle for the compressor cascade. . . 30

6.1 Typical single block, H mesh used in *TURBO-AE* analysis of high turning turbine cascade analysis (*single, constant radius plane shown for clarity*). 33

6.2 Typical multiblocked, H-O-H mesh used in *LNS2D* analysis of high turning turbine cascade analysis (*multiple passages shown for clarity*). 34

6.3 Steady blade loading predicted by *TURBO-AE* using both the old (reflecting) and new nonreflecting far-field boundary conditions. 35

6.4 Convergence history of the *TURBO-AE* predictions for the 1.531 expansion ratio. 36

6.5 Comparison of steady blade loading predicted by *TURBO-AE* and *LNS2D* with measurements for the 1.531 expansion ratio flow. 37

6.6 Comparison of viscous and inviscid *TURBO-AE* predictions for the 1.531 expansion ratio case. 37

6.7 Comparison of measured and predicted unsteady pressure response for the turbine cascade vibration in a torsional mode at 340 Hz, 0 degree interblade phase angle, and 1.531 expansion ratio. 39

6.8 Comparison of measured and predicted unsteady pressure response for the turbine cascade vibration in a torsional mode at 340 Hz, 180 degree interblade phase angle, and 1.531 expansion ratio. 40

6.9 Comparison of measured and predicted unsteady pressure response for the turbine cascade vibration in a torsional mode at 340 Hz, 45 degree interblade phase angle, and 1.531 expansion ratio. 42

6.10 Comparison of measured and predicted unsteady pressure response for the turbine cascade vibration in a torsional mode at 340 Hz, -45 degree interblade phase angle, and 1.531 expansion ratio. 43

6.11 Comparison of measured and predicted unsteady pressure response for the turbine cascade vibration in a torsional mode at 340 Hz, 90 degree interblade phase angle, and 1.531 expansion ratio. 44

6.12 Comparison of measured and predicted unsteady pressure response for the turbine cascade vibration in a torsional mode at 340 Hz, -90 degree interblade phase angle, and 1.531 expansion ratio. 45

6.13 Comparison of steady blade loading as a function of axial chord lengeh, Cax, predicted by *TURBO-AE* and *LNS2D* with measurements for the 2.713 expansion ratio flow. 46

6.14 Steady Mach number contours obtained from the *TURBO-AE* solution for the 2.713 expansion ratio. 46

6.15 Convergence history for the *TURBO-AE* solution, 2.713 expansion ratio. 47

6.16 Comparison of blade surface unsteady response predictions obtained from *TURBO-AE* and *LNS2D* with measurements for a torsional oscillation at 340 Hz, and an interblade phase angle of 0 degrees, and 2.713 expansion ratio. 49

6.17 Comparison of blade surface unsteady response predictions obtained from *TURBO-AE* and *LNS2D* with measurements for a torsional oscillation at 340 Hz, and an interblade phase angle of 180 degrees, and 2.713 expansion ratio. 50

6.18 Comparison of blade surface unsteady response predictions obtained from *TURBO-AE* and *LNS2D* with measurements for a torsional oscillation at 340 Hz, and an interblade phase angle of 45 degrees, and 2.713 expansion ratio. 52

6.19 Comparison of blade surface unsteady response predictions obtained from *TURBO-AE* and *LNS2D* with measurements for a torsional oscillation at 340 Hz, and an interblade phase angle of -45 degrees, and 2.713 expansion ratio. 53

6.20 Comparison of blade surface unsteady response predictions obtained from *TURBO-AE* and *LNS2D* with measurements for a torsional oscillation at 340 Hz, and an interblade phase angle of 90 degrees, and 2.713 expansion ratio. 54

6.21 Comparison of blade surface unsteady response predictions obtained from *TURBO-AE* and *LNS2D* with measurements for a torsional oscillation at 340 Hz, and an interblade phase angle of -90 degrees, and 2.713 expansion ratio. 55

6.22 Unsteady aerodynamic work-per-cycle prediction for turbine cascade for 1.531 and 2.713 expansion ratios. 56

7.1 Typical single block, H mesh used in steady, inviscid *TURBO-AE* and *ADPAC* analyses of the TF41-A100 first stage fan, only the mesh along the blade surface and a single, constant radius plane at 75% span is shown for clarity. . . 60

7.2 Comparison of the mesh used for the viscous (left) and inviscid (right) steady *ADPAC* analysis of the TF41-A100 first stage fan, only the mesh along the blade suction surface is shown for clarity. 61

7.3 Comparison of predicted 100% speedlines from *ADPAC* and *TURBO-AE* 62

7.4 Comparison of steady blade surface pressure distributions for the 50% span location. Predictions obtained from a viscous *ADPAC*, inviscid *ADPAC*, and inviscid *TURBO-AE* calculations performed at the flutter point. 63

7.5 Comparison of steady blade surface pressure distributions for the 75% span location. Predictions obtained from a viscous *ADPAC*, inviscid *ADPAC*, and inviscid *TURBO-AE* calculations performed at the flutter point. 63

7.6 Comparison of steady blade surface pressure distributions for the 88% span location. Predictions obtained from a viscous *ADPAC*, inviscid *ADPAC*, and inviscid *TURBO-AE* calculations performed at the flutter point. 64

7.7 Comparison of steady Mach number contours for the 50% span location. Predictions obtained from a viscous *ADPAC* and inviscid *TURBO-AE* calculations performed at the flutter point. 65

7.8 Comparison of steady Mach number contours for the 75% span location. Predictions obtained from a viscous *ADPAC* and inviscid *TURBO-AE* calculations performed at the flutter point. 66

7.9 Comparison of steady Mach number contours for the 88% span location. Predictions obtained from a viscous *ADPAC* and inviscid *TURBO-AE* calculations performed at the flutter point. 67

7.10 *TURBO-AE* predicted unsteady aerodynamic work-per-cycle as a function of the number of oscillation cycles, (a) 0, (b) 30, (c) 60, and (d) 90 degrees interblade phase angle. 70

7.11 Comparison of the unsteady aerodynamic work-per-cycle as a function of interblade phase angle. Predictions made using viscous *ADPAC/SLiQ*, inviscid *ADPAC/SLiQ*, and *TURBO-AE* algorithms. 71

7.12 Comparison of the time mean and steady blade surface pressure distributions obtained from *TURBO-AE* at the 50% span location. 72

7.13 Comparison of the time mean and steady blade surface pressure distributions obtained from *TURBO-AE* at the 75% span location. 72

7.14 Comparison of the time mean and steady blade surface pressure distributions obtained from *TURBO-AE* at the 88% span location. 73

7.15 Comparison of the 1^{st} harmonic unsteady blade surface pressure distributions obtained from inviscid *TURBO-AE* , viscous *ADPAC/ SLiQ*, and inviscid *ADPAC/ SLiQ*calculations at the 50% span location, *upper* magnitude, and *lower* phase at an interblade phase angle of 0 degrees. 75

7.16 Comparison of the 1^{st} harmonic unsteady blade surface pressure distributions obtained from inviscid *TURBO-AE* , viscous *ADPAC/ SLiQ*, and inviscid *ADPAC/ SLiQ*calculations at the 75% span location, *upper* magnitude, and *lower* phase at an interblade phase angle of 0 degrees. 76

7.17 Comparison of the 1^{st} harmonic unsteady blade surface pressure distributions obtained from inviscid *TURBO-AE* , viscous *ADPAC/ SLiQ*, and inviscid *ADPAC/ SLiQ*calculations at the 88% span location, *upper* magnitude, and *lower* phase at an interblade phase angle of 0 degrees. 77

7.18 Comparison of the 1^{st} harmonic unsteady blade surface pressure distributions obtained from inviscid *TURBO-AE* , viscous *ADPAC/ SLiQ*, and inviscid *ADPAC/ SLiQ*calculations at the 50% span location, *upper* magnitude, and *lower* phase, at an interblade phase angle of 30 degrees. 78

7.19 Comparison of the 1^{st} harmonic unsteady blade surface pressure distributions obtained from inviscid *TURBO-AE* , viscous *ADPAC/ SLiQ*, and inviscid *ADPAC/ SLiQ*calculations at the 75% span location, *upper* magnitude, and *lower* phase at an interblade phase angle of 30 degrees. 79

7.20 Comparison of the 1^{st} harmonic unsteady blade surface pressure distributions obtained from inviscid *TURBO-AE* , viscous *ADPAC/ SLiQ*, and inviscid *ADPAC/ SLiQ*calculations at the 88% span location, *upper* magnitude, and *lower* phase at an interblade phase angle of 30 degrees. 80

7.21 Comparison of the 1^{st} harmonic unsteady blade surface pressure distributions obtained from inviscid *TURBO-AE* , viscous *ADPAC/ SLiQ*, and inviscid *ADPAC/ SLiQ*calculations at the 50% span location, *upper* magnitude, and *lower* phase, at an interblade phase angle of 60 degrees. 81

7.22 Comparison of the 1^{st} harmonic unsteady blade surface pressure distributions obtained from inviscid *TURBO-AE* , viscous *ADPAC/ SLiQ*, and inviscid *ADPAC/ SLiQ*calculations at the 75% span location, *upper* magnitude, and *lower* phase at an interblade phase angle of 60 degrees. 82

7.23 Comparison of the 1^{st} harmonic unsteady blade surface pressure distributions obtained from inviscid *TURBO-AE* , viscous *ADPAC/ SLiQ*, and inviscid *ADPAC/ SLiQ*calculations at the 88% span location, *upper* magnitude, and *lower* phase at an interblade phase angle of 60 degrees. 83

7.24 2^{nd} harmonic unsteady blade surface pressure distributions obtained from inviscid *TURBO-AE* calculations at the 50% span location, *upper* magnitude, and *lower* phase at an interblade phase angle of 0 degrees. 84

7.25 2^{nd} harmonic unsteady blade surface pressure distributions obtained from inviscid *TURBO-AE* calculations at the 75% span location, *upper* magnitude, and *lower* phase at an interblade phase angle of 0 degrees. 85

7.26 2^{nd} harmonic unsteady blade surface pressure distributions obtained from inviscid *TURBO-AE* calculations at the 88% span location, *upper* magnitude, and *lower* phase at an interblade phase angle of degrees. 86

List of Tables

3.1 Physical parameters for the turbine and compressor cascades. 7

5.1 Compressor cascade test conditions 11

6.1 Turbine cascade test conditions. 32

Chapter 1

SUMMARY

The objective of NASA Contract NAS3-27725 was to evaluate the use of a NASA developed computer program, *TURBO-AE* , for the prediction of turbomachinery blade flutter. The *TURBO-AE* program was to be evaluated by comparison of predictions with cascade and rig data and to predictions made from various in-house programs.

Three sets of experimental data were chosen for the evaluation of *TURBO-AE* . Two of the sets were obtained from a linear cascade, while the third was a fan blade which was tested in a full scale rig. The Cascade data were obtained for two geometries, one representative of the tip section of a high speed fan, and the other the hub section of a high turning turbine blade. The unsteady response of both these blade sections was obtained for a torsional motion over a range of interblade phase angles. The fan blade geometry investigated was the first stage of a three stage fan which exhibited torsion mode flutter near the design point.

Three in-house programs were used in the course of this investigation. The *LNS2D* (Linearized Navier-Stokes, Two Dimensional) code models the 2-D linearized Navier-Stokes equations. The *ADPAC*(Advanced Ducted Propfan Analysis Code) program models the 3-D Navier-Stokes steady and unsteady equations. The *SLiQ*(Steady, Linear,Quadratic) program models the 3-D, Euler, steady, and linearized unsteady equations. The steady solver associated with *SLiQ*was not used in this study. Instead steady flow solutions obtained from *ADPAC*were input to *SLiQ*. If a steady viscous *ADPAC*flow was to be used in *SLiQ*, the boundary layer behavior was first removed.

The steady predictions for the high speed fan cascade showed that for the case in which both the inlet and exit velocity were supersonic the *TURBO-AE* predictions matched those obtained from two in-house codes(*LNS2D ADPAC*). However the predictions did not match the measured blade surface data. As other researchers reported similar disagreement with these data sets, the matter was not investigated further. A second pressure ratio was studied in which the inlet relative flow was supersonic while the exit flow was subsonic. In this case the *TURBO-AE* predictions did not match the other in-house code predictions or the measured data. The in-house code predictions did show a better but not good agreement with the data. Attempts to run unsteady calculations using *TURBO-AE* were not successful.

The turbine cascade results showed the steady *TURBO-AE* predictions were in

agreement with those obtained from the in-house code, *LNS2D*. The unsteady results indicated that the magnitude of the *TURBO-AE* predictions were underpredicted compared to the data and predictions from *LNS2D*. The predicted phase from *TURBO-AE* and the *LNS2D* code showed good agreement with the data in some of the cases studied, but not so good in others. *ADPAC/SLiQ*calculations were not used to analyze the turbine cascade.

The inviscid steady blade loading predictions from *TURBO-AE* for the fan blade were in good agreement with inviscid predictions made from *ADPAC*. No steady, viscous solutions were attempted with *TURBO-AE* . The unsteady work-per-cycle calculations obtained from inviscid *TURBO-AE* and *ADPAC/SLiQ*calculations were used to obtain the work-per-cycle for the torsion mode over a range of interblade phase angles. *TURBO-AE* predicted that the fan would flutter while *ADPAC/SLiQ*did not. The *TURBO-AE* calculations are in agreement with data obtained from the rig which did exhibit a torsion mode flutter behavior.

Chapter 2

INTRODUCTION

Aerodynamically induced vibrations are usually classified into one of two categories: flutter and forced vibration. In flutter, the aerodynamic forces that sustain blade motion are regarded as being dependent solely on that motion, whereas in forced vibration the aerodynamic forces are independent of the motion. In either case, the resulting vibratory motion can lead to fatigue failure. These failures are often associated with a 10% increase in development costs of a new engine and significant direct operating cost (DOC) expenses in revenue operation. With current trends in compressor and turbine designs calling for greater loading, higher speed, increased efficiency, the ability to predict unsteady behavior accurately becomes increasingly important. This is due in part to the fact that the empirical design rules derived from past experiences can no longer be effectively extrapolated into the operating regimes on new designs.

For a complete understanding of unsteady aerodynamic phenomena in turbomachinery, aeroelasticians require accurate and efficient models of the unsteady flow fields resulting from blade motion and incident gusts. Since these flows are, in general, time-dependent, three-dimensional (3-D), compressible and viscous, this is a formidable task. Only recently have the analysis and prediction of 3-D unsteady viscous flows in turbomachinery been treated in the literature. The computer storage and computational time required to accurately resolve the boundary layers adjacent to the airfoil surface and endwalls have made 3-D unsteady viscous calculations prohibitively expensive for routine design applications. Therefore the need exists to develop tools that model the salient features of the unsteady flow field yet remain efficient enough for routine design use.

The focus of NASA Contract NAS3-27725 AOI 6 was to validate recently developed aeroelastic computational fluid dynamics, CFD, algorithms as applied to the design/analysis of turbomachinery blade rows. In pursuit of this objective two paths were pursued concurrently. The first path involves the validation of *TURBO-AE* with relevant test data sets. *TURBO-AE* is envisioned to ultimately have the ability to analyze 3-D unsteady, nonlinear viscous flows in turbomachinery; however, before this analysis can be used with confidence, extensive work must be done to benchmark and validate the code.

The second path involved the continued development and validation of in-house codes. At the core of these codes is a quasi three-dimensional Navier-Stokes analysis. This algorithm is based on linear perturbation theory whereby the unsteady flow field is

considered to be a small harmonic perturbation about a nonlinear mean flow field. In addition, a 3-D unsteady linearized solver referred to as *SLiQ*was examined. The goal of this path was to develop a routine design tool that provides rapid feedback enabling engineers to refine preliminary designs quickly and home in on the optimal configuration.

The following three tasks were designed to achieve the goals outlined above.

Task 1: Compressor Unsteady Pressure Validation The first area of effort applied the codes mentioned above to the prediction of the unsteady interaction of typical compressor/fan geometries. A successful algorithm is one that can accurately model flows over a wide range of operation including subsonic, transonic, and supersonic flow regimes. The presence of adverse pressure gradients also makes the ability to model separated flows necessary. A configuration that requires the modeling of these effects and has accompanying experimental data was selected for this validation effort.

Task 2: Turbine Unsteady Pressure Validation The second area of effort applied the codes mentioned above to the prediction of the unsteady interaction of typical turbine geometries. Again, a configuration that realistically models the operational environment of a modern turbine stage was selected for this validation effort.

Task 3: Compressor Flutter Prediction Application Following the comparative code efforts of Tasks 1 and 2, an analytical study on low pressure (LP) compressor blading was made to determine how well the codes predicted flutter for existing and/or past designs. Comparisons were made detailing the strengths and weaknesses of each approach assessing their utility.

Chapter 3

Experimental Facilities

This chapter presents a brief overview of the experimental facilities which were used to obtain the measurements referenced in this report. These include a linear cascade with two different test sections, one representative of a turbine, and the other a compressor, and a full-scale rig which included a three-stage fan and a two-stage intermediate compressor.

3.1 Linear Cascade

A linear cascade facility was used to obtain the data for both the turbine and compressor geometries addressed in this report. Two different test sections were used, one to model the hub section of a high turning turbine rotor, Figure 3.1, and the other, the tip section of a high speed fan blade, Figure 3.2. A brief description of the cascade configurations and the instrumentation used to acquire the data is presented below. For a more detailed description of the experimental programs, the reader is referred to [1] and [2].

The linear cascade facility was designed to resolve detailed steady and unsteady surface pressure data on turbine and compressor geometries. The facility is a continuous flow, nonreturn, pressure-vacuum type wind tunnel capable of testing turbomachinery blades with very high turning. The main features of the facility are:

- Continuous steady and unsteady operation for extended time periods
- A mechanized test section for changing cascade incidence angle
- A Schlieren optical system for visual observation and photography of the facility in both steady and unsteady operation
- Bleed systems on all four cascade inlet sidewalls
- An instrumentation system capable of controlling and recording both the steady and unsteady operation of the cascade

Two parallel nozzle blocks control the inlet flow. These blocks are adjustable to ensure that the flow is properly channeled through the test section for any inlet flow angle

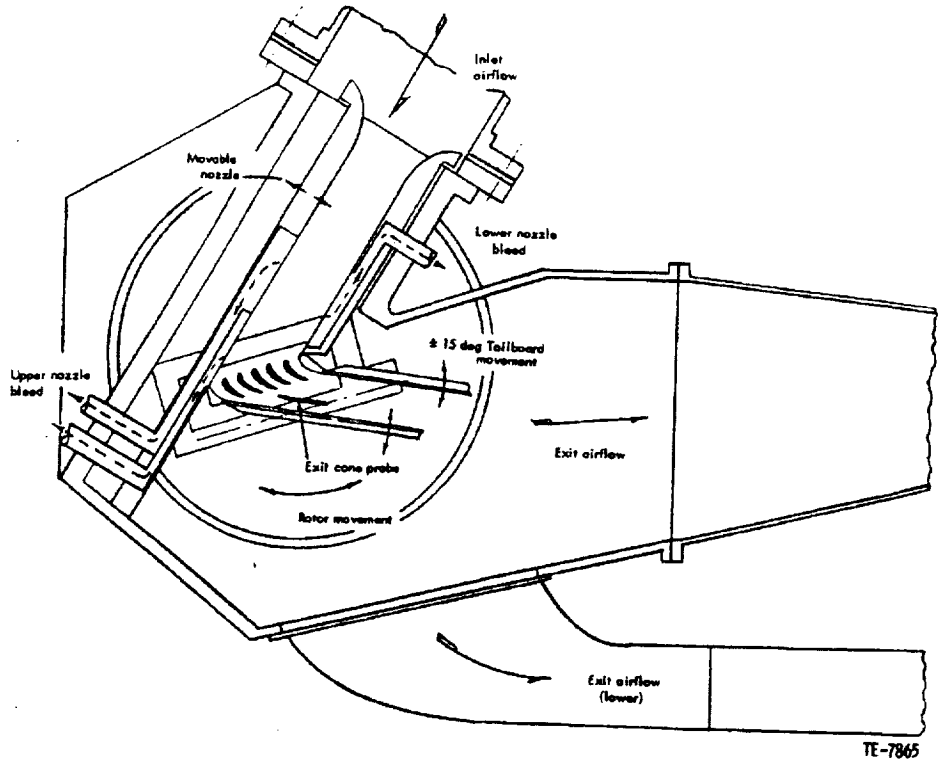

Figure 3.1: Schematic of linear cascade facility showing the turbine test section.

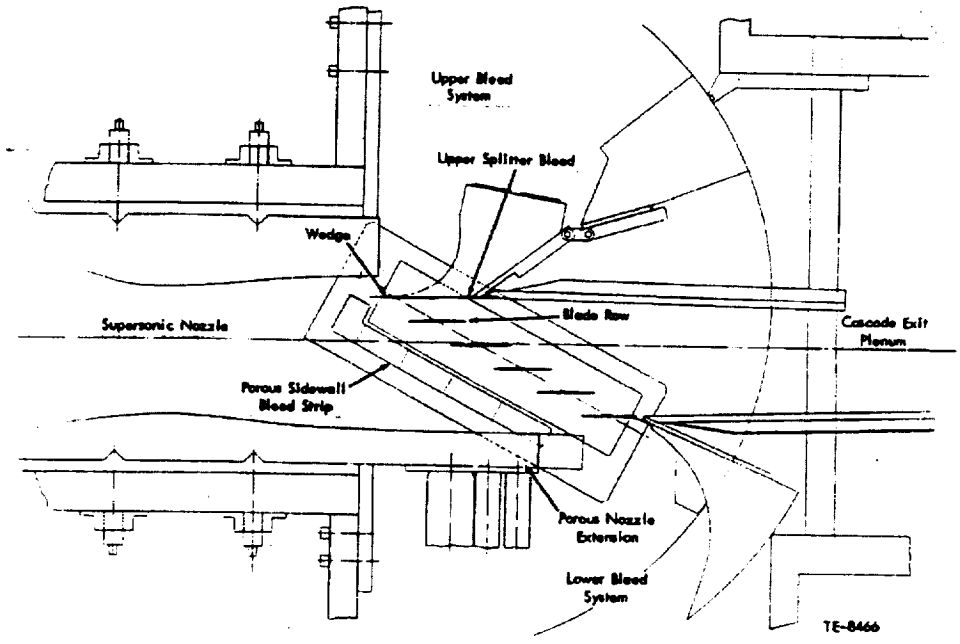

Figure 3.2: Schematic of linear cascade facility showing the compressor test section.

	Turbine	Compressor
Span	3.00 in.	3.00 in.
Chord	2.59 in.	3.00 in.
Solidity	1.891	1.17
Setting Angle	25.5 deg	61.55 deg
Turning	112.0 deg	1.23 deg
Max. Thickness / Chord	0.205	0.034
L.E. Radius / Chord	0.024	0.0026
T.E. Radius / Chord	0.009	0.0026
Axial Chord Projection	2.34 in.	1.43 in.
Torsion Axis Location	35.5 %	50%

Table 3.1: Physical parameters for the turbine and compressor cascades.

desired. In addition, a complex bleed system aids in the establishment of flow periodicity in the test section. Dummy end blades with attached porous tailboards are also incorporated to control the test section periodicity and shock reflection during transonic exit operation. The airfoils are driven in a torsion mode by a spring bar and hammer arrangement attached to each end of the blade. An excitation force is applied to the drive system by electromagnets. Interblade phase angle is controlled by phasing the drive signals provided to each of the electromagnets. A physical description for both the turbine and compressor test sections is given in Table 3.1.

The test section of the cascade is comprised of five airfoil sections. The center blade was changed depending on whether a steady or unsteady test is being performed. While acquiring steady data, the center blade was instrumented with static pressure taps. While acquiring unsteady data, however, the center blade is instrumented with surface mounted Kulite pressure transducers. For the precise locations of the steady and unsteady pressure sensors, as well as for the details of the mounting technique and calibration procedures, see [1] and [2].

3.2 TF41-A100 Test Rig

A cross-sectional view of the TF41-A100 compressor test rig is shown in Figure 3.3. It consists of a three-stage fan and two-stages of an intermediate compressor mounted on a single shaft. The flow path is divided into a by-pass and core flow at the entrance to the intermediate compressor. The fan design features clapperless blades on all three rows. The rig was originally built to study performance characteristics of various fan designs. However, during testing the first-stage fan exhibited flutter in a four nodal diameter mode (57.6 degrees) at its first torsion frequency along the 100% and 105% design corrected speed lines. The flutter occurred just above the nominal working line for both speed lines.

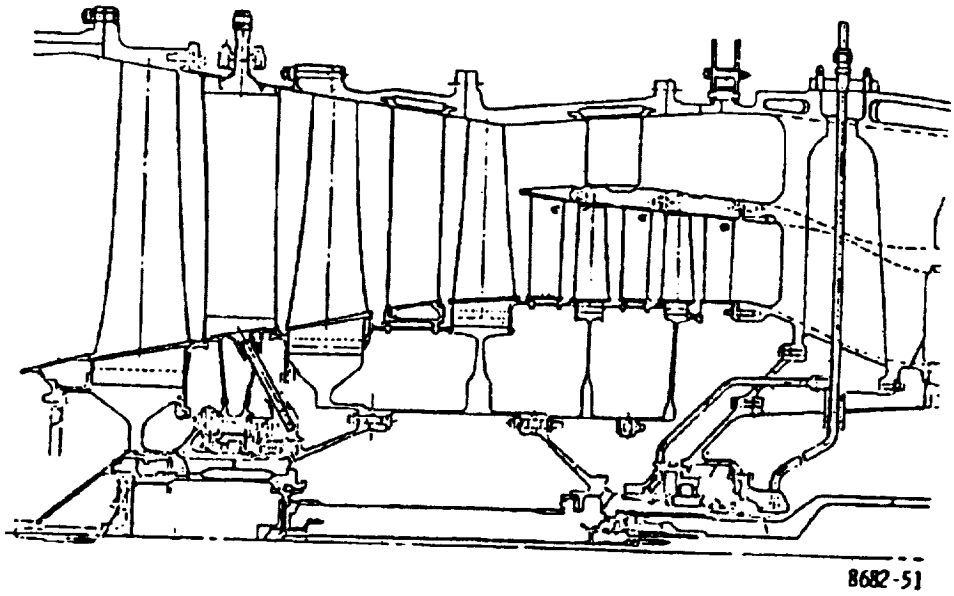

Figure 3.3: Cross section of TF41-A100 test rig.

Chapter 4

Computational Algorithms

Three numerical algorithms capable of unsteady aerodynamic calculations were selected for study as part of this effort. The first is the program referred to as *TURBO-AE* , a fully nonlinear, unsteady model capable of modeling the inviscid, and viscous behavior of multistage turbomachines. The second algorithm, *LNS2D*, models the 2-D, viscous steady and linearized unsteady response of a cascade of airfoils. The final algorithm used is a 3-D linearized unsteady, Euler solver capable of modeling the unsteady response of an isolated blade row. These algorithms are briefly described in the following sections.

4.1 Nonlinear Euler/Navier-Stokes Model, TURBO-AE

The *TURBO*algorithm was developed as part of a long term research effort at Mississippi State University by Janus [3], Chen [4], and Chen and Whitfield [5] to model multistage turbomachinery flows. The algorithm is capable of modeling stationary and rotating blade rows with unequal blade counts. The numerical approach used in this model is based on a finite volume discretization of the 3-D, Reynolds-averaged, thin-layer, Navier-Stokes equations written in terms of a general, time-dependent, curvilinear coordinate system. The resulting system of equations is solved using a flux vector splitting scheme to evaluate the flux Jacobian on the left side, and Roe's flux difference splitting is used to evaluate the fluxes on the right side of the equations, see Janus [3] for details. The resulting system of discretized equations are solved using symmetric Gauss-Sidel iteration together with a Newton sub-iteration approach to maintain the accuracy of the scheme. The Baldwin-Lomax algebraic turbulence model [6] is used to obtain closure of the viscous terms.

The *TURBO*algorithm was modified by Bakhle et al. [7], and [8] to predict the unsteady aerodynamic response of an isolated blade row resulting from a prescribed normal mode representation of the blade vibration. Blade motion is modeled through the use of a moving grid approach. The resulting algorithm is referred to as *TURBO-AE* . Version 4.0 of the *TURBO-AE* program was used in this study. The blade vibration characteristics are determined from the in-vacuum mode shapes and associated frequencies calculated using the in-house finite element program *STRATA*. The *TURBO-AE* program also calculates the unsteady aerodynamic work per cycle which can be related to the

aerodynamic damping acting on the blade. If the aerodynamic damping is negative, the air flow is supplying energy to support blade vibration. If this energy cannot be dissipated by the mechanical and/or material damping of the blade, the vibration can result in a flutter condition. However, if the aerodynamic damping is positive the air flow will act to extract energy from the blade motion and thus act to damp the vibration. The relationship between work per cycle and aerodynamic damping will be discussed in Chapter 6.

4.2 Linear Navier-Stokes Model, LNS2D

The second algorithm chosen for this study is described by Clark [9], it models the unsteady response as a linear perturbation to the steady mean flow. The algorithm which will be referred to as *LNS2D*, (Linearized Navier-Stokes - Two-Dimensional), solves the steady and linearized unsteady two-dimensional Reynolds averaged Navier-Stokes equations for an isolated blade row. Turbulence closure is provided by the Spalart-Allmaras turbulence model [10]. For the present work, the flow is considered to be fully turbulent. The unsteady flow is further assumed to be a small perturbation about a nonlinear steady mean flow. Unsteady calculations are performed in the frequency domain which enables the use of local time stepping, multigrid acceleration, and residual smoothing to speed numerical convergence. The steady and unsteady flow equations are discretized on multiblock rectangular grids. When the flow unsteadiness is a result of unsteady blade motion, the computational grid is allowed to deform with the prescribed blade motion. A finite-volume Lax-Wendroff algorithm is used to solve the discretized flow equations. Nonreflecting far-field boundary conditions are used to allow unsteady waves to propagate out of the computational domain. In this investigation, the flow unsteadiness is the result of a prescribed blade motion. The numerical model can also determine the unsteady response of the cascade to prescribed inlet/exit distortions. This capability, however, is not being benchmarked in this report. Additional modeling assumptions and discretization techniques employed in *LNS2D* can be found in the work presented by Clark [9] and Clark and Hall [11].

4.3 Linearized Euler Model, SLiQ

The 3-D, linear unsteady Euler algorithm is referred to as *SLiQ*. The model is capable of computing the unsteady flow through an isolated blade row. The unsteadiness can be introduced by a prescribed blade motion or through the use of prescribed unsteady pressure, vortical or entropic disturbances at the inlet and/or an unsteady pressure disturbance at the exit. The ability to model blade motion is incorporated into the model through the use of a moving mesh. The steady and linearized unsteady Euler equations are descritized using a finite volume approach. The resulting system of equations are solved using a fourth order Runge-Kutta scheme. Details on this model can be found in reference [12]. The *SLiQ*code was constructed to solve for both the steady and linearized unsteady flow through an isolated blade row. However, during this study a modified version of the unsteady solver was used in which the steady flow was obtained from an *ADPAC* [13] solution of the inviscid flow through the blade row.

Chapter 5

Task 1: Compressor Cascade

The objective of Task 1 was to calibrate the *TURBO-AE* and *LNS2D* algorithms for flow conditions representative of those found in a fan or compressor. The steady and unsteady response of these components requires that the location and strength of shocks and/or the presence of separated regions be accurately predicted. To accomplish this, the linear compressor cascade configuration described in Chapter 3 was used. This section presents the results of this effort for two steady flow conditions. One with a static pressure ratio of 1.04 is characterized by supersonic inlet and exit velocities, while the other had the same supersonic inlet velocity as the first, but the static pressure ratio was raised to 1.45 which allowed the exit velocity to become subsonic. The unsteady blade surface pressure response was measured for both these steady operating points by subjecting the cascade blades to a prescribed torsional motion at a frequency of 725 Hz over a range of interblade phase angles. A summary of the steady flow operating points is given in Table 5.1. This cascade has been identified by Bölcs and Fransson [14] as the Seventh Standard Configuration.

Mass Averaged Static Pressure Ratio	Inlet Mach Number	Exit Mach Number	Exit Flow Angle (Deg)
1.04	1.315	1.25	64.8
1.45	1.315	0.99	65.6

Table 5.1: Compressor cascade test conditions

5.1 Pressure Ratio of 1.04

5.1.1 Steady Flow

Since *TURBO-AE* is a 3-D algorithm, the 2-D linear cascade geometry was modeled as if it were a stationary annular cascade with 96 blades, a hub-tip ratio of 0.98, and a tip radius of 39.5723 inches. The radius and blade number were chosen to match the linear cascade blade pitch of 2.5641 inches at mid span. The high hub-tip ratio was chosen to minimize the radial flow component. The computational domain was modeled using a conventional "H" mesh with 129 points in the axial direction, 9 points along the span, and 33 points in the tangential direction. A portion of the *TURBO-AE* mesh is shown in Figure 5.1, which depicts a constant radius mesh plane at the mid span, together with the mesh distribution on both the pressure and suction surfaces. The surface mesh had 64 mesh points along the chord of the blade and 9 points along the span. The calculations were obtained assuming inviscid flow conditions. The inlet and exit boundary conditions used are the characteristic variable approximations developed for the *TURBO*code by Janus [3] and Chen and Whitfield

The viscous, *LNS2D* analysis was performed on a multiblock "H-O-H" mesh, Figure 5.2, which consisted of an O mesh which conforms to the blade together with H mesh caps attached to the inlet and exit planes. Both H-meshes had 17 points along the axial direction with 33 points in the tangential direction. The O mesh had 185 radial and 33 circumferential lines surrounding the blade. In addition to specifying total temperature and pressure at the inlet plane and static pressure at the exit plane, steady nonreflecting far-field boundary conditions were also applied.

In addition to inviscid *TURBO-AE* and viscous *LNS2D* steady flow calculations, viscous flow predictions were also made with the *ADPAC*code. This code was used to provide another check on the steady flow predictions for the compressor cascade. The mesh used in *ADPAC*was also a multiblock H-O-H mesh that had inlet and exit H-mesh caps with 15 points in the axial direction, and 33 points in the tangential direction. The O mesh had 182 radial and 33 circumferential lines. This mesh is slightly smaller then the one used in *LNS2D*. The *ADPAC*calculations were performed using characteristic variable boundary conditions at the inlet and exit planes. These are similar to the boundary conditions used in *TURBO-AE* .

Steady blade surface pressure predictions from all three codes are compared to the measured data in Figure 5.3. The first observation made from this figure is that while all three predictions are in agreement with each other, they are in poor agreement with the measurements. This type of poor agreement with measurements has also been observed by other researchers [14] [15]. The second observation is that the inviscid *TURBO-AE* prediction is in good agreement with the viscous *LNS2D* and *ADPAC*predictions. It should be noted that all three calculations were performed using slightly different pressure ratios. This was done in an attempt to match the predicted shock locations. A typical Mach number contour plot obtained from *LNS2D* is shown in Figure 5.4. The figure clearly shows the shock structure acting on the blade.

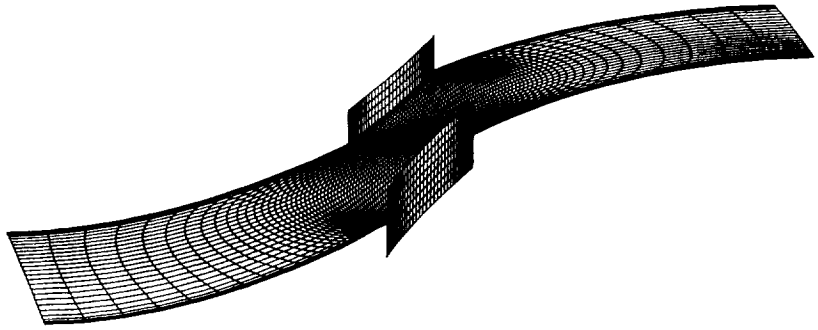

Figure 5.1: H-mesh used in *TURBO-AE* analysis of compressor cascade.

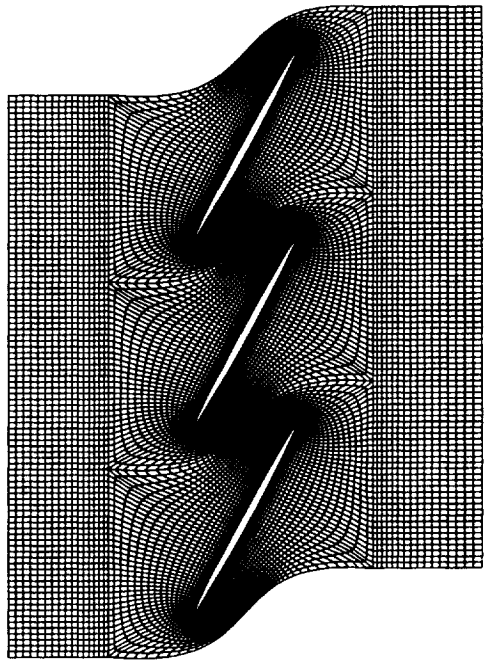

Figure 5.2: Multiblocked H-O-H mesh used in *LNS2D* analysis of compressor cascade.

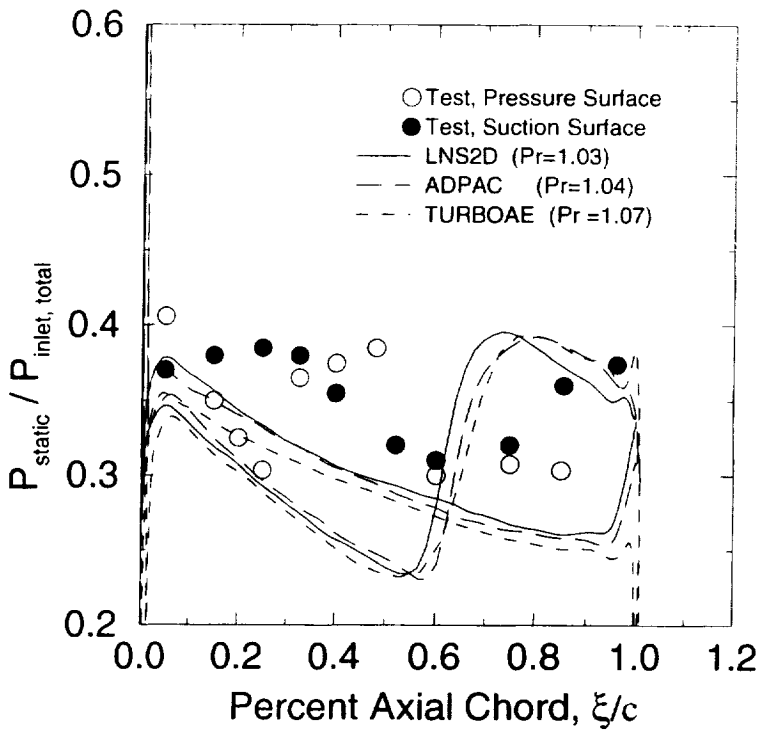

Figure 5.3: Comparison of steady blade surface pressure predictions from *TURBO-AE*, *LNS2D*, and *ADPAC*with measurements for a static pressure ratio of 1.04.

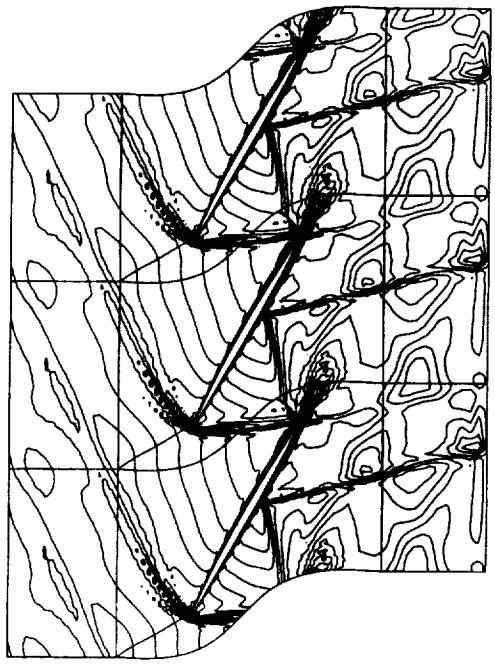

Figure 5.4: Steady Mach contours obtained from *LNS2D* for a static pressure ratio of 1.04.

5.1.2 Unsteady Flow

Despite the poor comparison of the predicted steady blade loading with measurements, the *LNS2D* program was used to predict the magnitude and phase of the unsteady blade surface pressure distribution. Attempts to obtain unsteady predictions using *TURBO-AE* were not successful for either of the steady conditions studied. The cause of this divergence was never identified. As such, unsteady results will be presented only for the linearized Navier-Stokes analysis. In addition, *ADPAC* was not used since the code is not capable of applying a boundary condition which allows the blades to vibrate.

The unsteady blade surface pressures were obtained as the result of vibrating the blades in a torsion mode at a frequency of 725Hz. Measurements were made for interblade phase angles of -30, -50, -90, 0, 80 , and 180 degrees. The comparison of the *LNS2D* predictions and measured values for these interblade phase angles are shown in Figures 5.5 through 5.10.

Comparison of the predicted blade surface unsteady pressure magnitude with the measurements for the range of interblade phase angles tested indicate that for the most part the level and trend of the measurements are well predicted by *LNS2D*. The exception to this is in the vicinity of where the bow shock reflected off of the suction surface intersects the pressure side of the blade on the opposite side of the flow passage, see Figure 5.4. The *LNS2D* calculations over-predict the magnitude of the shock for the 80 and 180 degree interblade phase angles, Figures 5.9 and 5.10. In the case of the -90 degree interblade phase angle, Figure 5.7, the magnitude is under-predicted. It should be remembered that the measurement locations for the unsteady pressure are widely spaced. As such, the discrepancy between the measurement and prediction in the vicinity of the bow shock reflection may be attributed to the large spacing between measurement transducers. Both the predictions and measurements show the location of the bow shock reflection to be at about the same position on the blade pressure surface. The exception to this occurs for the 180 degree interblade phase angle, Figure 5.10. In this case the measurements do not indicate the presence of a reflected shock on the pressure surface, while the predictions show one at about the 60% chord location. The measurements indicate that the shock reflection occurs on the suction side of the blade. A condition which is not physically possible. The reason for this discrepancy in the data reported in reference [2] is not known.

The predicted and measured phase angle distribution on the suction surface for the most part are in good agreement with each other. Exception to this observation is most pronounced for the 80 degree interblade phase angle case where the predicted phase distribution does not match the measurements over the whole length of the blade. In the case of the -90 and 180 degree interblade phase angles, the predictions differ from the measurements over the aft 30% of the surface.

The comparison of the predicted and measured phase distribution on the pressure side of the blade shows more of a difference in level and trend than was observed on the suction surface. This is probably related to the location of the shock reflection.

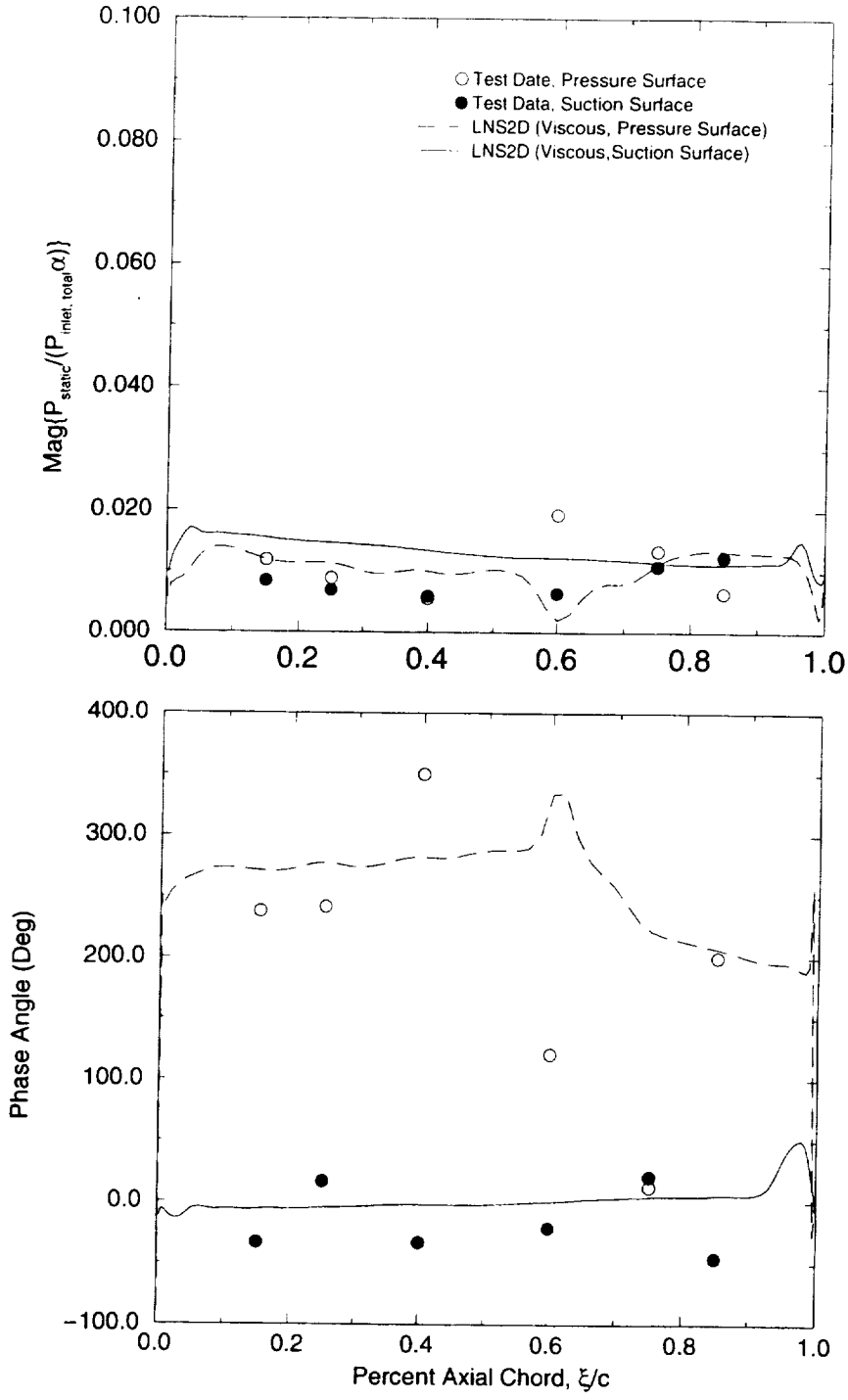

Figure 5.5: Comparison of unsteady blade surface pressure magnitude and phase predictions from, *LNS2D*, with measurements for a static pressure ratio of 1.04, a torsion mode oscillation at 725 Hz and an interblade phase angle of -30 degrees.

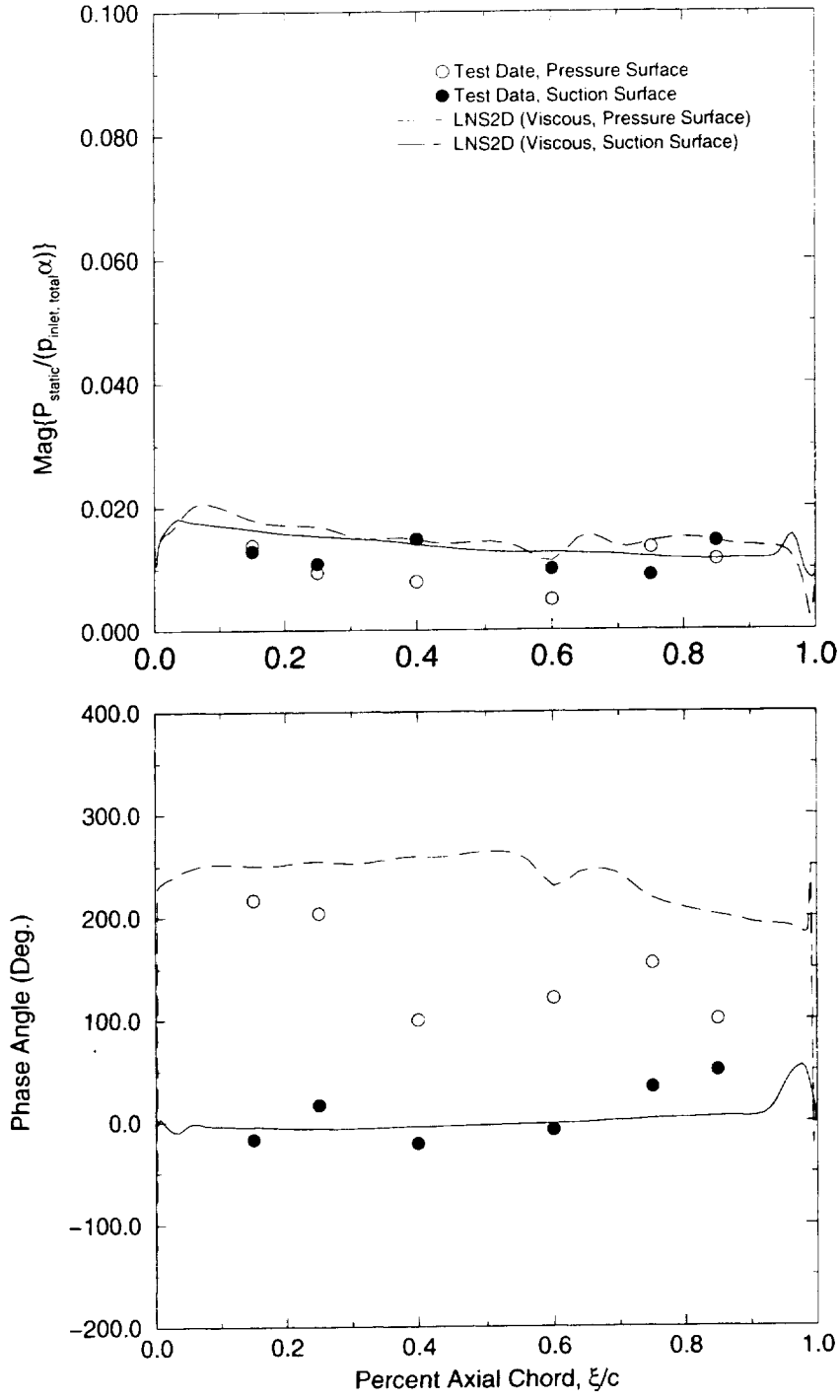

Figure 5.6: Comparison of unsteady blade surface pressure magnitude and phase predictions from, *LNS2D*, with measurements for a static pressure ratio of 1.04, a torsion mode oscillation at 725 Hz and an interblade phase angle of -50 degrees.

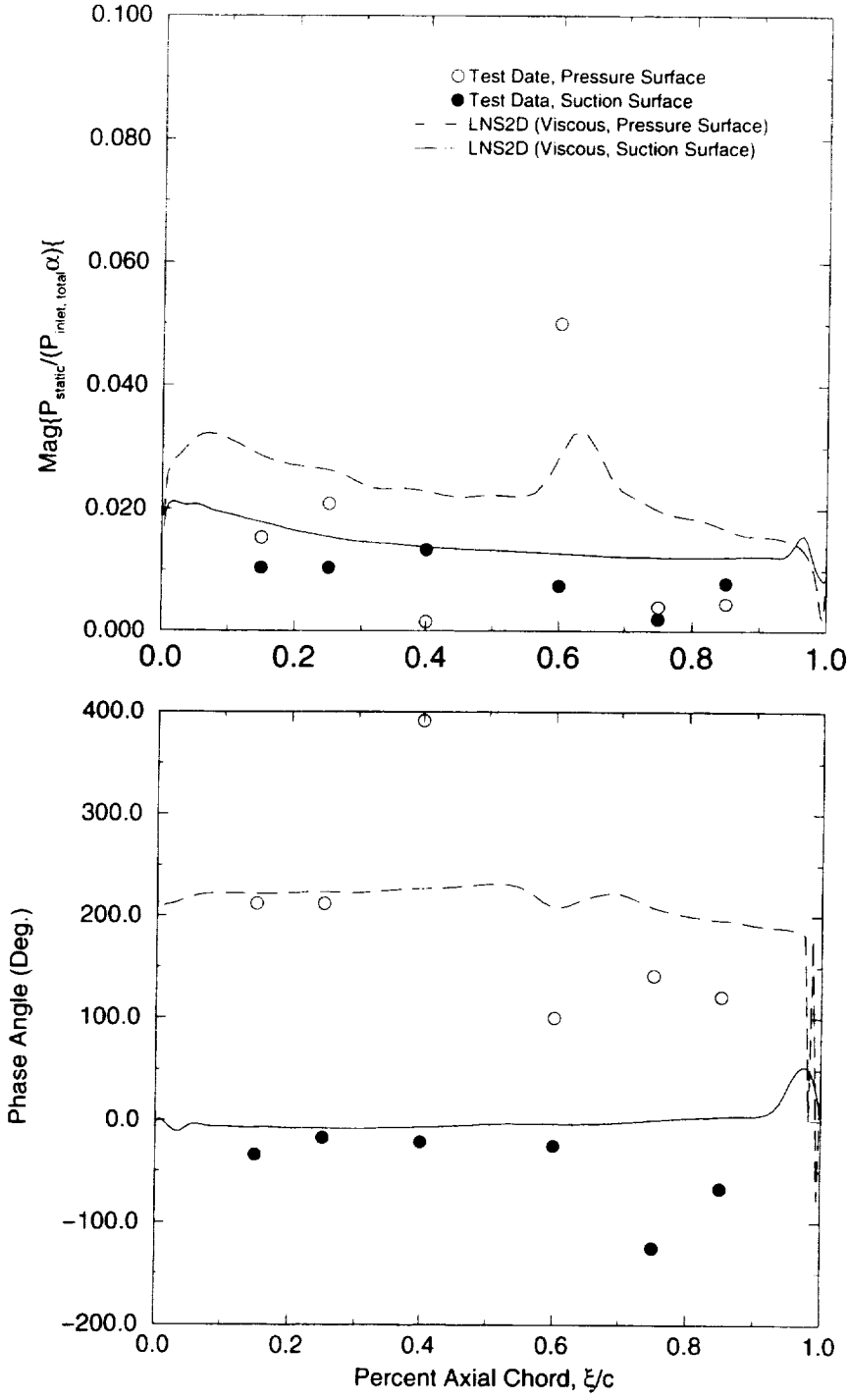

Figure 5.7: Comparison of unsteady blade surface pressure magnitude and phase predictions from, *LNS2D*, with measurements for a static pressure ratio of 1.04, a torsion mode oscillation at 725 Hz and an interblade phase angle of -90 degrees.

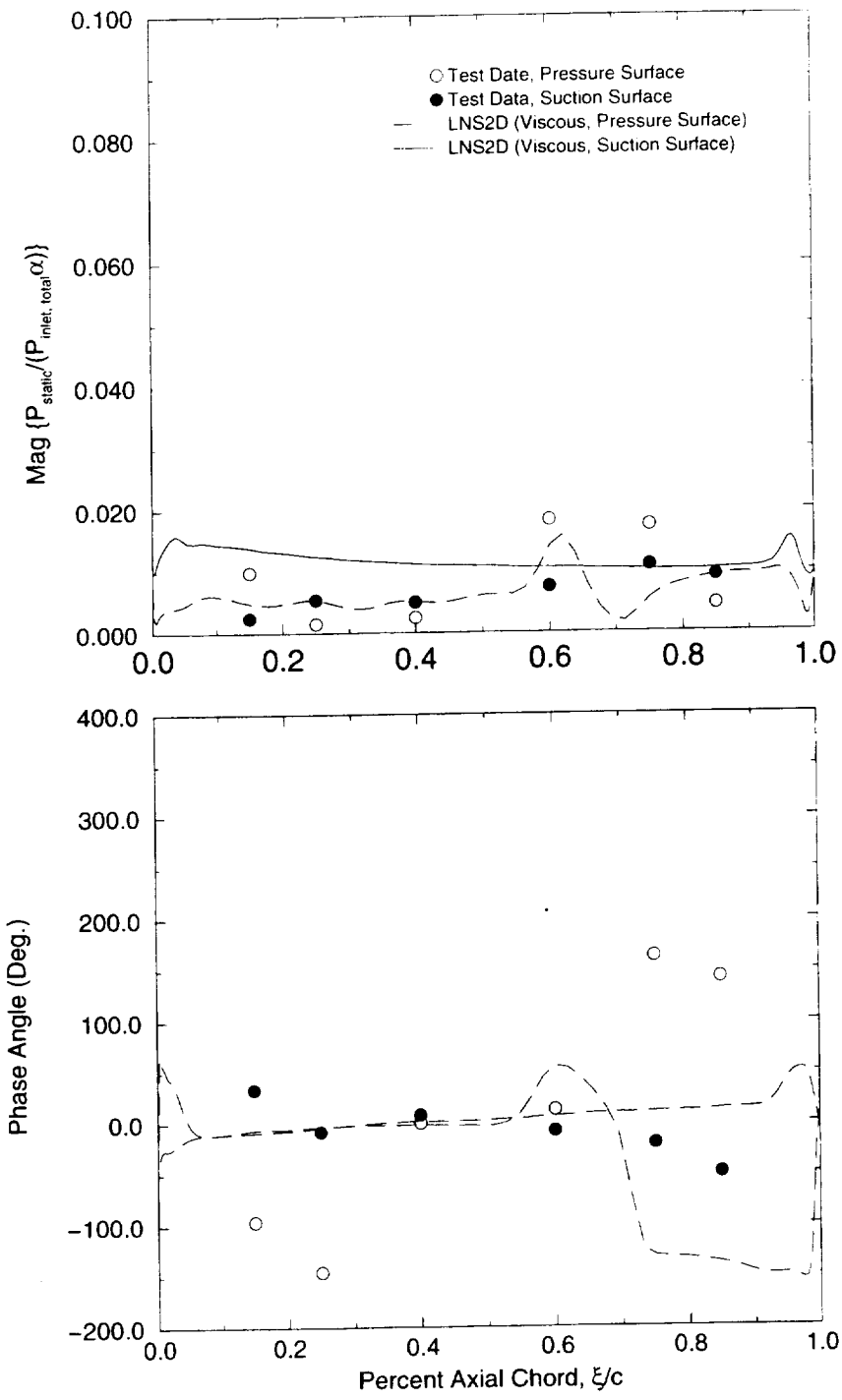

Figure 5.8: Comparison of unsteady blade surface pressure magnitude and phase predictions from, *LNS2D*, with measurements for a static pressure ratio of 1.04, a torsion mode oscillation at 725 Hz and an interblade phase angle of 0 degrees.

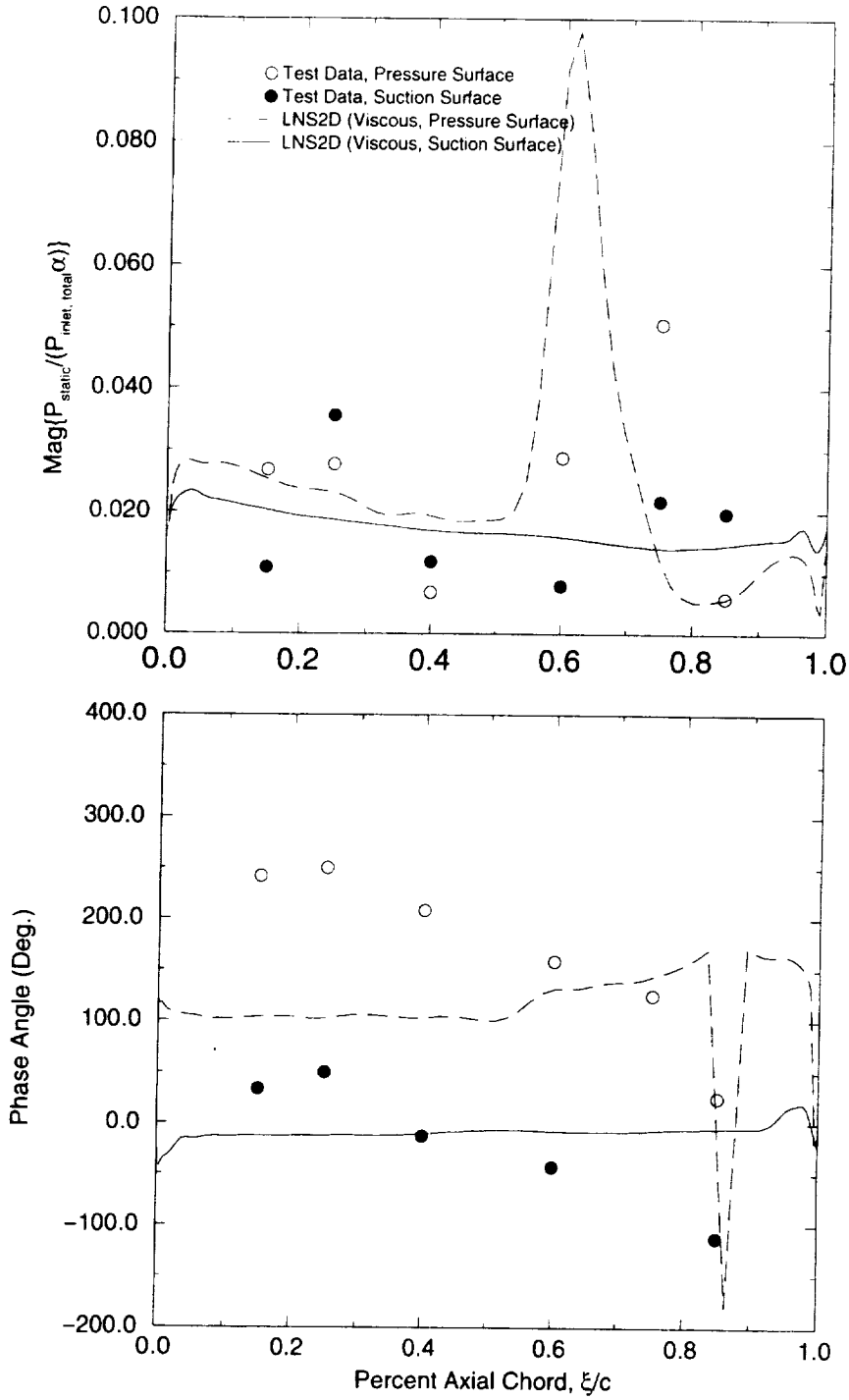

Figure 5.9: Comparison of unsteady blade surface pressure magnitude and phase predictions from, *LNS2D*, with measurements for a static pressure ratio of 1.04, a torsion mode oscillation at 725 Hz and an interblade phase angle of 80 degrees.

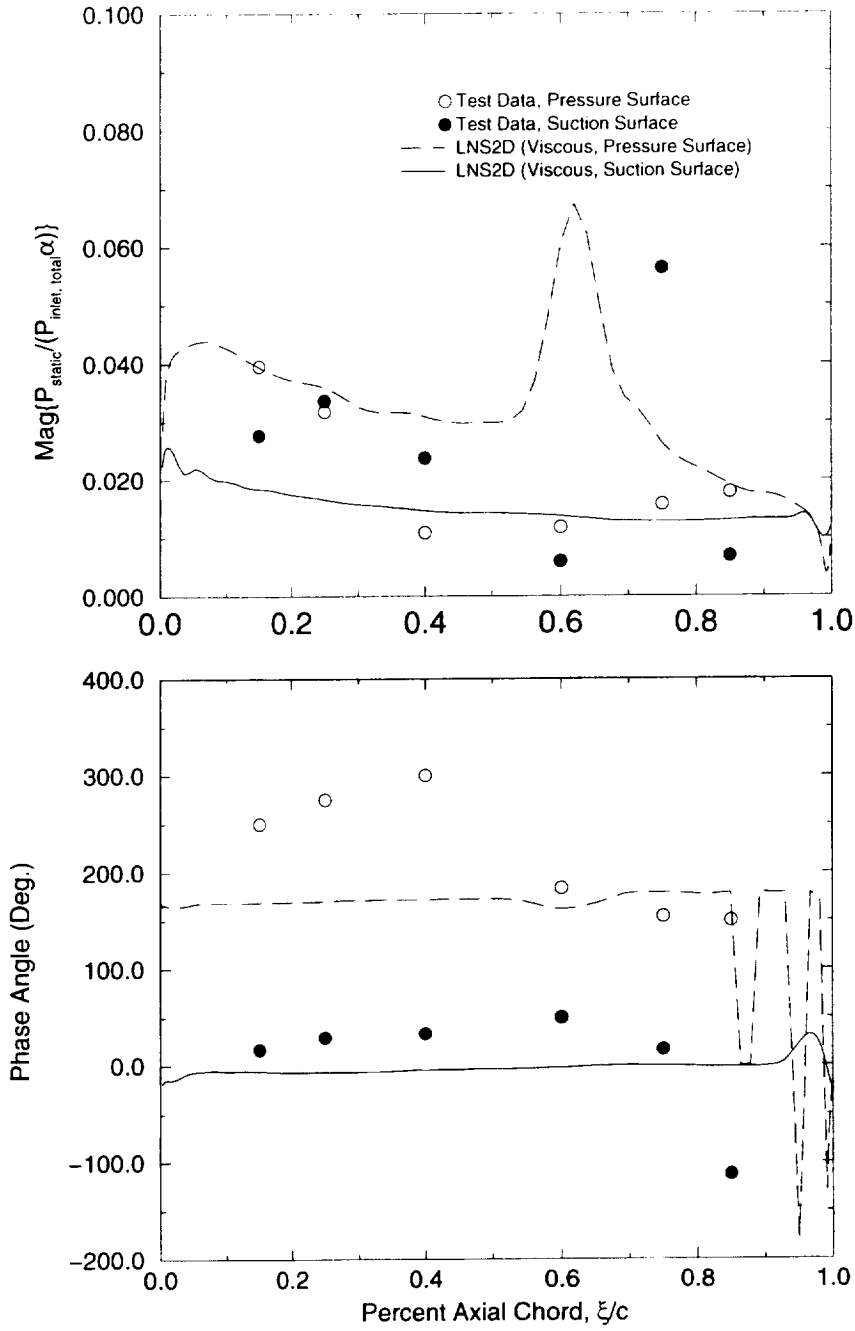

Figure 5.10: Comparison of unsteady blade surface pressure magnitude and phase predictions from, *LNS2D*, with measurements for a static pressure ratio of 1.04, a torsion mode oscillation at 725 Hz and an interblade phase angle of 180 degrees.

5.2 Pressure Ratio of 1.45

5.2.1 Steady Flow

The back pressure of the computational model was raised in an attempt to match steady and unsteady measurements for a cascade flow condition in which the inlet flow was supersonic and the exit flow subsonic relative to the blade. Steady blade surface predictions obtained from *TURBO-AE* , *LNS2D*, and *ADPAC*were compared to measurements as shown in Figure 5.11. Also shown in this figure are the static pressure ratios obtained from each of the algorithms. The Mach number contours predicted by *LNS2D* are shown in Figure 5.12 and indicate that for this back pressure there is a normal shock in the blade passage which intersects the suction surface at about the 70% chord position. The predictions from *LNS2D* and *ADPAC*are in good agreement with each other and with the measurements on the suction surface except in the vicinity of the shock. Both codes predict the shock to be farther upstream than what is indicated by the measurements. The *TURBO-AE* predictions on the suction surface indicate that the bow shock intersects the suction surface in the vicinity of the trailing edge and then reflects back onto the pressure surface of the adjacent blade. Attempts to adjust the exit pressure in *TURBO-AE* to match the other suction surface predictions were not successful.

The calculated pressure surface steady pressure distribution does not agree with the measurements over the last 60% of the blade. This discrepancy is probably the result of not applying any streamtube contraction to the steady flow model. The *LNS2D* algorithm is only a 2-D model and as such cannot handle any change in streamtube height. At the time of the writing of this report, the code was being extended to include quasi-3-D effects. A full 3-D *ADPAC*model of the compressor cascade was not run.

5.2.2 Unsteady Flow

The steady flow condition presented in section 5.2.1 were used to make unsteady predictions using the *LNS2D* algorithm. Attempts to make unsteady predictions using *TURBO-AE* were not successful. The solution would begin to diverge about half way through one oscillation cycle. This was the same behavior observed for the lower pressure ratio case. Unsteady predictions were made for the same interblade phase angles at which measurements were made, -170, -65, 0, 60, and 85 degrees. Comparison of the predicted and measured unsteady blade surface pressure distribution for the range of interblade phase angles tested is shown in Figures 5.13 through 5.17. These figures present the unsteady blade surface pressure magnitude and phase as a function of the blade axial chord. The predicted and measured unsteady pressure magnitude are small and in good agreement with each other over most of the blade surface. The exception being in the vicinity of the blade leading edge and the shock intersection on the pressure surface. The predictions over-predict the level of the shock load. As was noted in section 5.1.2, some of the discrepancy between prediction and measurement is probably due to the coarse distribution of the unsteady pressure transducers on the blade surface.

Comparison of the predicted phase angle distribution on the blade surface with those obtained from the measurements indicates that there is generally poor agreement

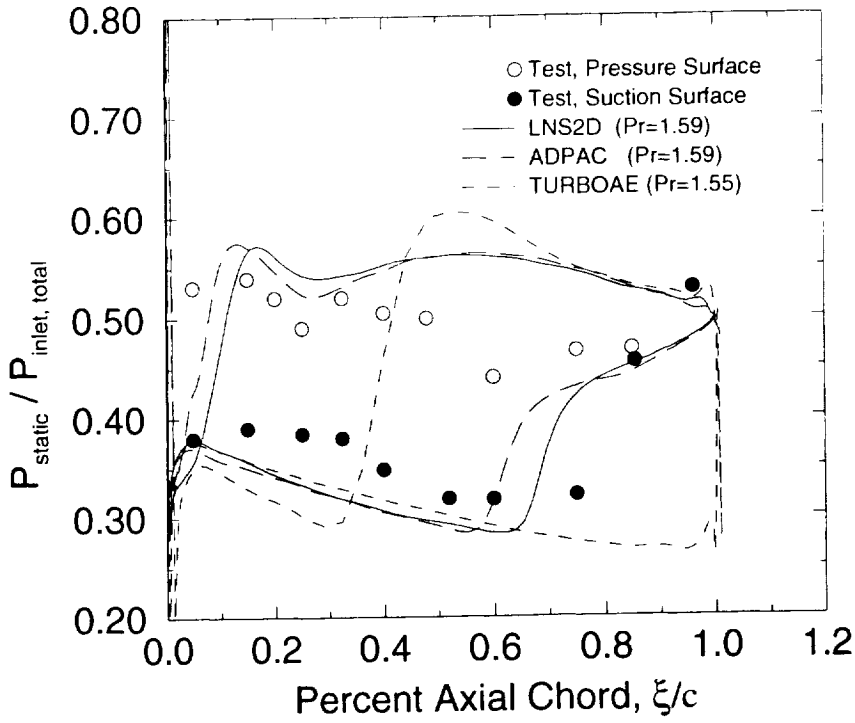

Figure 5.11: Comparison of steady blade surface pressure predictions with measurements for the 1.45 pressure ratio compressor cascade.

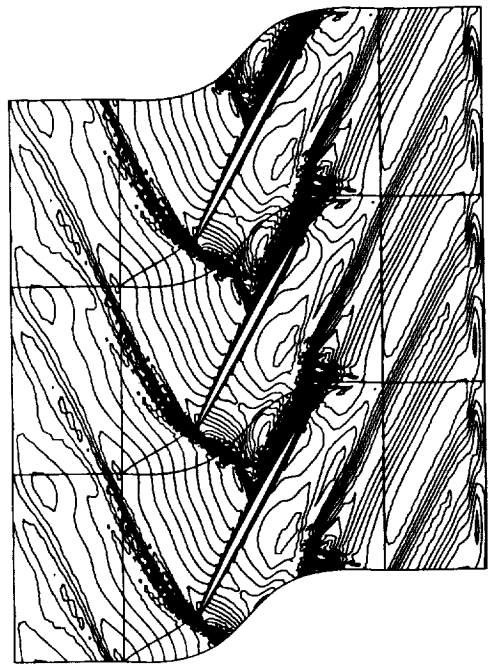

Figure 5.12: *LNS2D* predicted Mach number contours for the 1.45 pressure ratio compressor cascade.

between them. The is particularly true for the -170, -65 and 0 interblade phase angles. The positive interblade phase angles, 60 and 85 degrees, show better agreement for locations from the leading edge to the shock. Downstream of the shock, the differences are again quite large.

5.3 Unsteady Aerodynamic Work

The unsteady work-per-cycle for the compressor cascade executing a torsional vibration is plotted as a function of the interblade phase angle for the 1.04, 1.59, and 1.65 pressure ratios used in the predictions, Figure 5.18. Also shown is the unsteady work calculations based on the unsteady pressures measured in the linear cascade for the 1.45 pressure ratio case. The levels of the work-per-cycle obtained from the measured unsteady pressures are much lower than those obtained from the predicted results. The reason for this difference can be seen by referring to the comparison of the measured and predicted unsteady blade surface pressures shown in Figure 5.17. The work-per-cycle calculation based on the measured data was accomplished by assuming that the data points between the first and last transducer on a given surface are connected with a straight line. Extrapolation is used to construct the unsteady pressure upstream and downstream of the first and last transducers on a surface. This procedure completely misses the shock impulses on the pressure and suction surface. Because of this, similar calculations were not carried out using data obtained from the 1.04 pressure ratio case.

The rotating rig upon which the cascade geometry was constructed, see reference [2], experienced flutter for a pressure ratio corresponding to the 1.45 value used in testing. Flutter occurred for a range of interblade phase angles from -60 to -120 degrees. However, the rig did not experience any flutter for a condition corresponding to the 1.04 pressure ratio. Unsteady work predictions based on the calculated unsteady blade surface pressure for pressure ratios of 1.04 and 1.65 show that the cascade becomes unstable for both of these conditions. Also shown is the effect on unsteady work-per-cycle of lowering the back pressure from 1.65 to 1.59. In this case, the normal shock shown in Figure 5.12 moves slightly downstream. This small rearward movement results in a cascade that is stable over the complete interblade phase angle range. This small change in shock position demonstrates the sensitivity of cascade stability to shock position.

5.4 Conclusions

This chapter presented the results for work performed under Task 1 of the contract. The objective was to calibrate the *TURBO-AE* and *LNS2D* algorithms against measured data. The measurements selected for the calibration were obtained from a linear cascade which modeled the tip section of a high speed fan. Steady loading on the blade surface was predicted using three algorithms, *TURBO-AE* , *LNS2D*, and *ADPAC*. All three codes predicted similar steady pressure distributions on the blade surface for the case in which both the inlet and exit velocities were supersonic. However the predictions did not match the measured steady pressure distribution for this case. The reason for this discrepancy could not be determined, however other researchers have also reported difficulty in matching the measured data for this steady flow condition. In the case of the subsonic

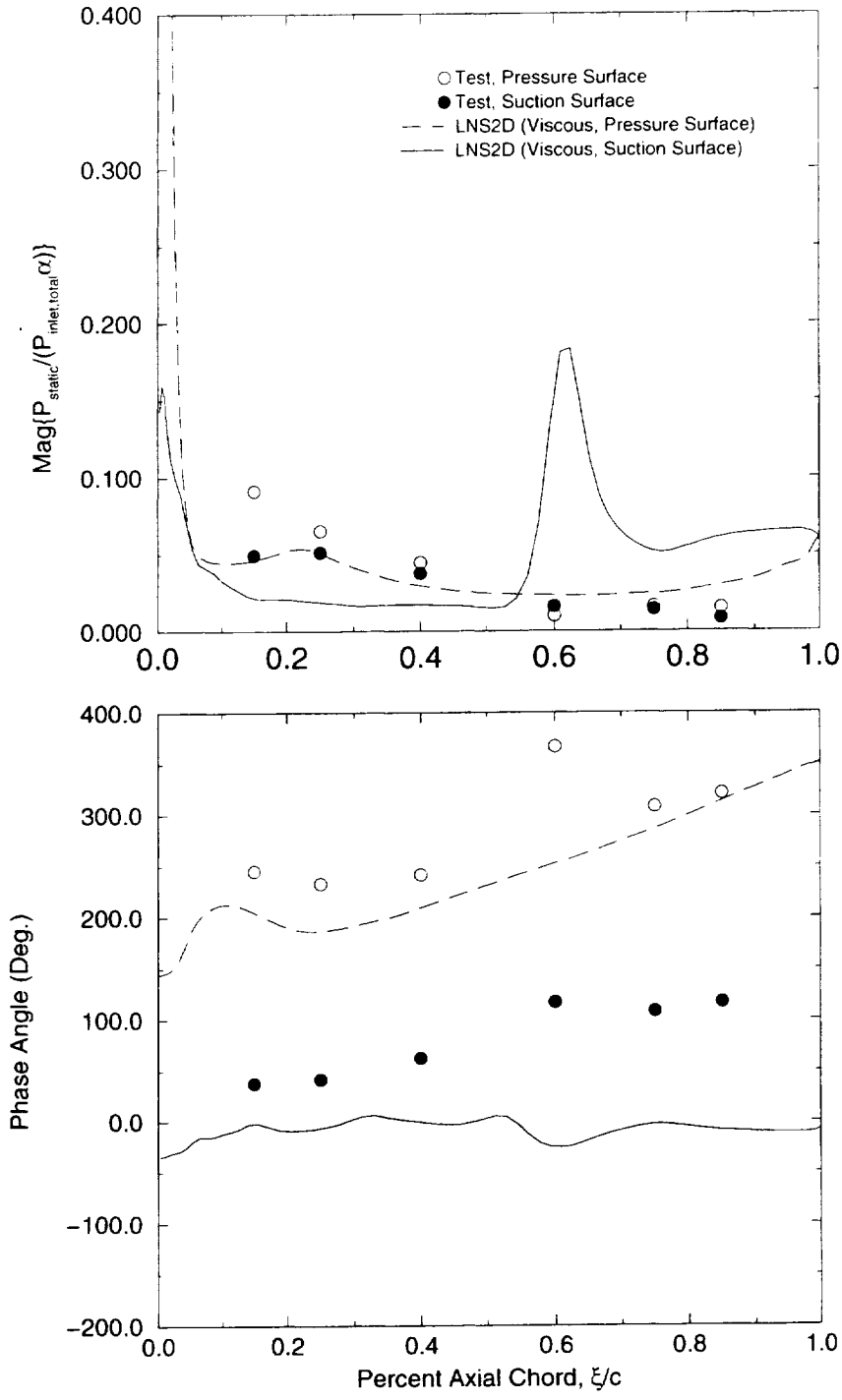

Figure 5.13: Blade surface unsteady pressure distribution, magnitude (*top*), and phase (*bottom*) compared to measurements for the 1.45 pressure ratio compressor cascade vibrating in a torsion mode at 725Hz and an interblade phase angle of -170 degrees. The predictions were made using *LNS2D*.

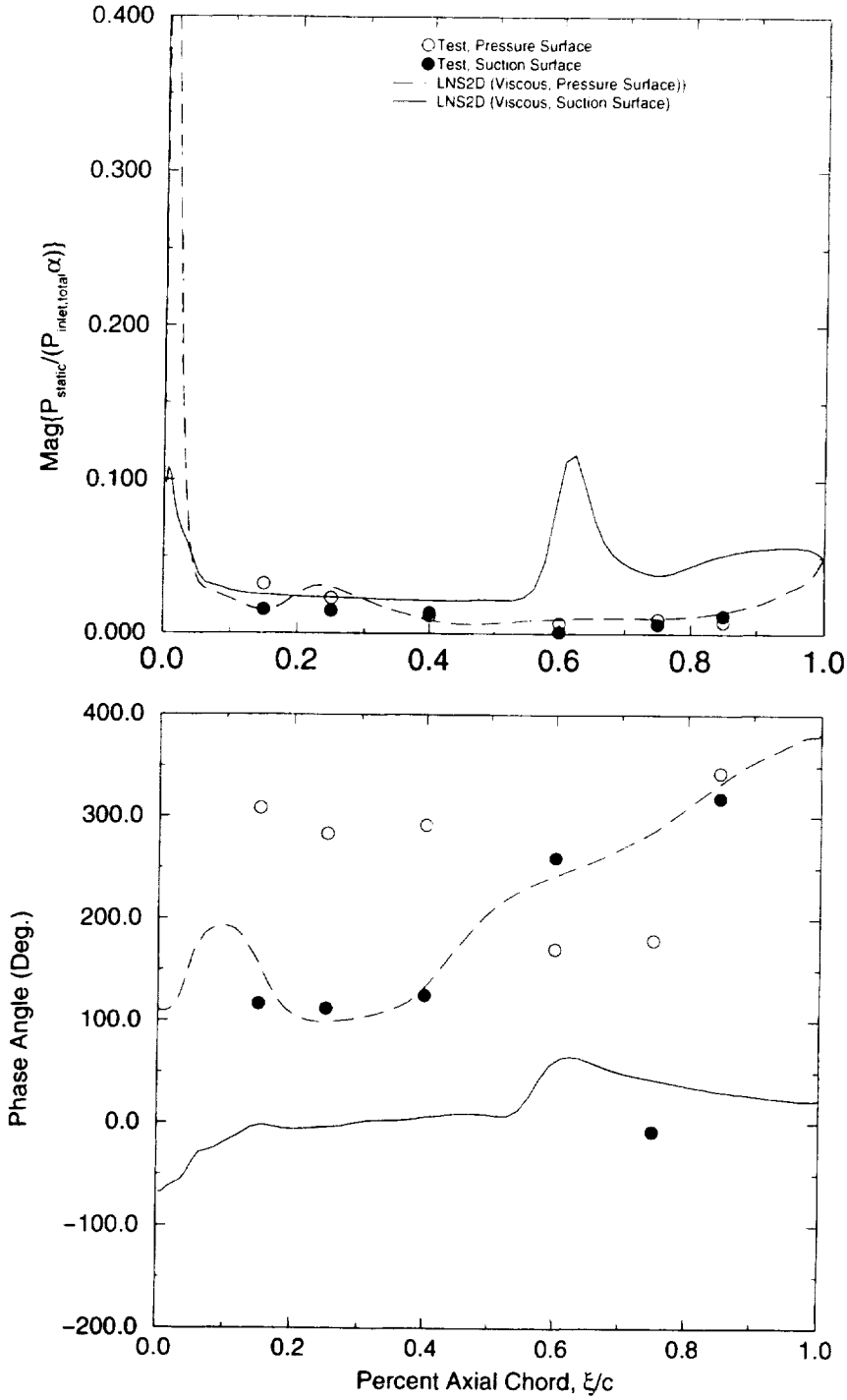

Figure 5.14: Blade surface unsteady pressure distribution, magnitude (*top*), and phase (*bottom*) compared to measurements for the 1.45 pressure ratio compressor cascade vibrating in a torsion mode at 725Hz and an interblade phase angle of -65 degrees. The predictions were made using *LNS2D*.

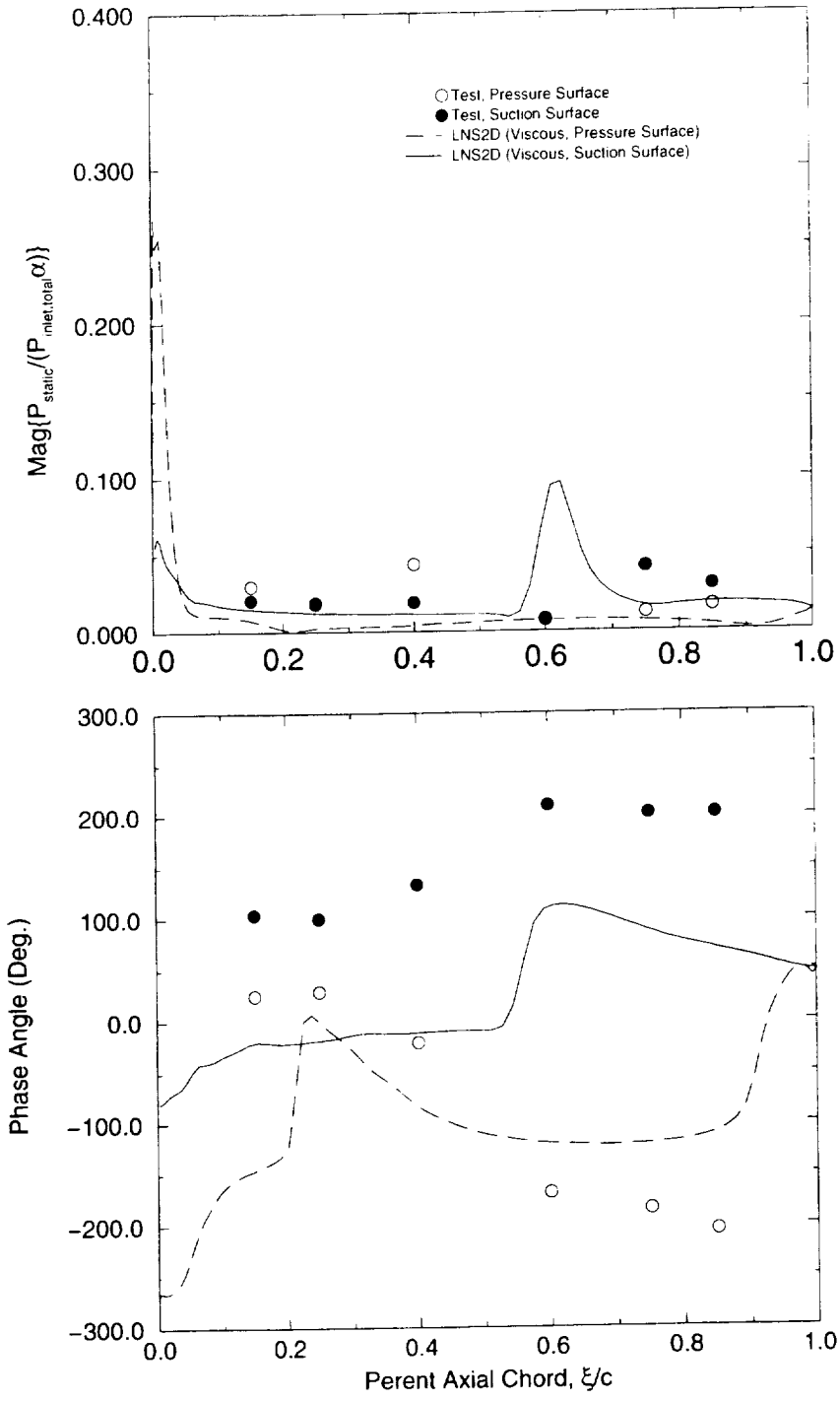

Figure 5.15: Blade surface unsteady pressure distribution, magnitude (*top*), and phase (*bottom*) compared to measurements for the 1.45 pressure ratio compressor cascade vibrating in a torsion mode at 725Hz and an interblade phase angle of 0 degrees. The predictions were made using *LNS2D*.

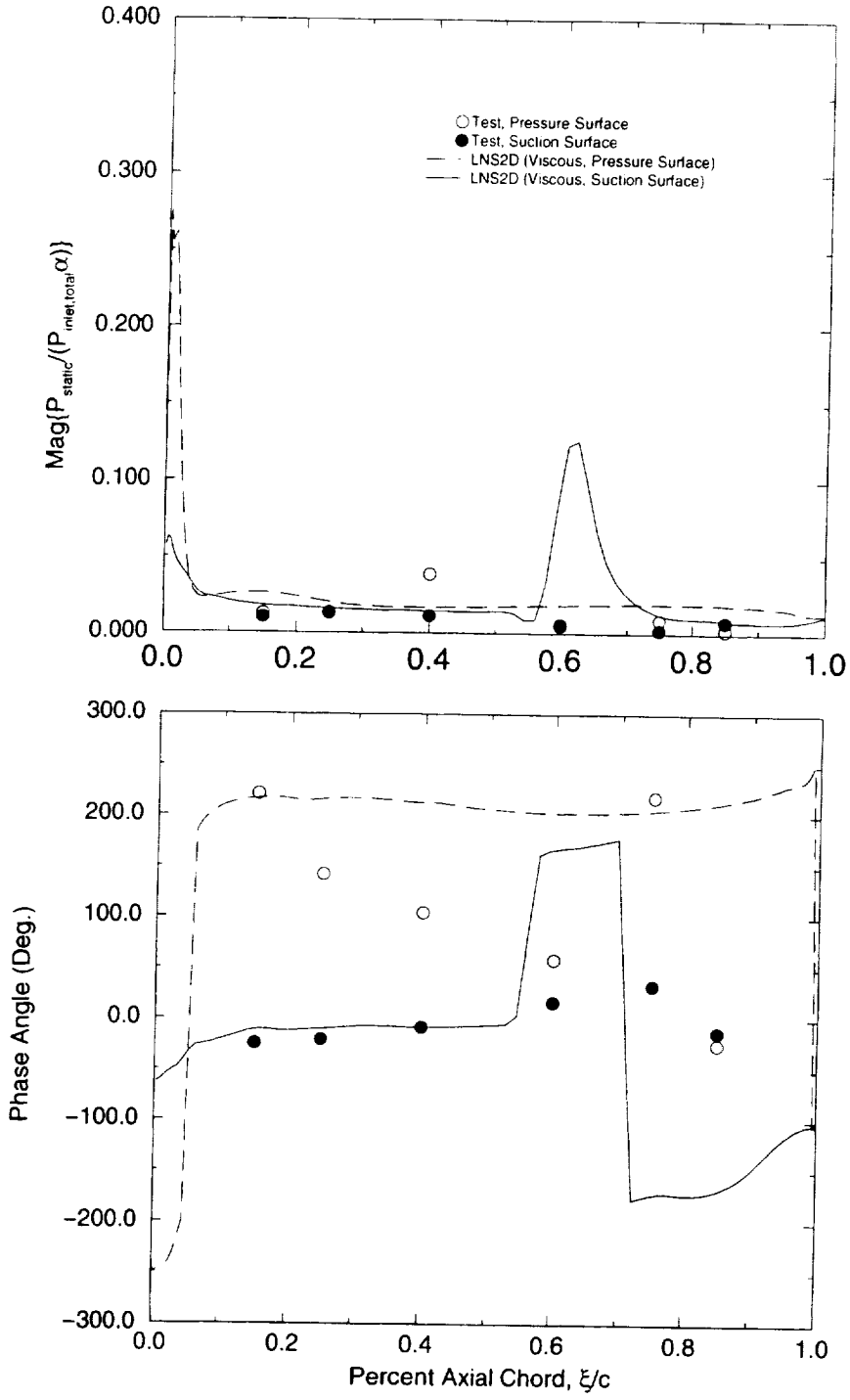

Figure 5.16: Blade surface unsteady pressure distribution, magnitude (*top*), and phase (*bottom*) compared to measurements for the 1.45 pressure ratio compressor cascade vibrating in a torsion mode at 725Hz and an interblade phase angle of 60 degrees. The predictions were made using *LNS2D*.

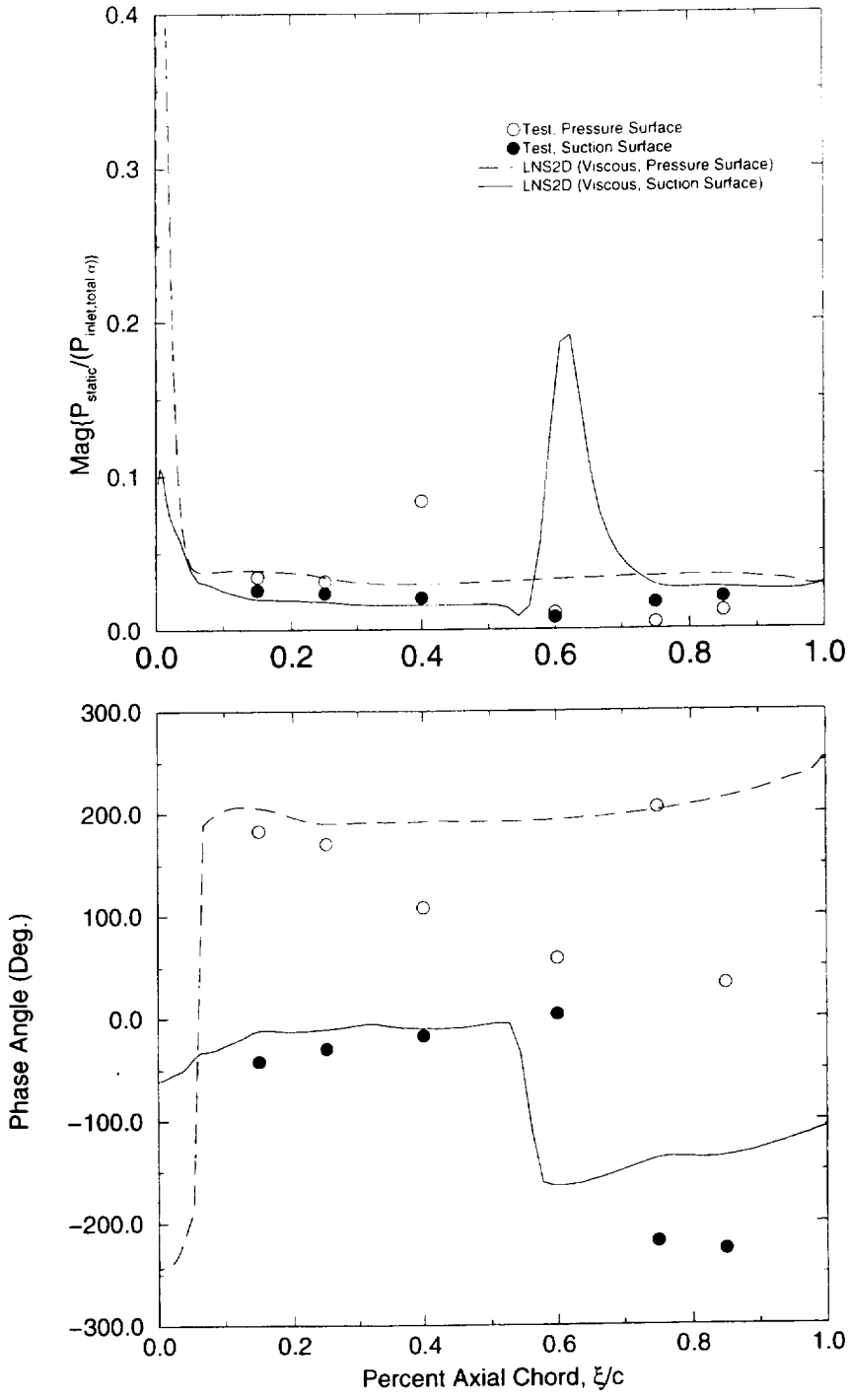

Figure 5.17: Blade surface unsteady pressure distribution, magnitude (*top*), and phase (*bottom*) compared to measurements for the 1.45 pressure ratio compressor cascade vibrating in a torsion mode at 725Hz and an interblade phase angle of 85 degrees. The predictions were made using *LNS2D*.

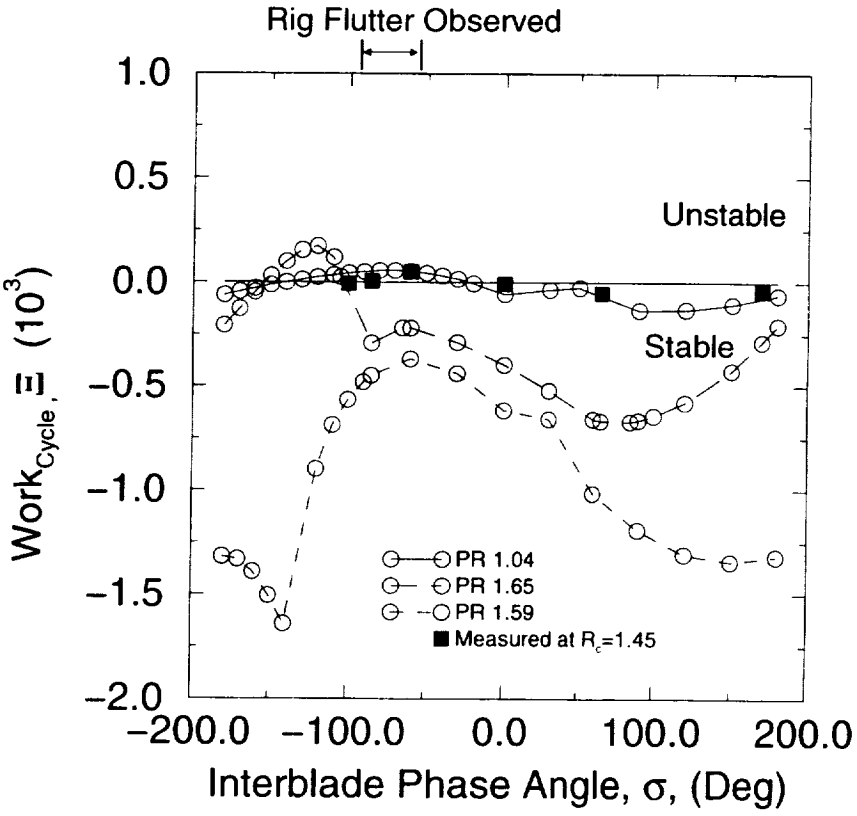

Figure 5.18: Predicted unsteady aerodynamic work per cycle for the compressor cascade.

exit flow, the *LNS2D* and *ADPAC* predictions were closer to the measured steady pressures than the *TURBO-AE* predictions. It was felt that the discrepancy between the *LNS2D* and *ADPAC* predictions was probably the result of not applying a stream tube height correction to the 2-D calculations. The difference between the *TURBO-AE* predictions and measurements was related to the problem of specifying a unique incidence condition at the inlet plane of the calculation. The fact that the *TURBO-AE* was not able to handle the unique incidence requirement was not considered a drawback since the code would rarely be used to model a 2-D stator cascade in which the inlet flow is supersonic. The ability of *TURBO-AE* to model rotor flow in which the tip sections are operating supersonically was investigated as part of Task 3.

Attempts to make unsteady calculations using *TURBO-AE* were not successful. Therefore, only the *LNS2D* code was used to predict the unsteady blade surface pressure response. The predicted magnitude of the unsteady response, for the steady flow with supersonic inlet and exit velocities, matched the measurements over most of the blade surface. However, the shock impulse on the suction surface was not very well predicted. The difference between the measured and predicted surface unsteady pressure in the shock region could be the result of having only a few transducers in the shock region. The phase predictions for this case were respectable on the pressure surface but poor on the suction surface. This trend was observed for all interblade phase angles investigated. Similar trends were also observed for the steady flow condition with subsonic exit flow. The cause of poor phase prediction is not known and should be investigated in the future. Despite the poor phase prediction on the suction surface, the unsteady work predictions indicate a range of unstable operation which is similar to that observed during rig testing of the fan blade from which the cascade blade was modeled.

Chapter 6

Task 2: Turbine Cascade

The objective of Task 2 was to investigate the ability of the *TURBO-AE* and *LNS2D* codes to predict the unsteady aerodynamic response of a high turning turbine cascade. The linear cascade facility used to obtain the experimental data has been described previously in Chapter 3. The first part of this chapter describes the steady and unsteady predictions for a cascade expansion ratio of 1.531. This condition corresponds to a case in which the steady flow through the cascade is completely subsonic. This flow provided a relatively simple condition with which to begin the calibration process. Next, a discussion of a 2.713 expansion ratio flow condition is given. In this case the cascade inlet velocity is subsonic, while the exit velocity is supersonic. A summary of the test conditions covered in this chapter is given in Table 6.1. The chapter concludes with a description of the unsteady work-per-cycle obtained from a prescribed torsional motion at the two expansion ratios.

6.1 Expansion Ratio of 1.531

6.1.1 Steady Flow

Since *TURBO-AE* is capable of modeling a full 3-D geometry, the 2-D linear cascade was modeled as if it were a high hub-tip ratio annular cascade. The cascade was modeled as a

Ideal Inlet Total to exit Static Expansion ratio	Mass Averaged Expansion Ratio	Inlet Mach Number	Inlet Static Pressure (psia)	Cascade Incidence Angle (deg)	Mass Averaged Exit Mach Number
1.5:1	1.53	0.5	12.74	-6.6	0.78
2.8:1	2.71	0.52	12.30	-6.6	1.25

Table 6.1: Turbine cascade test conditions.

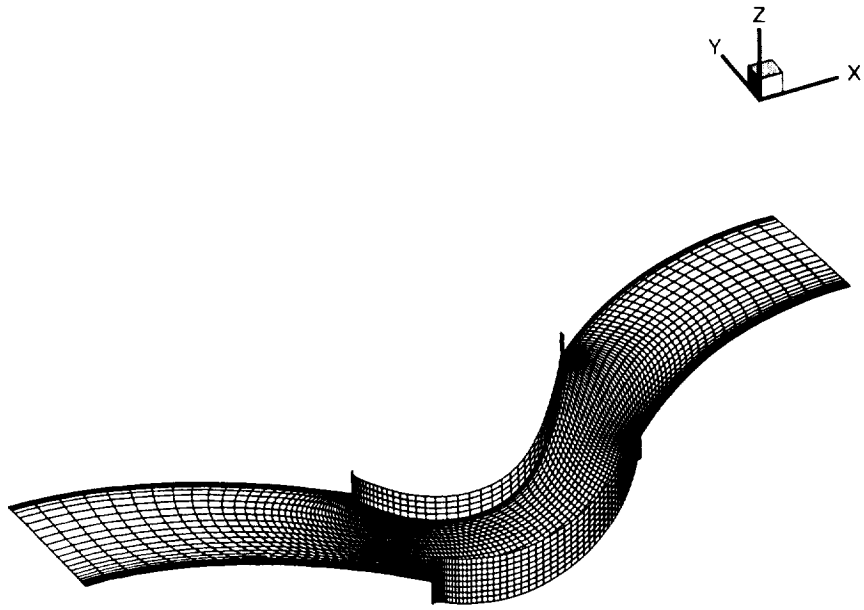

Figure 6.1: Typical single block, H mesh used in *TURBO-AE* analysis of high turning turbine cascade analysis (*single, constant radius plane shown for clarity*).

stationary annular cascade with 96 blades, a 0.98 hub-tip-ratio, and a tip radius of 21.4625 inches. These parameters were selected to match the solidity of the test cascade at mid chord. A constant radius section of the computational mesh used in the *TURBO-AE* analysis of the turbine cascade is shown in Figure 6.1. The mesh had 129 points in the axial direction, 9 constant radius planes in the radial direction, and 33 points in the tangential direction. The inlet and exit planes were located about one axial chord length upstream and downstream of the cascade leading and trailing edges respectively.

A typical computational mesh used by *LNS2D* is shown in Figure 6.2. The multiblock mesh shown is constructed by placing H grid caps on the inlet and exit boundaries of an O grid which conforms to the turbine blade section being modeled. The dimensions for the upstream H grid, the airfoil O grid, and the downstream H grid are 17×33, 165×33, and 21×21, respectively. A mesh sensitivity study was performed to determine the required grid resolution necessary to achieve the grid independent solutions reported herein. Also, it should be noted that through the application of periodic boundary conditions, both the steady and unsteady numerical simulations are performed on a single computational blade passage regardless of interblade phase angle being considered.

The *TURBO-AE* code has two types of far-field boundary conditions that can be

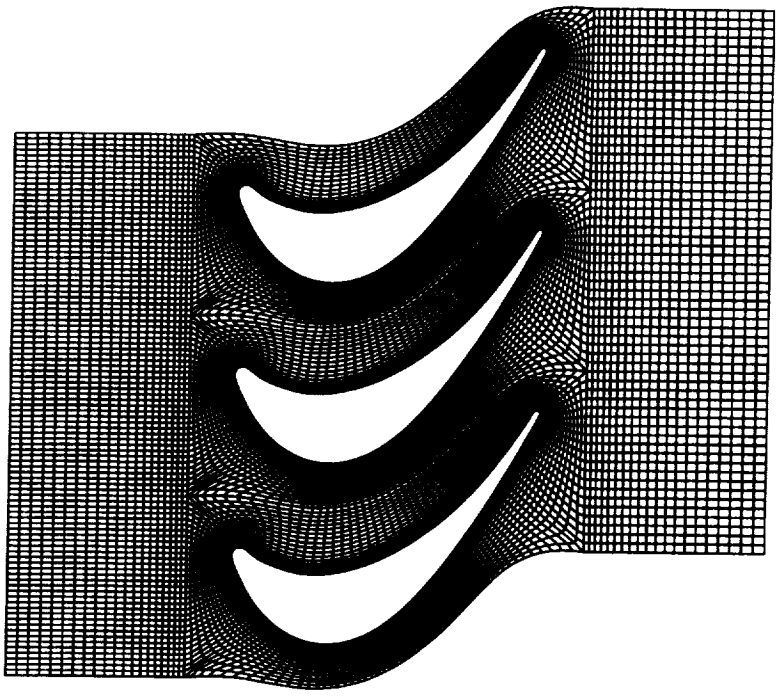

Figure 6.2: Typical multiblocked, H-O-H mesh used in *LNS2D* analysis of high turning turbine cascade analysis (*multiple passages shown for clarity*).

imposed: the original boundary conditions which are considered reflecting with respect to an unsteady disturbance, and a new boundary condition which is nonreflecting. In the case of the steady flow calculation being considered, the application of either boundary condition should yield the same result. To check this assumption both boundary conditions were exercised on the the same grid. The resulting predictions are shown in Figure 6.3 which gives the steady blade surface pressure as a function of the projected axial chord. The normalized pressure shown in Figure 6.3 is the predicted blade surface static pressure divided by the inlet free stream total pressure. The predictions are also in good agreement with the measured data except in a region near the leading edge of the suction surface. Evidence obtained during the experimental program indicates that due to the negative incidence angle the flow was separated in this region, see reference [1]. A plot of the convergence history of the solution for both sets of boundary conditions is shown in Figure 6.4. The upper curve shows the history of the mass flow ratio and the lower curve the torque developed on the suction surface of the blade. The mass flow rate converged to a value of unity after about 2800 iterations, while the torque converged in about 2500 iterations.

The viscous *LNS2D* predictions for the 1.531 expansion ratio are compared to those obtained from *TURBO-AE* in Figure 6.5. Both calculations were performed using nonreflecting far-field boundary conditions. Again, good agreement between the two predictions was obtained over most of the blade with the exception of the separated region on the suction surface near the leading edge. In this region the viscous *LNS2D* prediction is closer to the measured data.

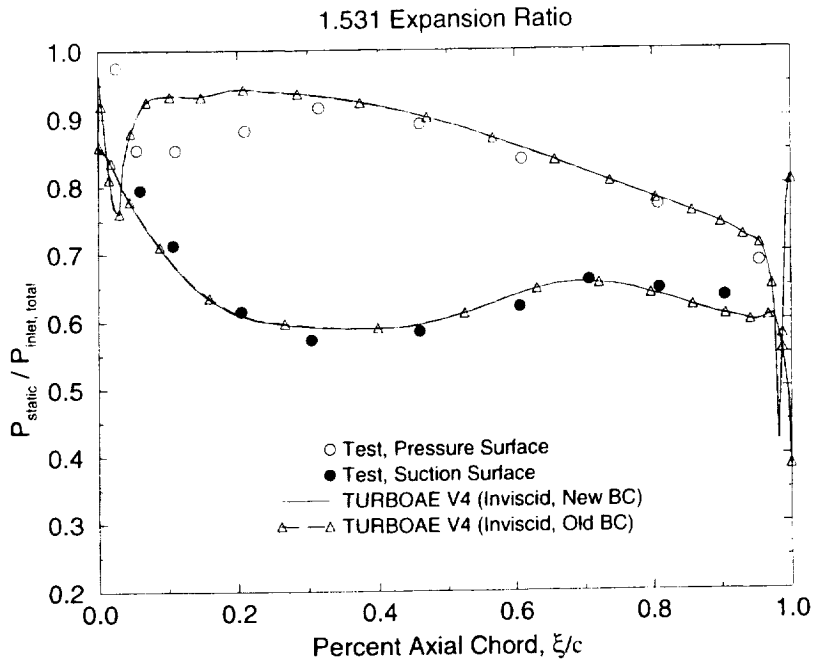

Figure 6.3: Steady blade loading predicted by *TURBO-AE* using both the old (reflecting) and new nonreflecting far-field boundary conditions.

An attempt was made to use *TURBO-AE* to make a viscous calculation of the steady flow. The 129x9x33 mesh used to generate the inviscid results reported on above, was regenerated with a tighter clustering of points near the blade surface. When a calculation was attempted using the nonreflecting far-field boundary conditions, the solution diverged. However if the older, reflecting, far-field conditions were used, the solution converged after 3000 iterations. The converged viscous predictions are compared to the inviscid results obtained from the nonreflecting far-field conditions in Figure 6.6. The comparison shows that the inviscid predictions are in better agreement with the measurements than are the viscous predictions. Since the unsteady calculation is probably better performed using the nonreflecting far-field conditions, the inviscid steady flow will be used in the unsteady calculations.

6.1.2 Unsteady Flow

The inviscid steady flow discussed in section 6.1.1 was used in the unsteady calculations reported on in this section. The unsteady response was the result of a rigid body torsional oscillation at a frequency of 340 Hz and a prescribed interblade phase angle. The unsteady *TURBO-AE* calculations were made using phased lagged unsteady boundary conditions along the periodic boundaries of the grid. As such, only one extended blade passage needed to be considered. nonreflecting far-field boundary conditions were prescribed at the inlet and exit planes. The *LNS2D* calculations were also performed on a mesh that covered only one blade passage. Since in this case the unsteady flow is modeled

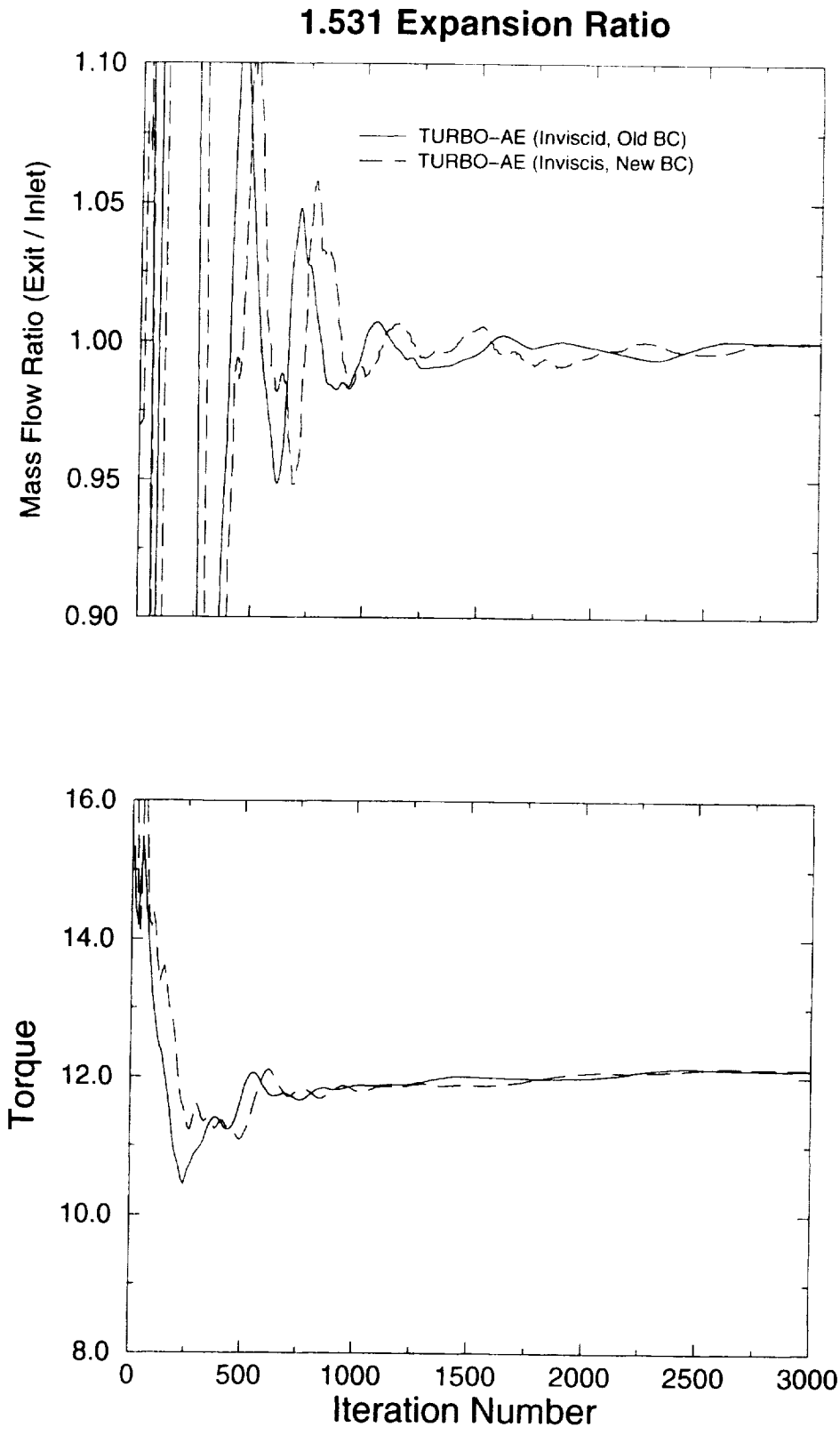

Figure 6.4: Convergence history of the *TURBO-AE* predictions for the 1.531 expansion ratio.

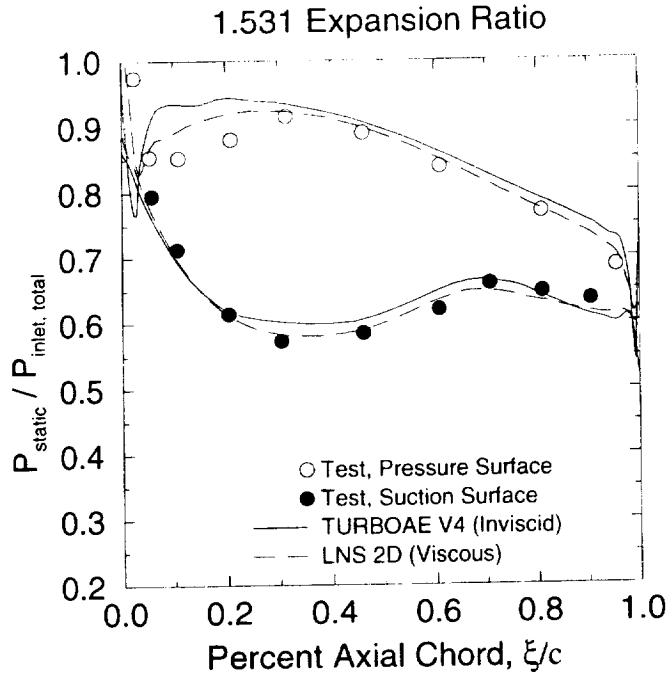

Figure 6.5: Comparison of steady blade loading predicted by *TURBO-AE* and *LNS2D* with measurements for the 1.531 expansion ratio flow.

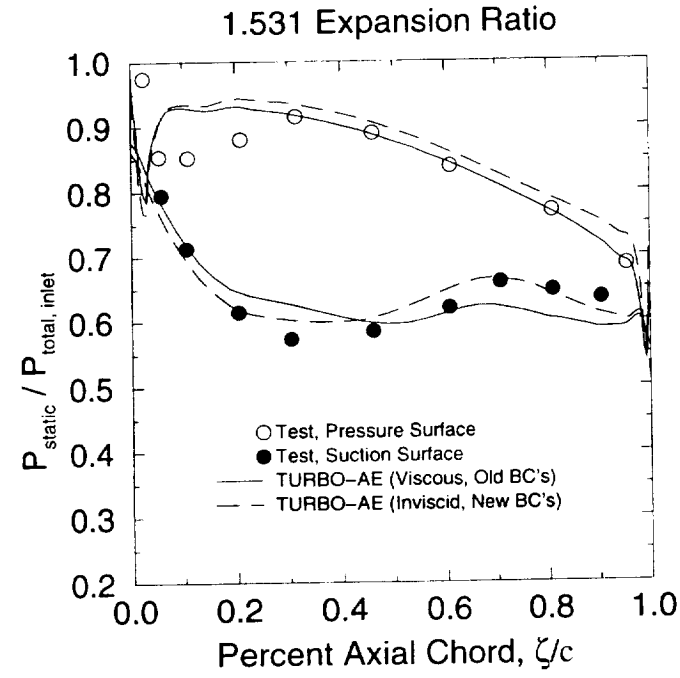

Figure 6.6: Comparison of viscous and inviscid *TURBO-AE* predictions for the 1.531 expansion ratio case.

as a linear perturbation to the steady base flow, typical unsteady periodic boundary conditions are prescribed along the periodic boundaries together with nonreflecting far-field boundary conditions at the inlet and exit planes.

The unsteady pressure response on the blade surface for interblade phase angles of $0, 180, \pm 45$, and ± 90 degrees are shown in Figures 6.7 - 6.12. These figures show the magnitude and phase of the unsteady blade surface pressure as a function of percent axial chord. The normalized unsteady pressure displayed is obtained by dividing the unsteady static pressure by the product of the inlet total pressure and the amplitude of the torsional oscillation.

Inviscid, nonlinear *TURBO-AE* predictions are compared to those obtained from the linear, Navier Stokes predictions of *LNS2D*, and to measurements in Figures 6.7 and 6.8. Referring to these figures, it is seen that the *LNS2D* predictions for the magnitude of the unsteady response are in good agreement with the measurements on the suction surface for both interblade phase angles. The comparison to the measurements near the leading edge of the pressure surface shows poor agreement, but it should be noted that this is a region of separated flow. The steady calculation was performed assuming that the flow was fully turbulent, no attempt was made to model the transition from laminar to turbulent flow. Since the unsteady pressure transducer located at the 30% chord position was not operational, no trend information can be inferred over the mid section of the blade. Therefore, it is difficult to assess how well the predictions are doing in this region of the pressure surface. The inviscid *TURBO-AE* predictions on the suction surface indicate that the unsteady pressure magnitude is being underpredicted over the first 60% of the blade. The trendwise behavior however compares well with the measurements. The pressure side predictions again show a large difference when compared to the measurements in the separated region as would be expected for an inviscid analysis. Over the last 40% of the pressure side, the predictions from both algorithms compare well with the measurements.

The phase predictions from both *TURBO-AE* and *LNS2D* for the 0 degree interblade phase angle case, Figure 6.7, show good agreement with each other and with the measurements on the suction surface, but poor agreement with the measurements aft of the mid-chord on the pressure surface. The phase predictions in Figure 6.8 for the 180 degree interblade phase angle show good trendwise agreement with the data on both surfaces. However, the levels of the *LNS2D* predictions do not agree well with the measurements in the leading edge region. In the trailing edge region the level of the phase prediction is in much better agreement with the data. The *TURBO-AE* phase predictions again show good agreement with the trend of the measurements, but poor agreement with the level of the measurements, particularly in the trailing edge region on both surfaces.

The *LNS2D* code was used to predict the unsteady response resulting from a torsional oscillation with interblade phase angles of ± 45 degrees. The results are compared to measurements in Figures 6.9 and 6.10. Referring to Figure 6.9, which shows the response for a 45 degree interblade phase angle, it will be seen the *LNS2D* predictions for the magnitude of the response do not match the measurements on either the suction or pressure surfaces. The phase angle however shows good trend agreement on both surfaces. The comparison of predicted and measured unsteady phase angle on the pressure surface is very good. However, the maximum difference between the predicted and measured phase on the suction surface is about 50 degrees near the 30% chord position. The reason for the

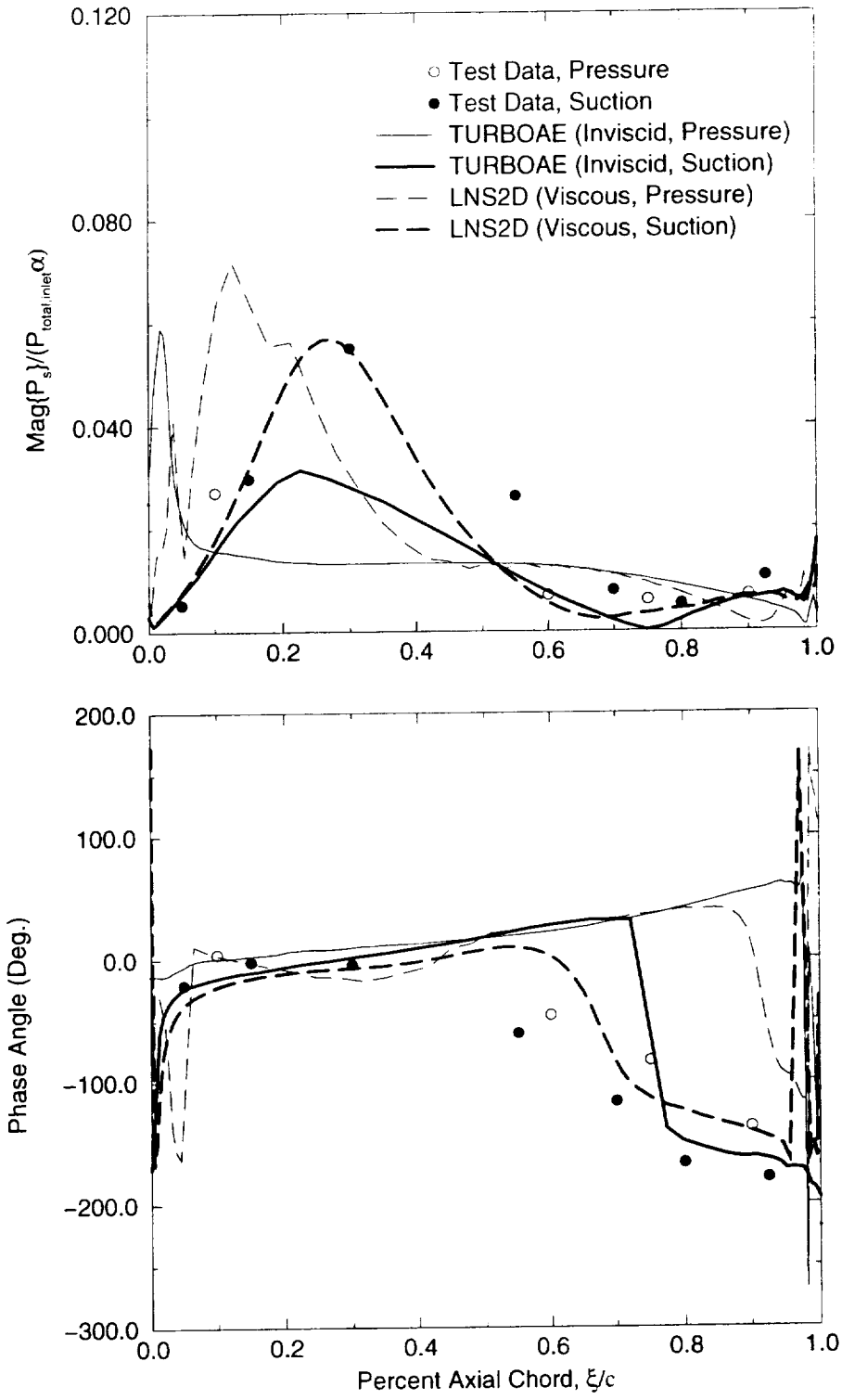

Figure 6.7: Comparison of measured and predicted unsteady pressure response for the turbine cascade vibration in a torsional mode at 340 Hz, 0 degree interblade phase angle, and 1.531 expansion ratio.

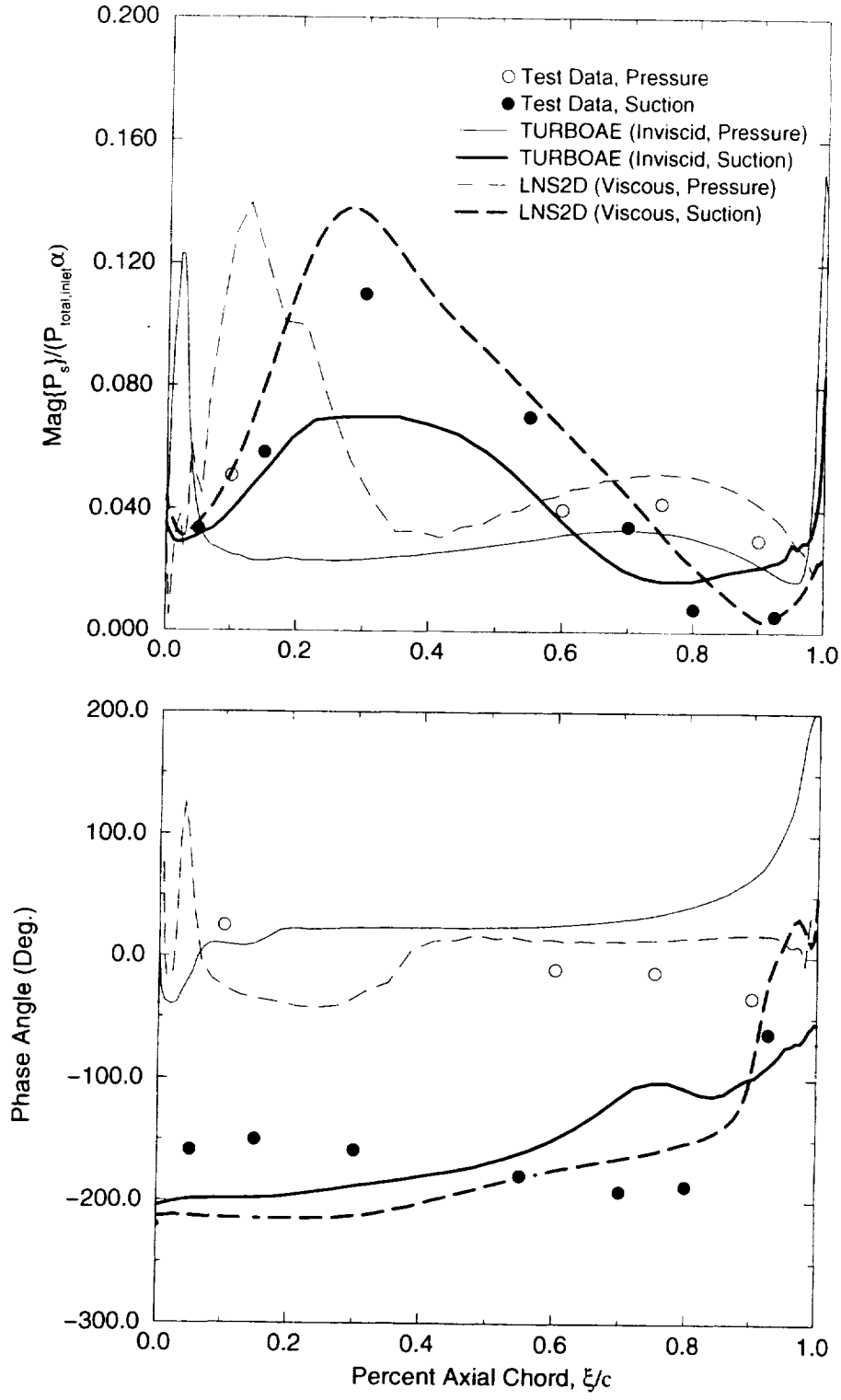

Figure 6.8: Comparison of measured and predicted unsteady pressure response for the turbine cascade vibration in a torsional mode at 340 Hz, 180 degree interblade phase angle, and 1.531 expansion ratio.

discrepancy in the magnitude predictions at this interblade phase angle is not known.

The results in Figure 6.9 for the -45 degree interblade phase angle show quite a different story. In this case, the predicted unsteady pressure magnitude shows excellent agreement with measurements over the entire suction surface. The comparison on the pressure surface in the leading edge region is again clouded by the lack of measurements in the separated region of the flow. The predicted phase angles of the unsteady response again show the same trend as the measurements but differ in level by as much as 50 degrees compared to the measured values.

Comparison of *LNS2D* predictions and measurements for interblade phase angles of ± 90 degrees are shown in Figures 6.11 and 6.12. The predicted magnitude on the suction surface for both interblade phase angles show excellent agreement with the measurements over the entire surface. The pressure surface comparison also shows excellent agreement with the measured values over the aft portion of the blade.

The comparison of the predicted and measured phase angle of the unsteady response for the 90 degree interblade phase angle case, Figure 6.11, shows good agreement on the pressure surface, but only fair agreement on the suction surface. This is especially true over the aft portion of the blade. The comparison of predicted and measured phase angle for the -90 degree interblade phase angle case shows good agreement on both the suction and pressure surfaces.

6.2 Expansion Ratio of 2.713

6.2.1 Steady Flow

The second steady flow condition studied represented a situation in which the exit flow Mach number became supersonic. In this case the cascade expansion ratio was raised to 2.713. The inlet Mach number became 0.52 and the exit Mach number 1.25, see Table 6.1. Predictions for the steady blade surface pressure distribution obtained from *TURBO-AE* and *LNS2D* are compared to measurements in Figure 6.13. Both predictions show excellent agreement with the measured values over most of the blade surface. The exception is in the leading edge region on the suction surface. As was pointed out in Section 6.1.1, this discrepancy occurs in a region in which the steady flow was known to be separated. As such, the inviscid *TURBO-AE* solution would not be expected to match the steady data in this region. The predictions from the linearized Navier-Stokes analysis show better agreement with the data but still overpredict the static pressure in the separated region. No attempt was made to study the effect of moving the transition point on the flow behavior in this region. The analysis was performed assuming fully turbulent flow. The steady Mach number contours obtained from the *TURBO-AE* solution are shown in Figure 6.14. These contours clearly show the trailing oblique shock extending downstream to the exit boundary. The convergence history for the *TURBO-AE* solution is shown in Figure 6.15. The upper plot in this figure shows the ratio of the exit to inlet mass flow rate. As can be seen, the flow converges after about 1400 time steps.

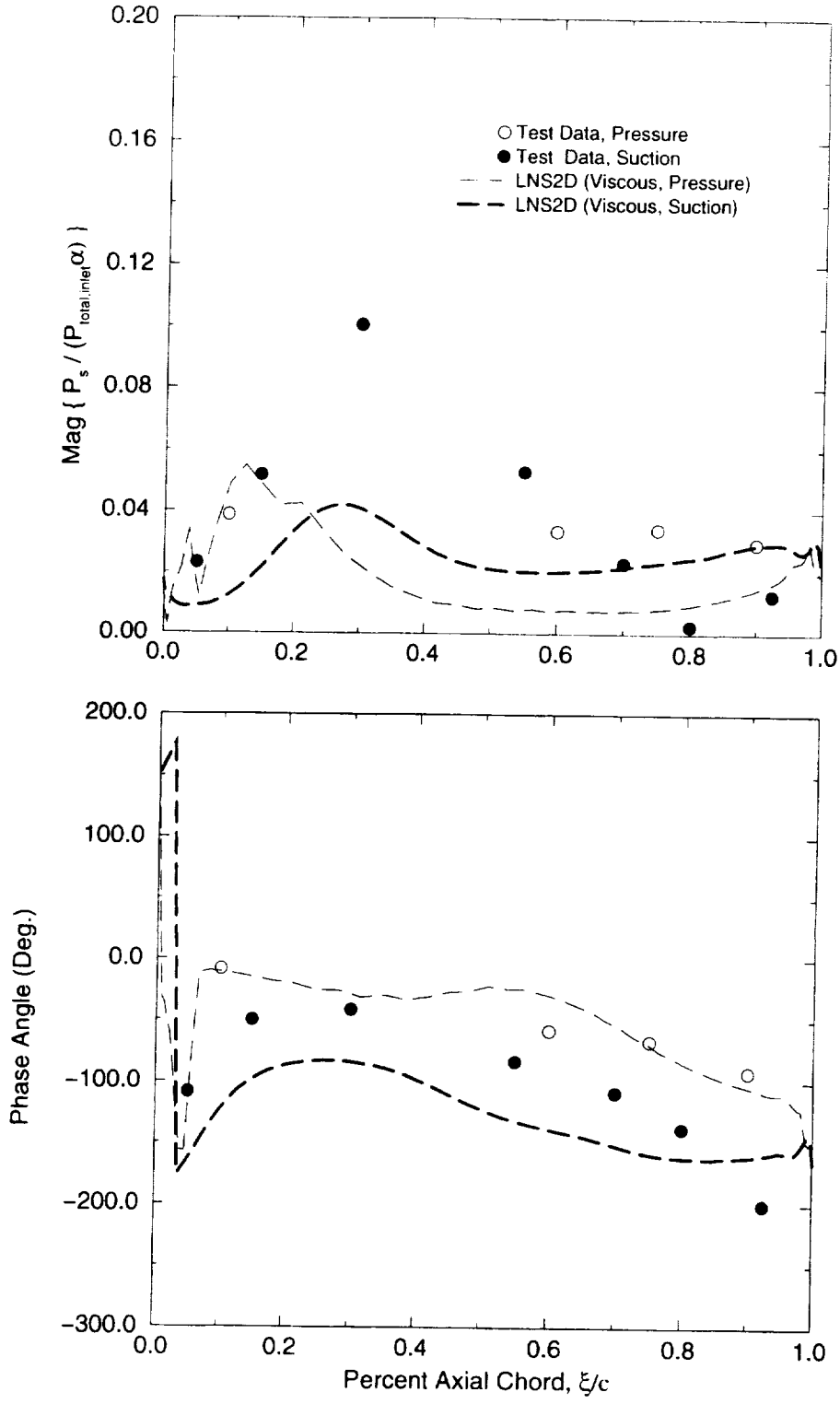

Figure 6.9: Comparison of measured and predicted unsteady pressure response for the turbine cascade vibration in a torsional mode at 340 Hz, 45 degree interblade phase angle, and 1.531 expansion ratio.

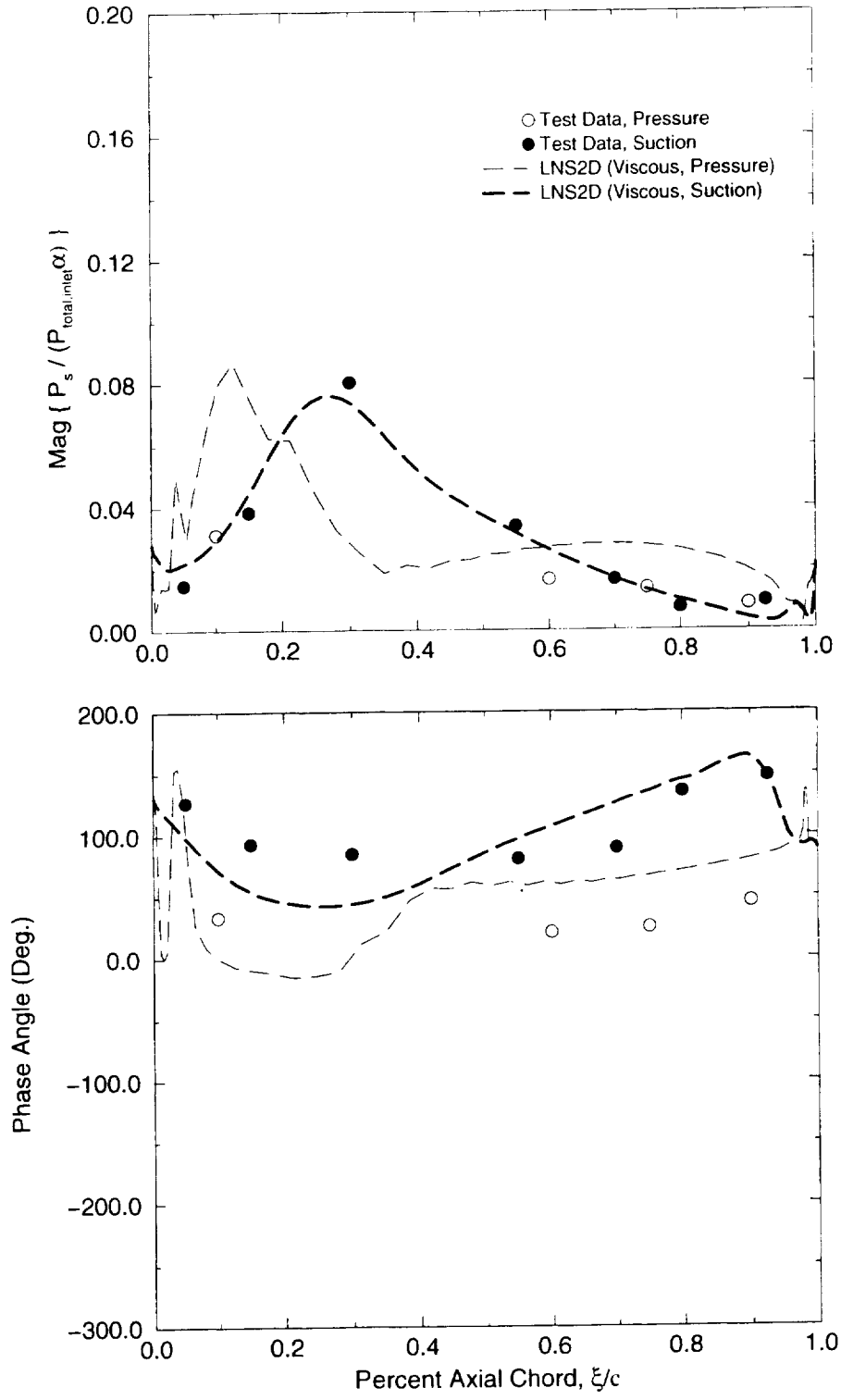

Figure 6.10: Comparison of measured and predicted unsteady pressure response for the turbine cascade vibration in a torsional mode at 340 Hz, -45 degree interblade phase angle, and 1.531 expansion ratio.

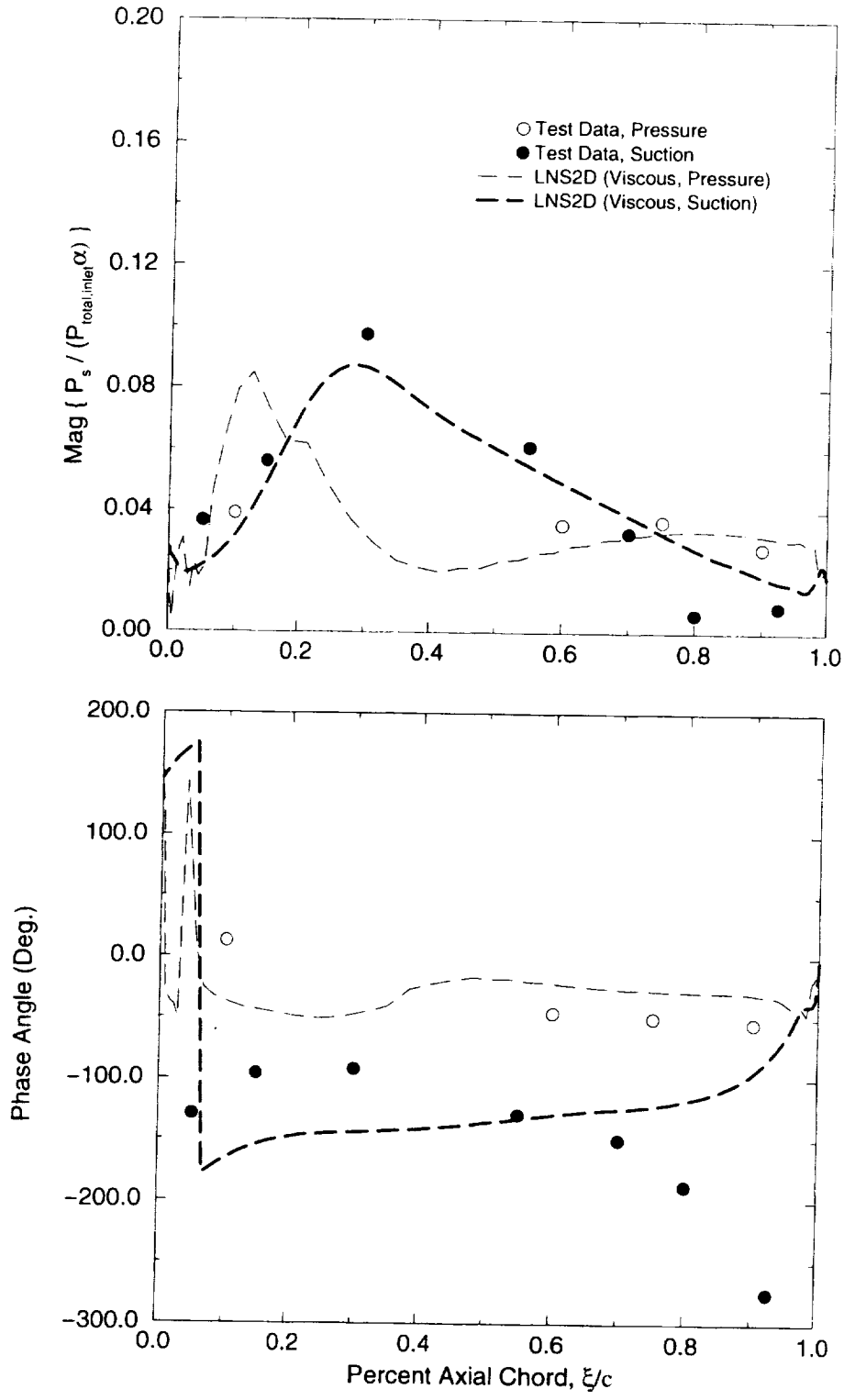

Figure 6.11: Comparison of measured and predicted unsteady pressure response for the turbine cascade vibration in a torsional mode at 340 Hz, 90 degree interblade phase angle, and 1.531 expansion ratio.

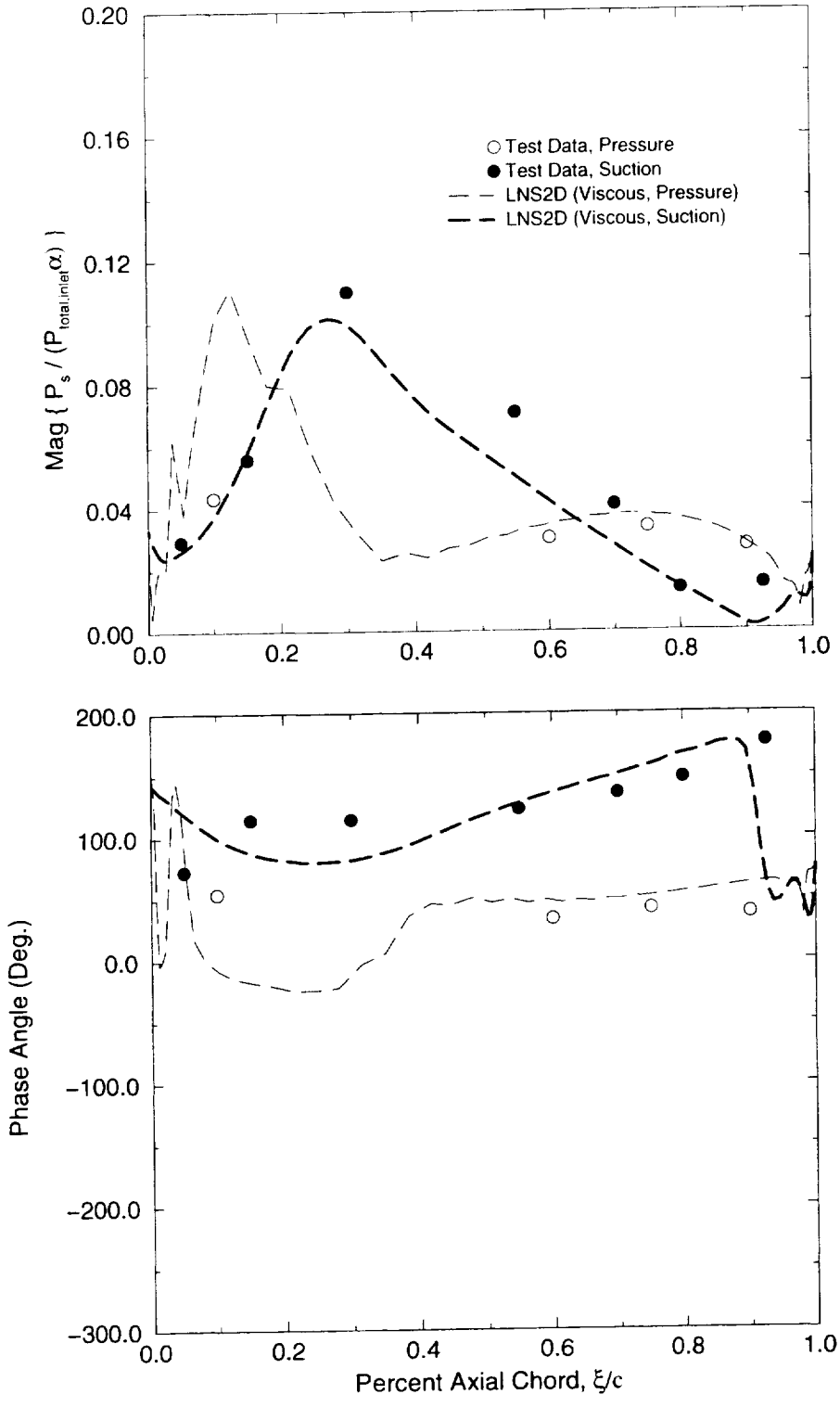

Figure 6.12: Comparison of measured and predicted unsteady pressure response for the turbine cascade vibration in a torsional mode at 340 Hz, -90 degree interblade phase angle, and 1.531 expansion ratio.

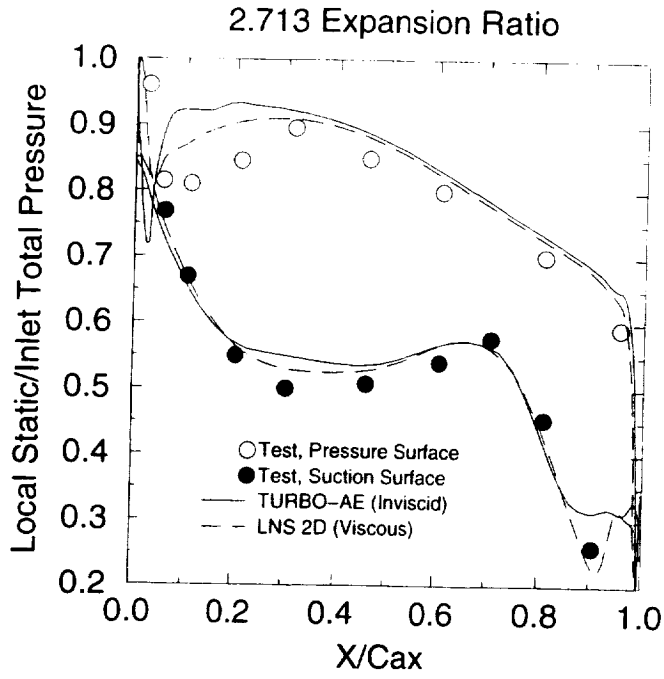

Figure 6.13: Comparison of steady blade loading as a function of axial chord lengeh, Cax, predicted by *TURBO-AE* and *LNS2D* with measurements for the 2.713 expansion ratio flow.

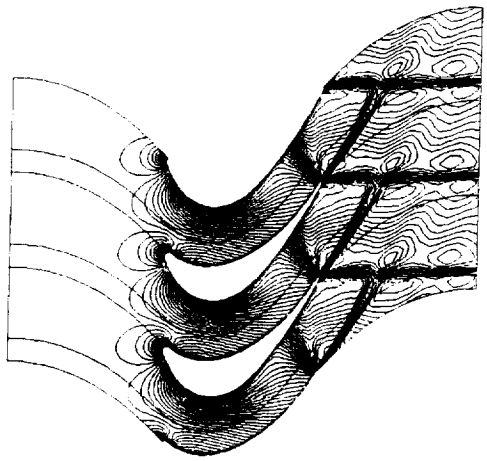

Figure 6.14: Steady Mach number contours obtained from the *TURBO-AE* solution for the 2.713 expansion ratio.

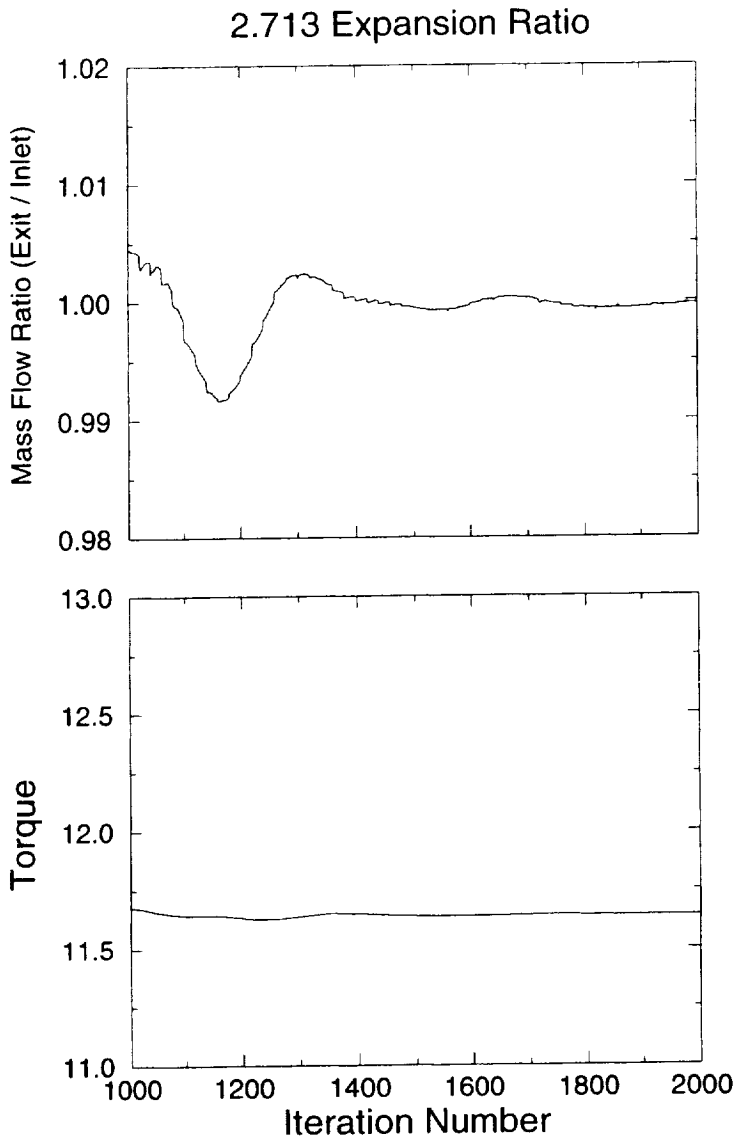

Figure 6.15: Convergence history for the *TURBO-AE* solution, 2.713 expansion ratio.

6.2.2 Unsteady Flow

The steady flow conditions predicted by both the *TURBO-AE* and *LNS2D* codes, discussed in Section 6.2.1, were used as the base flow from which unsteady calculations were performed. The unsteady predictions are compared to measurements in Figures 6.16 to 6.21. The unsteady response was the result of a prescribed torsional displacement at 340 Hz and prescribed interblade phase angles of 0, 180, ±45, and ±90 degrees.

Unsteady predictions obtained from *TURBO-AE* , and *LNS2D*, for 0 and 180 degrees interblade phase angles are compared to measurements in Figures 6.16, and 6.17, respectively. The 0 degree interblade phase angle results, Figure 6.16, indicate that the *LNS2D* results for the unsteady pressure magnitude more closely match those of the measurements than do the *TURBO-AE* results. In particular, the *LNS2D* predictions of the unsteady pressure magnitude on the suction surface show good agreement with the data, whereas the *TURBO-AE* results underpredict the magnitude of the unsteady response. On the pressure surface, both codes predict the same level of unsteady response aft of mid chord. However, over the front half of the pressure surface, both codes predict quite different behavior. The *LNS2D* predictions show a maximum in the unsteady magnitude at about the 28% chord position. The *TURBO-AE* predictions, while showing the same level in the unsteady magnitude, indicate the the maximum is achieved at about 2% chord. As was pointed out in Section 6.1.2, the flow is separated over the first 30% of the suction surface, and the unsteady pressure measurements were sparse since a transducer located at the 30% chord location was not working. In the trailing edge region of the suction surface, both codes missed the measured increase in unsteady pressure magnitude aft of the point where the trailing edge shock intersects the blade.

Unsteady phase angle predictions from *TURBO-AE* and *LNS2D* are also shown in Figures 6.16 and 6.17. In this case, both sets of predictions show a good comparison with the measured data. The exception to this observation is in the leading edge region of the suction surface where the measurements differ from both predictions by as much as 150 degrees.

In addition to the 0 and 180 degree interblade phase angle prediction discussed above, *LNS2D* was also used to calculate the unsteady response to ±45, and ±90 degree interblade phase angles. The magnitude and phase angle of the unsteady blade surface response for these interblade phase angles are shown in Figures 6.18 - 6.21.

The predicted unsteady responses for ±45 degree interblade phase angles are shown in Figures 6.18 and 6.19. Referring to the magnitude plots of the unsteady pressure, it is seen that *LNS2D* underpredicts the magnitude over most of the suction surface for both interblade phase angles. The location of the intersection of the trailing edge shock with the suction surface is well predicted for both interblade phase angles. However, the -45 degree results show much better agreement with measurements than was obtained for the 45 degree interblade phase angle case. Comparison of the predicted and measured unsteady pressure magnitude in the trailing edge region of the pressure surface shows that the magnitude is underpredicted for the 45 degree case and overpredicted for the -45 degree case.

The comparison of predicted and measured unsteady phase angle for the 45 degree interblade phase angle case is shown in Figure 6.18. The agreement between the two is

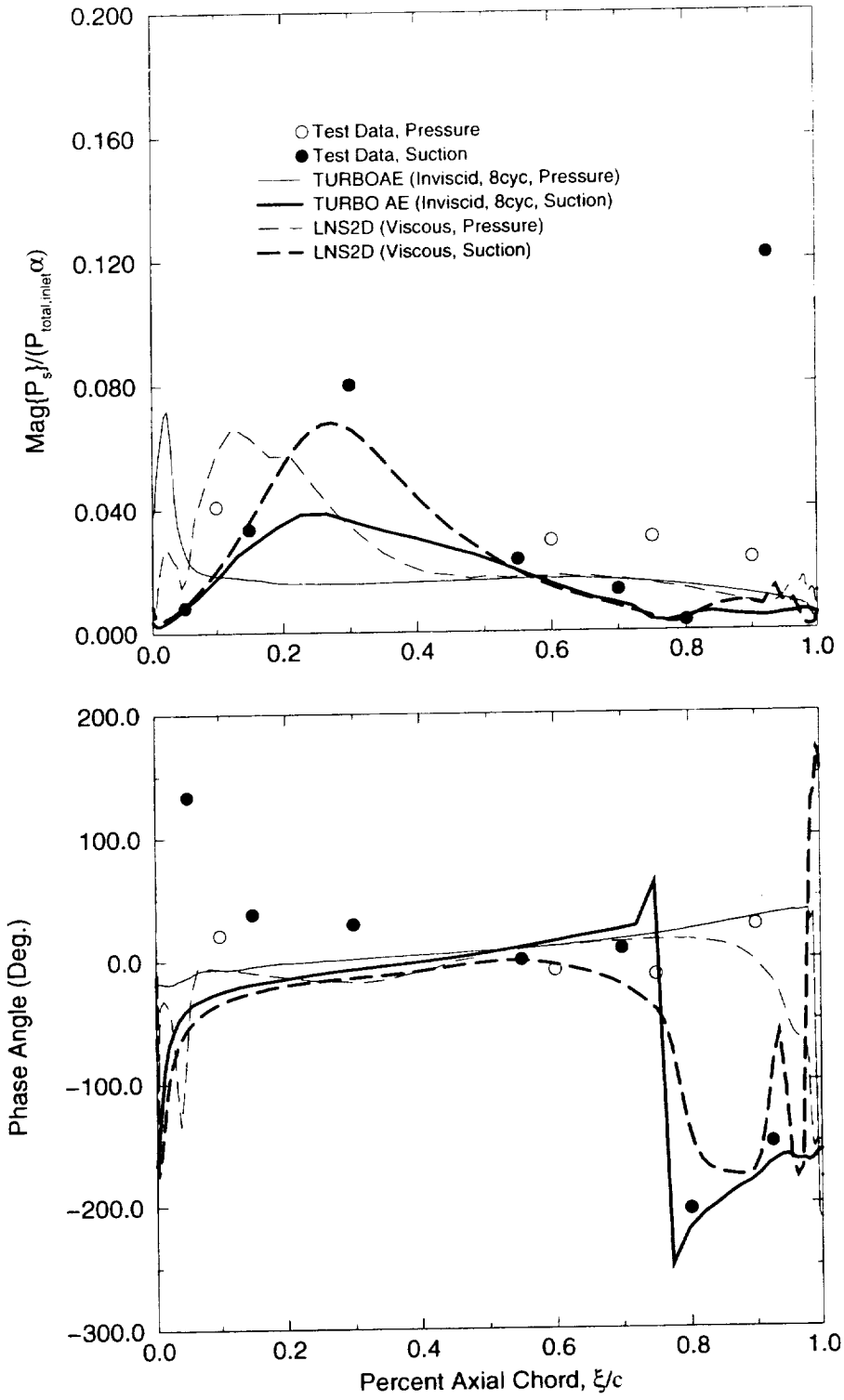

Figure 6.16: Comparison of blade surface unsteady response predictions obtained from *TURBO-AE* and *LNS2D* with measurements for a torsional oscillation at 340 Hz, and an interblade phase angle of 0 degrees, and 2.713 expansion ratio.

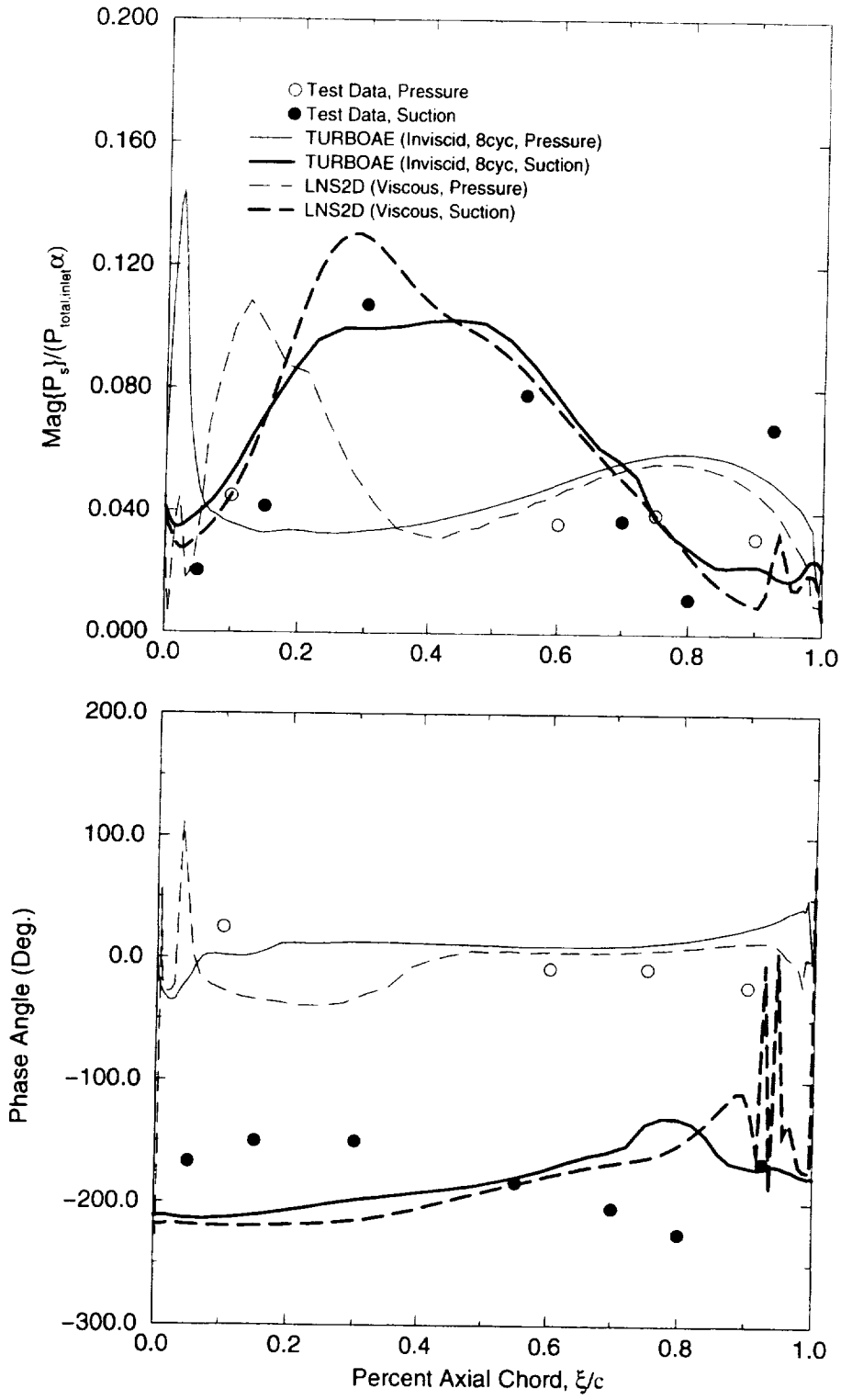

Figure 6.17: Comparison of blade surface unsteady response predictions obtained from *TURBO-AE* and *LNS2D* with measurements for a torsional oscillation at 340 Hz, and an interblade phase angle of 180 degrees, and 2.713 expansion ratio.

good over the last half of the suction surface and over all of the pressure surface. Differences of 50 degrees can be seen over the first half of the suction surface. The -45 degree interblade phase range results indicate that the phase angle was not well predicted over the suction surface. The pressure surface phase angle predictions are in better agreement with the measurements, a difference of about 30 degrees being observed.

The last two conditions investigated with *LNS2D* was for interblade phase angles of ±90 degrees. Comparisons of the predicted magnitude and phase of the blade surface unsteady pressure with measurements are shown in Figures 6.20 and 6.21. The predicted unsteady pressure magnitudes for both interblade phase angles are in very good agreement with measurements on both surfaces. The unsteady phase angle predictions show good agreement with regard to the trend of the measurements but differ by as much as 75 degrees in some locations on the blade surface.

6.3 Aerodynamic Damping

In the case of a flutter analysis, the critical parameter that must be determined is the level of aerodynamic damping acting on the individual blades, see references [16] and [17]. The aerodynamic damping is a measure of the energy absorbed or removed by a blade as it vibrates in a given mode. If energy is absorbed, the vibration level increases and can become unstable resulting in a flutter condition. If energy is dissipated, the blade vibration level will decrease resulting in stable operation. Aerodynamic damping is related to the work per cycle performed on the blade as it vibrates. The relationship is given below,

$$\delta_{aero} = -\frac{n\Xi}{4K_e}, \tag{6.1}$$

where, δ_{aero} is the aerodynamic damping, n the number of blades on the disk, and K_e the kinetic energy of the system. Referring to equation 6.1, a negative value of work per cycle results in a positive value of aerodynamic damping which is considered stabilizing. A positive value for work per cycle results in negative aerodynamic damping value which is considered unstable.

Unsteady pressure predictions for both expansion ratios were used to calculate the unsteady work per cycle as a result of the torsional motion of the blade. Figure 6.22 shows the resulting aerodynamic work per cycle as a function of interblade phase angle. The higher expansion ratio case is shown to be unstable over a range of interblade phase angles between 0 and 90 degrees, while the lower expansion ratio case was determined to be unstable between 0 and 50 degrees. The inflection point in the low pressure ratio curve in the vicinity of 55 degrees is the result of the calculation being performed near an acoustic resonance point associated with the exit Mach number. No work per cycle calculations based on the measured data have been included in Figure 6.22 because none were reported at the time that the measurements were made. Due to the lack of data on the pressure surface any attempt to integrate the measured pressures to obtain work per cycle values would not be accurate. One interesting result shown in Figure 6.22 is that both expansion ratios exhibit very similar stability characteristics even though their steady loadings differ substantially over the aft 20% of the suction surface due to the presence of trailing edge shock in the high expansion ratio case. This similarity is due to the relatively weak influence of the unsteady shock loading for this mode shape and flow configuration.

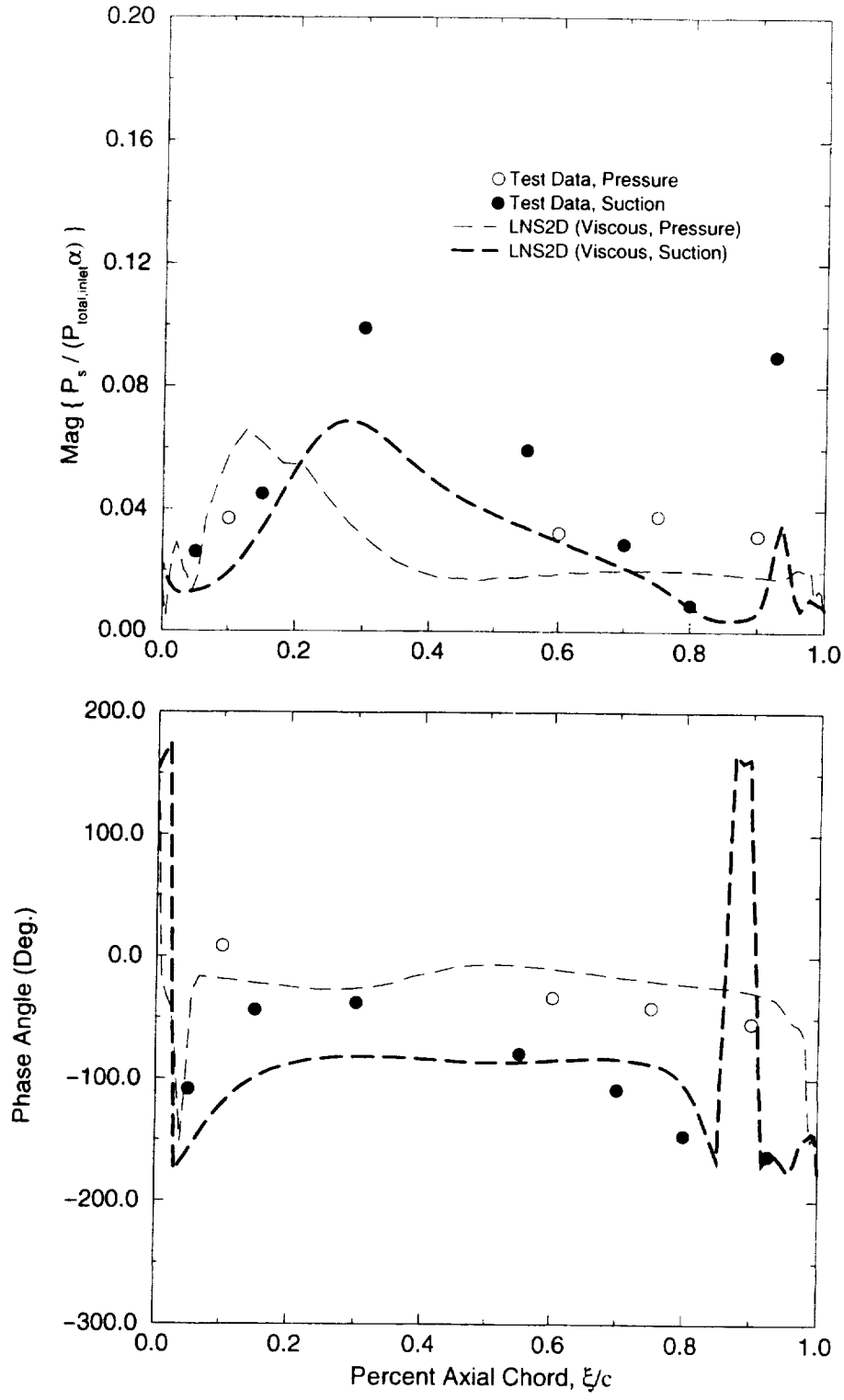

Figure 6.18: Comparison of blade surface unsteady response predictions obtained from *TURBO-AE* and *LNS2D* with measurements for a torsional oscillation at 340 Hz, and an interblade phase angle of 45 degrees, and 2.713 expansion ratio.

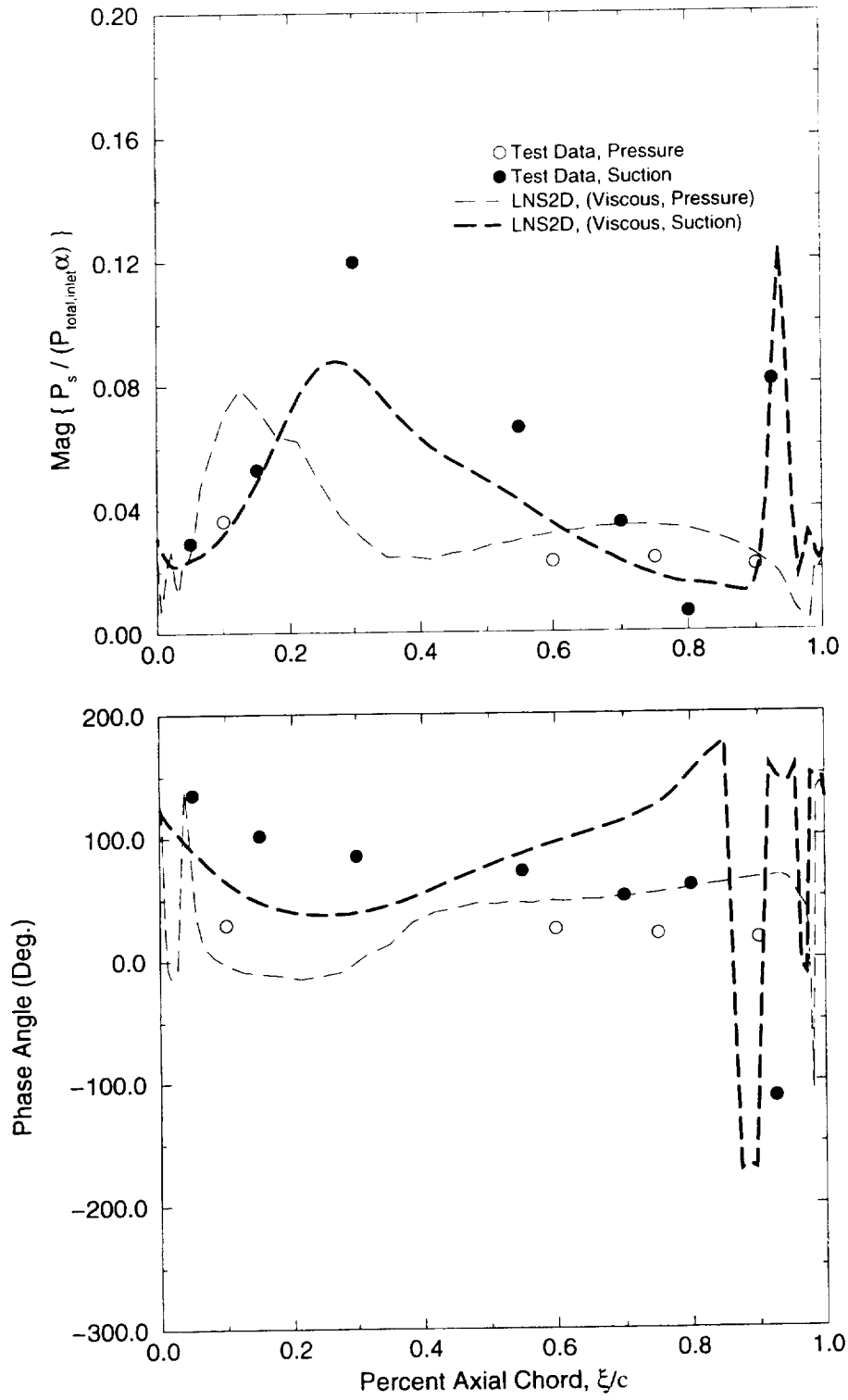

Figure 6.19: Comparison of blade surface unsteady response predictions obtained from *TURBO-AE* and *LNS2D* with measurements for a torsional oscillation at 340 Hz, and an interblade phase angle of -45 degrees, and 2.713 expansion ratio.

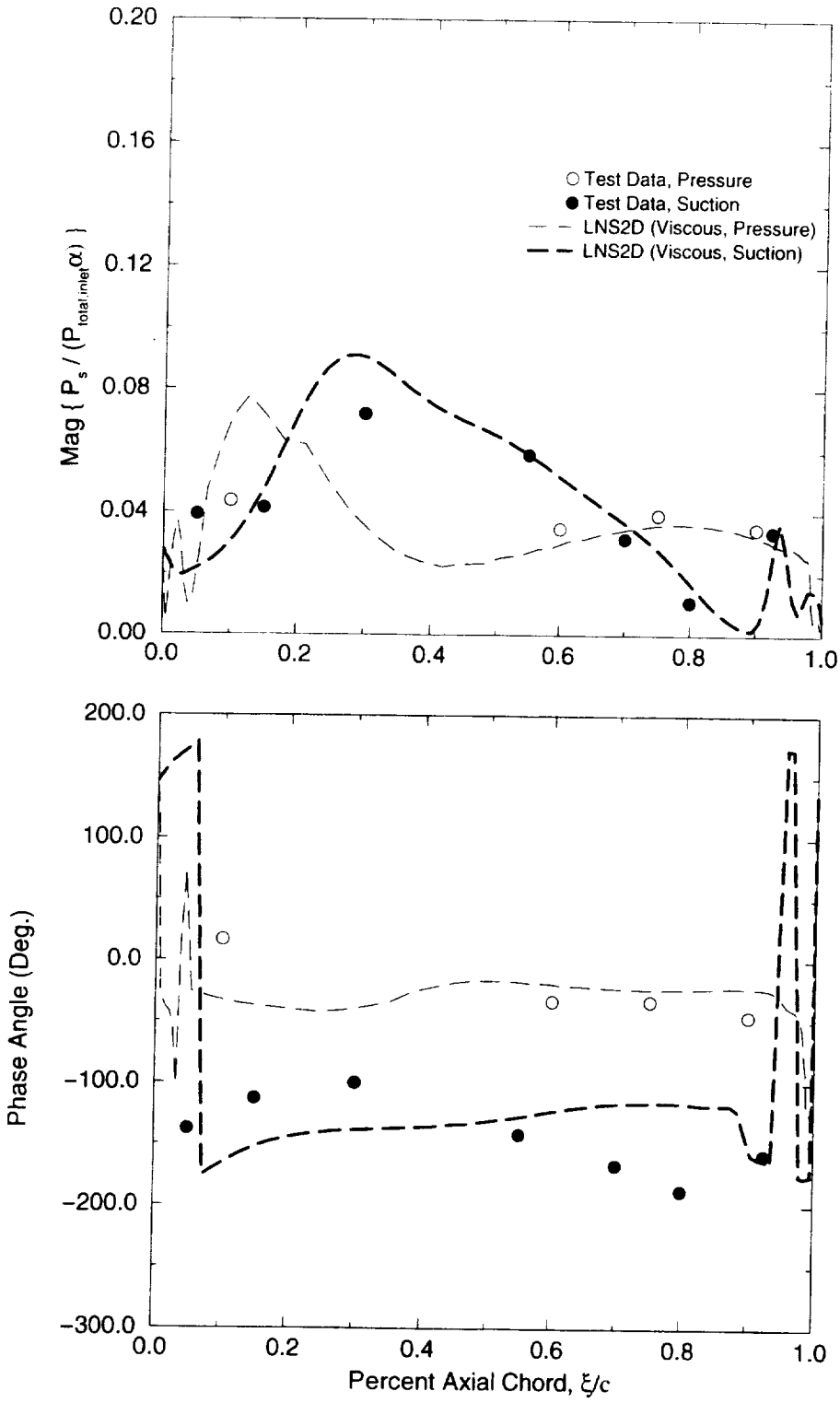

Figure 6.20: Comparison of blade surface unsteady response predictions obtained from *TURBO-AE* and *LNS2D* with measurements for a torsional oscillation at 340 Hz, and an interblade phase angle of 90 degrees, and 2.713 expansion ratio.

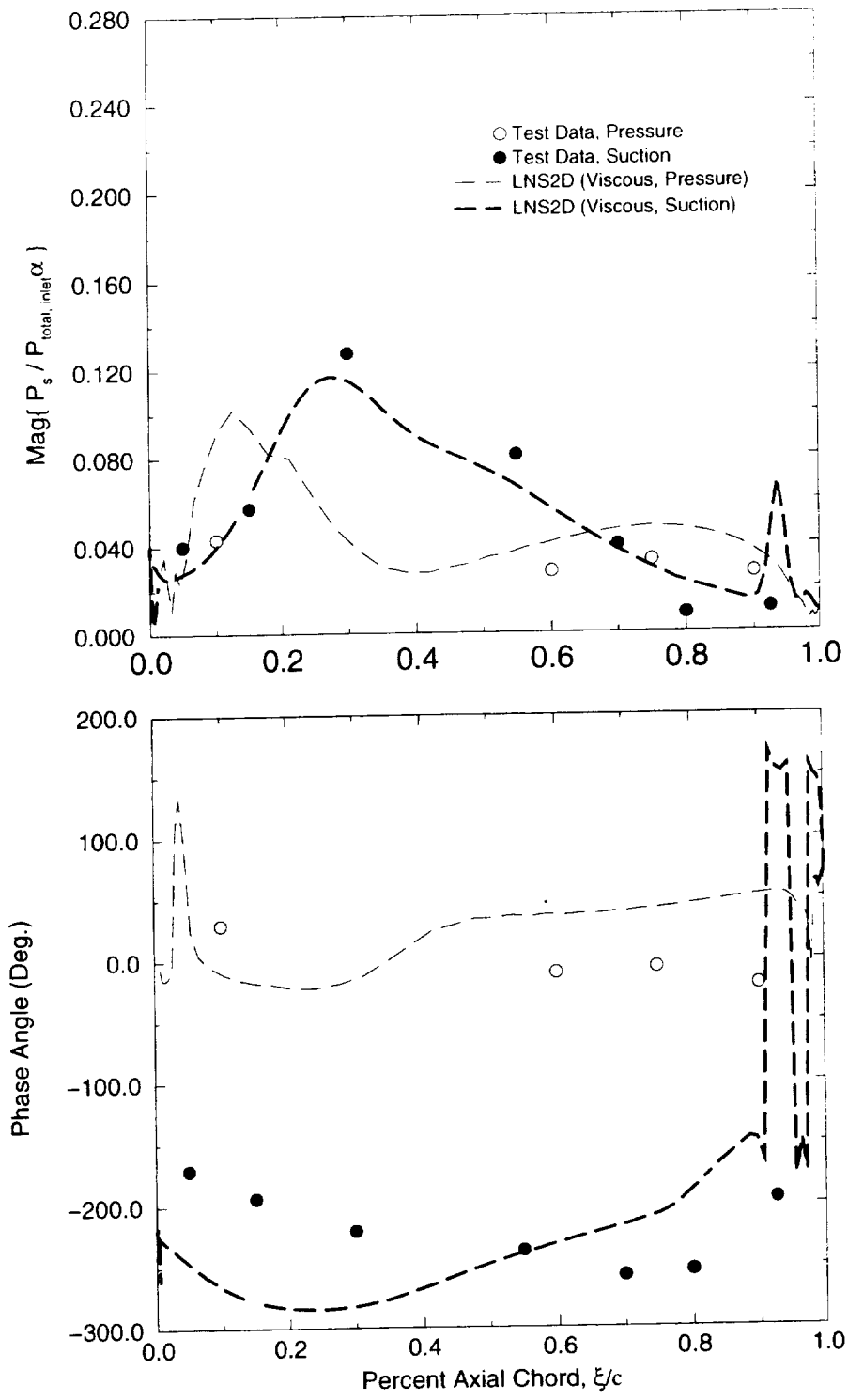

Figure 6.21: Comparison of blade surface unsteady response predictions obtained from *TURBO-AE* and *LNS2D* with measurements for a torsional oscillation at 340 Hz, and an interblade phase angle of -90 degrees, and 2.713 expansion ratio.

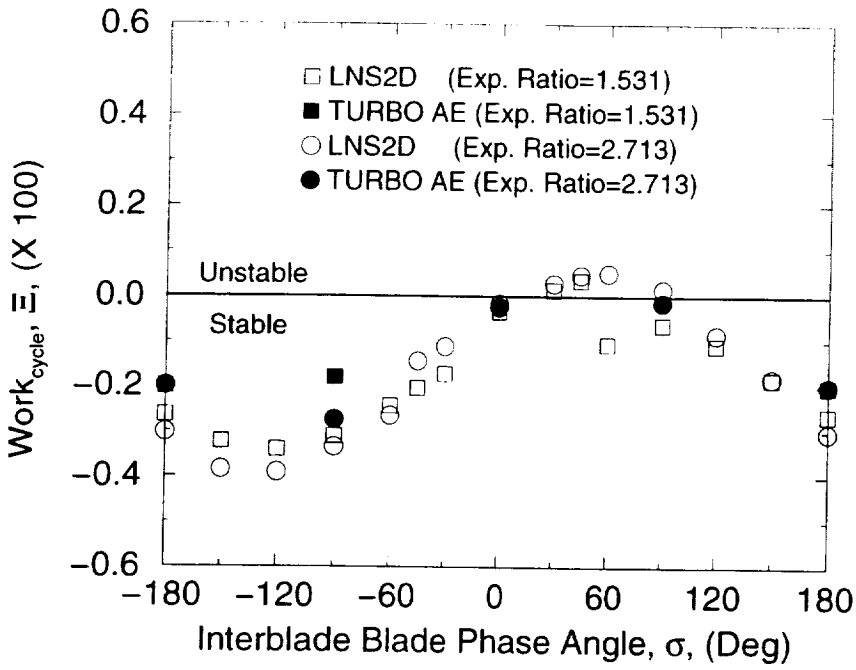

Figure 6.22: Unsteady aerodynamic work-per-cycle prediction for turbine cascade for 1.531 and 2.713 expansion ratios.

6.4 Conclusions

The *TURBO-AE* and *LNS2D* algorithms were used to predict the steady and unsteady behavior of a linear cascade of turbine airfoils. Two cascade expansion ratios were examined: one in which the steady flow was completely subsonic and the other in which the exit velocity was supersonic. For both expansion ratios, unsteady response predictions were made over a range of interblade phase angles for a rigid body torsional motion of the airfoils. The torsional frequency was 340Hz.

The steady predictions from *TURBO-AE* and *LNS2D* were in excellent agreement with the measurements on the suction and pressure surfaces for both expansion ratios. The exception to this statement was in the leading edge region of the suction surface where the flow was shown to be separated during the experimental program.

The agreement between the unsteady predictions from both algorithms and the measured data showed a dependence on the interblade phase angle being analyzed. In the case of the *LNS2D* predictions the magnitude for the most part was well predicted on the suction surface for the 1.531 expansion ratio case. The predictions in the trailing edge region of the pressure were not as well predicted. However this could be the result of low levels of measured data and the associated problems with determining phase angle for the measured signals. The code also had some problems in predicting the pressure rise through the reflected shock on the suction surface for the high expansion ratio. This could be an indication that the linear model is having problems with this type of condition.

The phase prediction from *LNS2D* also showed a strong dependance on the

interblade phase angle being investigated. In some cases, the phase magnitude was well predicted and in others the phase was off by as much as 100 degrees.

Comparison of the inviscid *TURBO-AE* unsteady predictions with measurements and with *LNS2D* results were made only for a few interblade phase angles. These comparisons showed that *TURBO-AE* tended to underpredict the magnitude of the unsteady pressure. The exception to this being the 180 degree interblade phase angle case for the high expansion ratio where the magnitude was very well predicted. The *TURBO-AE* predicted phase angle tended to match those obtained from *LNS2D*. As such the agreement with the measurements showed a strong dependence on the interblade phase angle being considered. The reason for the good agreement with measurements in some cases and poor agreement in others is not clear. One possibility is the behavior of the non-reflective boundary conditions at the inlet and exit. These boundary conditions are sensitive to the wave number of the disturbance impinging on the boundary. As such for some flow conditions unsteady disturbances may be reflected back into the computation domain. This aspect of unsteady modeling needs to be studied in more detail if modeling capability is to be improved.

The unsteady work-per-cycle predictions for both expansion ratios showed remarkably similar behavior, indicating that for this turbine cascade, the steady loading had very little impact on the unsteady response. This is a surprising result and would need to be further studied to determine the underlying physics of this finding.

Chapter 7

Task 3: Transonic Fan

The objective of Task 3 was to investigate the aeromechanical stability of an existing transonic fan design using the *TURBO-AE* code. The fan selected for this purpose was the first stage fan of the TF41-A100 rig. This fan rig consisted of a two-stage low pressure compressor and a three-stage intermediate compressor. The first stage fan consisted of 25 unshrouded blades. A description of the rig and a brief history of the testing program were given in Section 3.2 of Chapter 3. During the initial build, both the first and second-stage fan blades experienced high stress levels at points just above the sea level working line. The first-stage fan fluttered in a four nodal diameter mode (57.6 degrees) at its first torsion frequency at a point along the 100% speed line, while the second stage fan exhibited flutter in its second bend mode at a point along the 105% speed line. The first-stage fan was selected for this study because it provided the best test case for exercising the single blade row analysis capability of *TURBO-AE* .

Since no on-blade unsteady pressure instrumentation was used during the rig test program, the capability of *TURBO-AE* to predict flutter will be assessed by performing an unsteady analysis at a point on the 100% speed line which was known to exhibit flutter behavior. As flutter was expected to occur along the 100% speed line at a point just above the standard sea level working line, an inviscid *TURBO-AE* was thought to be adequate. Stability of the fan was determined by computing the unsteady aerodynamic work performed on the blade over one cycle of oscillation. If the unsteady aerodynamic work has a negative sign associated with it the unsteady flow will be doing work on the blade and this could result in a flutter condition. Flutter will occur only if the energy input by the unsteady aerodynamic work overcomes any energy dissipated by the blade structural and material damping. No estimate of the blade structural and material damping properties was obtained during the rig test. As such, for the purpose of this task, flutter behavior was assessed by looking only at the sign of the unsteady aerodynamic work-per-cycle.

A flutter calculation was also performed using a set of in-house programs, *ADPAC* [13] and *SLiQ* [12]. The *ADPAC*program provides a steady baseline flow which is used by *SLiQ*to perform a linear, unsteady, inviscid analysis. The *SLiQ*unsteady analysis can use the results of either an inviscid or viscous steady solution from *ADPAC*. Both approaches were used in this study. The unsteady predictions obtained from *TURBO-AE* are compared with those obtained from *SLiQ*in order to provide an assessment of the importance of nonlinear unsteady effects on flutter behavior.

7.1 Steady Flow: Flutter Point

This section covers the results obtained from a steady flow analysis using the *TURBO-AE* and *ADPAC* algorithms. The *TURBO-AE* analysis was only performed using the inviscid flow assumption, while both viscous and inviscid analyses were performed using *ADPAC*.

The inviscid, steady flow analysis obtained using the *TURBO-AE* code was performed on a typical H mesh which consisted of 141 points in the axial direction, 17 uniformly spaced point along the blade from hub-to-tip, and 49 points in the blade-to-blade direction. A portion of the mesh showing a constant radius plane (constant j indices) at 75% span and the mesh on both the suction and pressure surfaces are shown in Figure 7.1. The leading and trailing edges of the blade were modeled using constant radius circles. No attempt was made to modify the trailing edge geometry into a wedge to accommodate the inviscid flow analysis. This same mesh was also used for the inviscid *ADPAC* predictions. The mesh used for the viscous *ADPAC* predictions had the same number of points in the axial and blade-to-blade directions, 141 and 49 respectively. However, in order to resolve the boundary layers along the hub and casing flow paths, the number of grid points in the radial direction was increased from 17 to 45, and the mesh clustered at the hub and casing boundaries. A comparison of the inviscid and viscous meshes on the suction surface of the blade is shown in Figure 7.2. In both the inviscid and viscous grids no blade tip gap was included. The blade was allowed to slide along the tip casing.

The predicted 100% speed characteristic obtained from the viscous *ADPAC* and inviscid *TURBO-AE* codes are compared to the flutter and nonflutter points obtained from rig testing in Figure 7.3. The viscous *ADPAC* predictions do a good job of matching the mass flow and pressure rise across the fan. The rig flutter and nonflutter points shown in Figure 7.3 were obtained from a through flow analysis in which the measured inlet and exit conditions across the whole rig were matched. The *ADPAC* analysis was performed using a radial equilibrium exit boundary condition together with the Spalart-Allmaras turbulence model. The points closest to the rig operating points were used in the subsequent *SLiQ* analysis.

Initial attempts to use *TURBO-AE* to predict the steady, inviscid behavior along the 100% speed line were not successful. The analysis in this case was initialized assuming uniform flow together with specifying the exit static pressure at the hub location of the exit plane. While the flow would converge for the specified exit pressure, the corresponding point on the operating map would indicate a much lower pressure ratio and mass flow rate than was observed in either the rig or *ADPAC* solutions. In addition, convergence was very slow, requiring a large number of time steps (on the order of 20,000) to converge the solution. It should be noted that convergence was based on obtaining a value of unity for the ratio of the exit-to-inlet mass flow for at least 500 iterations.

In an attempt to overcome this starting problem, it was decided to initialize the *TURBO-AE* analysis with a solution obtained from *ADPAC*. The *TURBO-AE* code was modified to input an *ADPAC* restart file and use it to initialize the flow. An *ADPAC* inviscid analysis was performed using the exit static pressure obtained from the viscous *ADPAC* analysis at the flutter point. The mesh used was identical to the mesh used

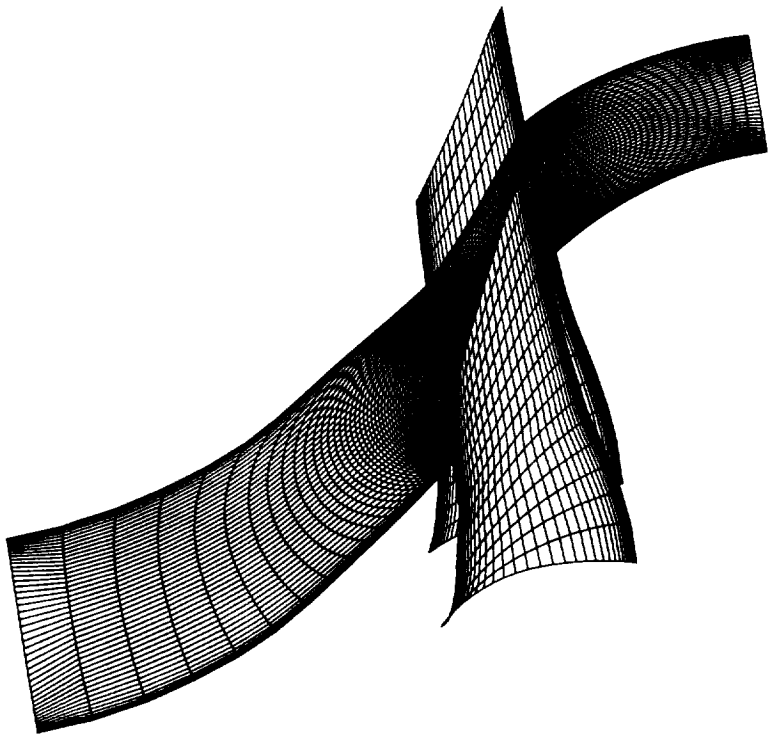

Figure 7.1: Typical single block, H mesh used in steady, inviscid *TURBO-AE* and *AD-PAC* analyses of the TF41-A100 first stage fan, only the mesh along the blade surface and a single, constant radius plane at 75% span is shown for clarity.

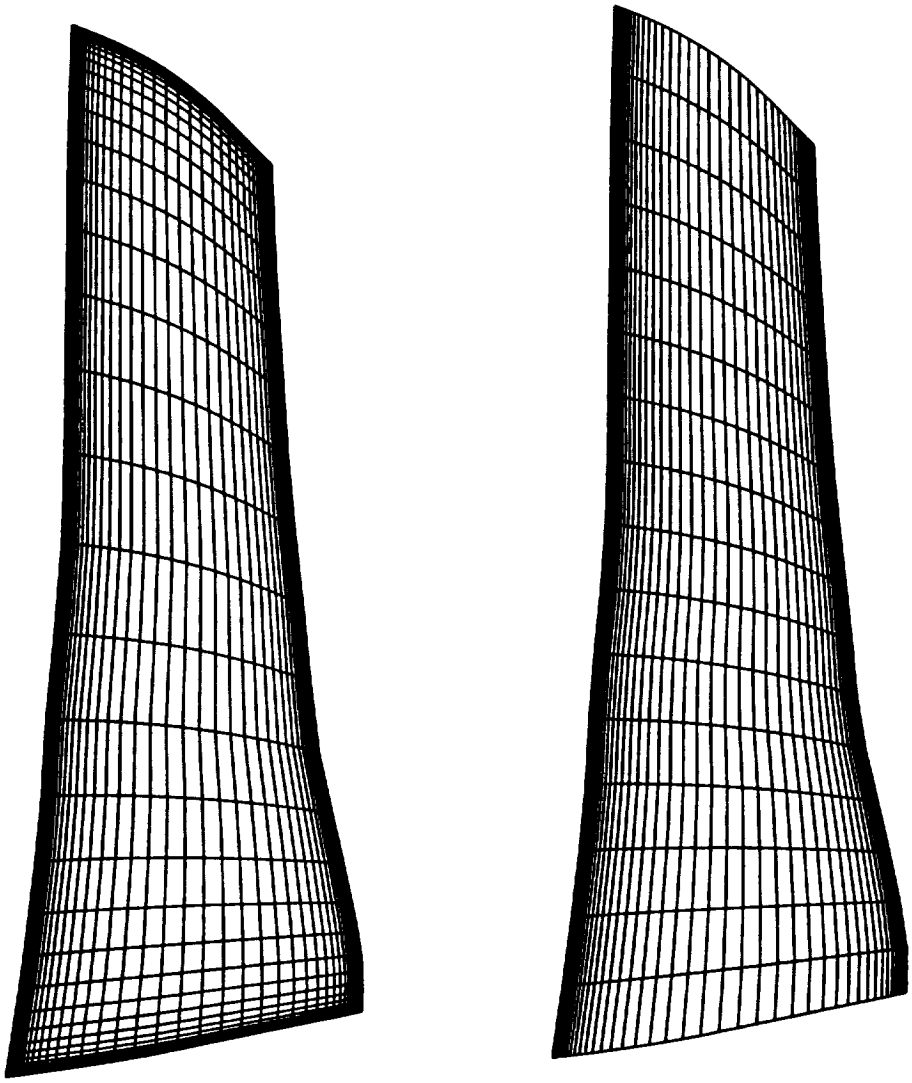

Figure 7.2: Comparison of the mesh used for the viscous (left) and inviscid (right) steady *ADPAC* analysis of the TF41-A100 first stage fan, only the mesh along the blade suction surface is shown for clarity.

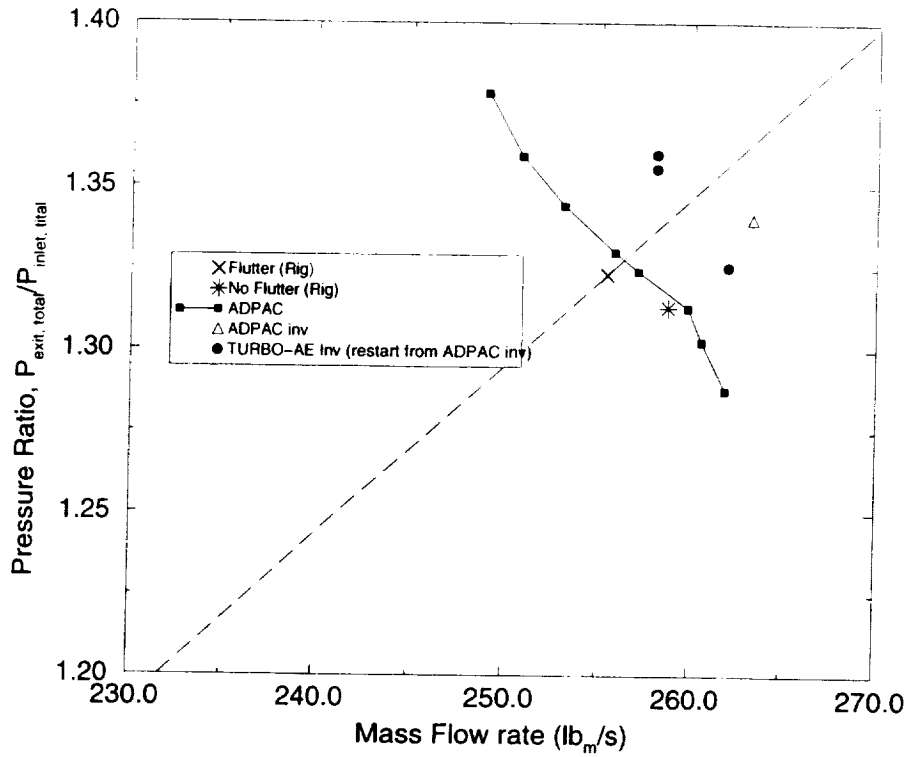

Figure 7.3: Comparison of predicted 100% speedlines from *ADPAC* and *TURBO-AE*.

for the *TURBO-AE* analysis. This was done to avoid the need for performing an interpolation from the *ADPAC* to the *TURBO-AE* mesh. The change in the flutter point from the viscous to the inviscid *ADPAC* analysis is shown in Figure 7.3. As can be seen the inviscid flutter point moved to a higher mass flow and slightly higher pressure ratio than was observed for the viscous results. This is consistent with the reduced blockage associated with the inviscid flow. No attempt was made to adjust the back pressure to match the viscous results. The three operating points obtained from *TURBO-AE* were predicted using the inviscid *ADPAC* results as the starting point. The procedure of using an inviscid *ADPAC* solution to initialize the *TURBO-AE* analysis resulted in a much better match of the rig operating conditions than was obtained from the previous approach of using a uniform flow to initialize the *TURBO-AE* analysis.

The predicted steady blade surface pressure distributions obtained from the two algorithms used in this study are shown in Figures 7.4, 7.5, and 7.6, for the 50%, 75%, and 88% span locations respectively. Predictions in these figures correspond to points on the fan operating map that are closest to the rig measured flutter point. The three sets of curves are obtained from a viscous *ADPAC* solution, an inviscid *ADPAC* solution, and an inviscid *TURBO-AE* solution that was initialized using the inviscid *ADPAC* solution. As can be seen both inviscid predictions are in good agreement with each other. Comparing the viscous and inviscid results, it will be noticed that the main difference is in location of the shocks on the suction surface and in the magnitude of the pressure in the leading edge region of the pressure surface. The difference between the viscous and inviscid pressure surface predictions increases as a function of increasing span location.

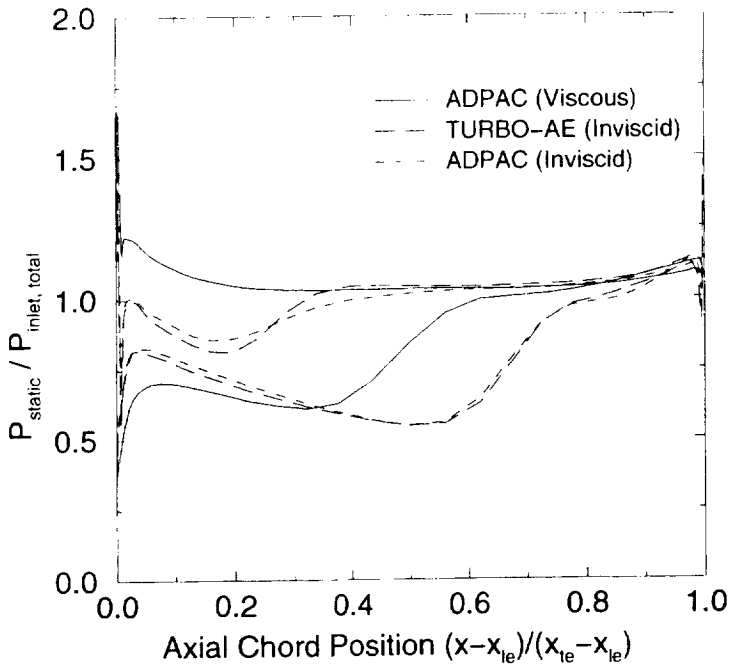

Figure 7.4: Comparison of steady blade surface pressure distributions for the 50% span location. Predictions obtained from a viscous *ADPAC*, inviscid *ADPAC*, and inviscid *TURBO-AE* calculations performed at the flutter point.

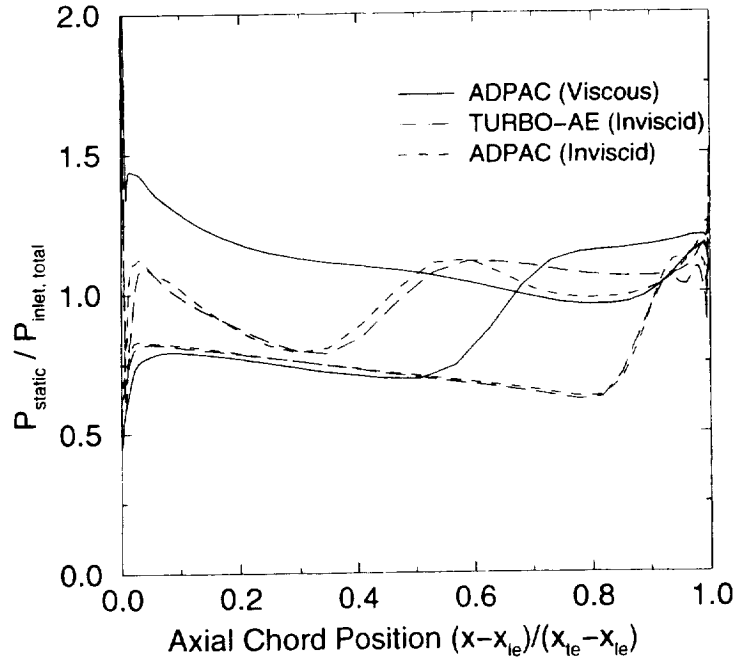

Figure 7.5: Comparison of steady blade surface pressure distributions for the 75% span location. Predictions obtained from a viscous *ADPAC*, inviscid *ADPAC*, and inviscid *TURBO-AE* calculations performed at the flutter point.

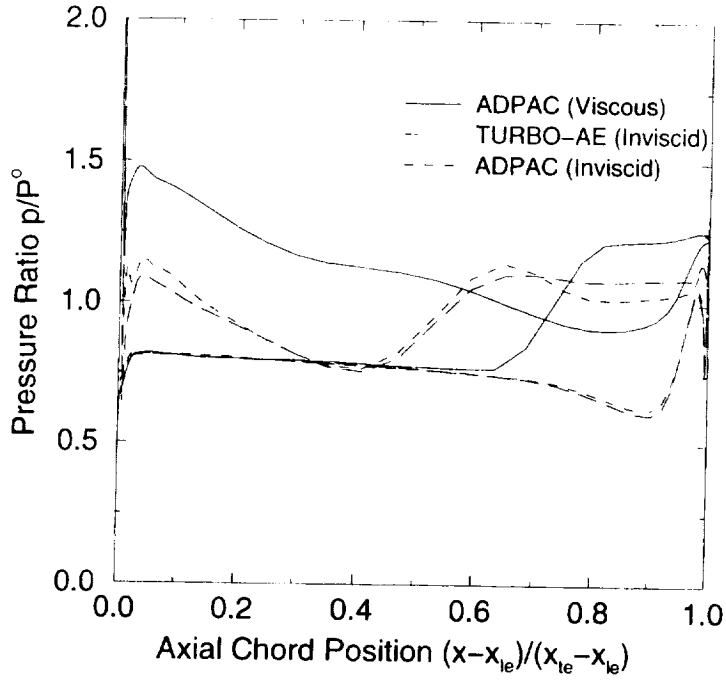

Figure 7.6: Comparison of steady blade surface pressure distributions for the 88% span location. Predictions obtained from a viscous *ADPAC*, inviscid *ADPAC*, and inviscid *TURBO-AE* calculations performed at the flutter point.

The inviscid assumption changes the nature of the shock structure on the blade. This is shown in Figures 7.7, 7.8, and 7.9, which compare the Mach number contours obtained from the viscous *ADPAC*and inviscid *TURBO-AE* solutions at the 50%, 75%, and 88% span locations, respectively. The comparison of the viscous to the inviscid Mach contours in Figure 7.7 shows that the inviscid *TURBO-AE* solution exhibits very little boundary layer-like behavior near the blade surface. This finding was of some importance since during the initial attempts at trying to start the inviscid *TURBO-AE* solution by using a uniform flow, there appeared to be boundary layer-like behavior near the blade surface. It was felt that this boundary layer behavior was preventing *TURBO-AE* from getting the pressure ratio and mass flow observed during rig testing. Using a better initial estimate of the flow as a starting point appears to have removed this type of behavior. The other point that should be observed from Figure 7.7 is that the character of the shock structure has changed for the two flow assumptions. The shock structure obtained from the viscous solution appears to be a weak bow shock. However, the shock observed in the inviscid flow is stronger indicating that the relative Mach number approaching the blade row is higher for the inviscid flow. This is consistent with the lower blockage associated with the inviscid flow. The increased strength of the bow shock associated with the inviscid flow generates a reflected shock, which intersects the pressure surface of the neighboring blade. The reflected shock is responsible for the observed differences in the magnitude of the steady pressure on the pressure side of the blade, as shown in Figure 7.4. Similar observations can be made with respect to the Mach contours shown in Figures 7.8 and 7.9.

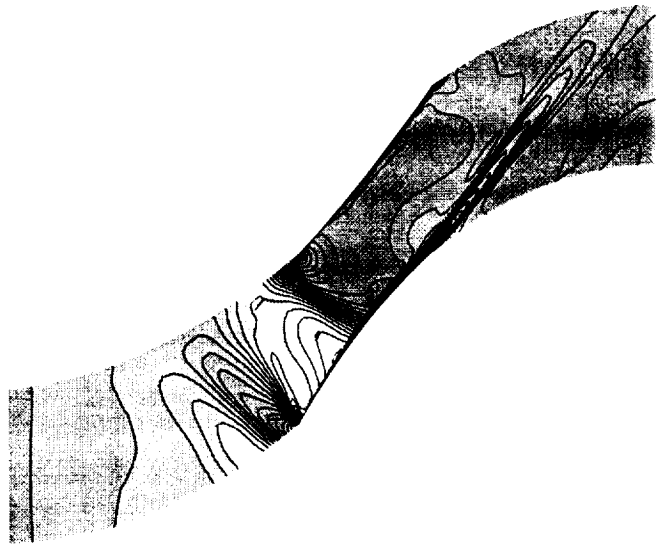

(a) Viscous

(b) Inviscid

Figure 7.7: Comparison of steady Mach number contours for the 50% span location. Predictions obtained from a viscous *ADPAC* and inviscid *TURBO-AE* calculations performed at the flutter point.

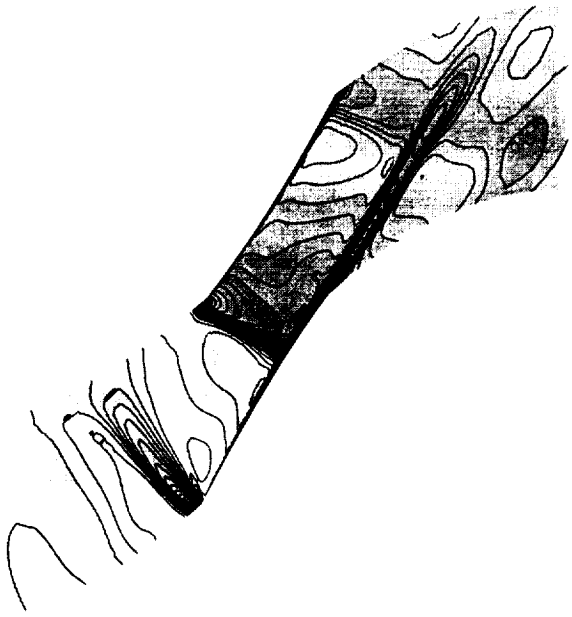

(a) Viscous

(b) Inviscid

Figure 7.8: Comparison of steady Mach number contours for the 75% span location. Predictions obtained from a viscous *ADPAC*and inviscid *TURBO-AE* calculations performed at the flutter point.

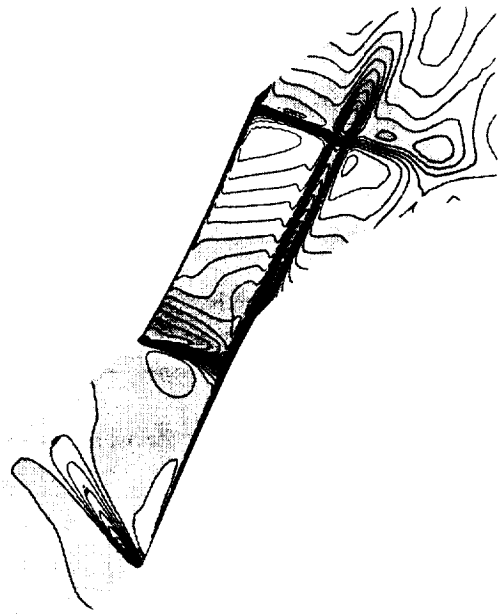

(a) Viscous

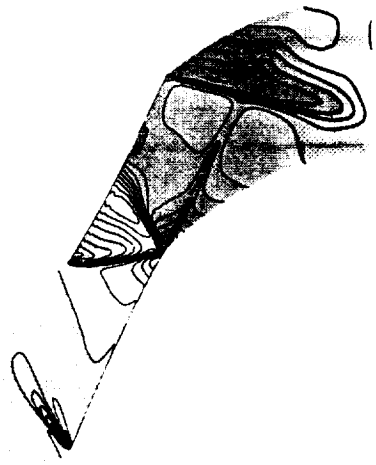

(b) Inviscid

Figure 7.9: Comparison of steady Mach number contours for the 88% span location. Predictions obtained from a viscous *ADPAC*and inviscid *TURBO-AE* calculations performed at the flutter point.

7.2 Unsteady Flow: Flutter Point

To calculate the amount of unsteady aerodynamic damping associated with a prescribed blade motion the *TURBO-AE* and *SLiQ*algorithms were used. The flutter behavior for the prescribed motion was then assessed by looking at the sign of the aerodynamic damping term. A positive value indicated that the mode was stable while a negative sign indicates flutter.

The *TURBO-AE* unsteady calculations were performed assuming that the flow was inviscid. The mesh was the same one that was used for the steady calculations, see Figure 7.1. The blade motion was prescribed by interpolating the required mode shape onto the blade surface of the mesh used in the unsteady aerodynamic calculation. In this study the blade was vibrated in its first torsion mode, which has a frequency of 563 Hz. The mode shape and frequency information were obtained from a finite element analysis using the in-house program, *STRATA*. The blade was modeled using meanline shell elements. The disk was assumed to be rigid and thus did not enter into the frequency or modeshape determination. Phase lagged boundary conditions were prescribed along the periodic boundaries of the computational domain. Characteristic boundary conditions were prescribed at the inlet and exit flow boundaries. No attempt was made to use the nonreflecting inlet and exit boundary conditions. Unsteady calculations were made for interblade phase angles of 0, 30, 60, and 90 degrees.

The *SLiQ*calculations were performed for a number of interblade phase angles between ∓ 180 degrees . Since the *SLiQ*calculation is linear, the required interblade phase angle boundary condition was applied directly to the periodic boundaries. The inlet and exit boundary condition is modeled using a quasi 3-D, nonreflecting approximation.

7.2.1 Unsteady Aerodynamic Work

The unsteady aerodynamic work, Ξ, performed by the air flow on a vibrating blade can be calculated for one cycle of blade oscillation using the methods outlined in reference [18]. Once Ξ has been calculated the unsteady aerodynamic damping parameter, δ_{aero}, can be calculated using Equation 6.1. The *TURBO-AE* algorithm was constructed to output Ξ after the completion of each iteration. During this investigation convergence of the unsteady calculation was determined by monitoring this parameter. The history of the unsteady aerodynamic work as a function of the number of oscillation cycles for interblade phase angles of 0, 30, 60, and 90 degrees is given in Figure 7.10. Referring to this figure, it will be noticed that a converged unsteady solution was only obtained for the 0 degrees interblade phase angle case. The remaining interblade phase angles studied exhibited an oscillatory behavior in the unsteady aerodynamic work. Because of the large amount of computer time required to perform these unsteady calculations it was necessary to stop the calculations after about 20 cycles. In these cases, the unsteady aerodynamic work was calculated by determining the mean value of the 4^{th} through last cycle. The first three oscillation cycles were excluded based on the results of the 0 degrees interblade phase angle analysis where the calculation required three cycles before the startup transients settled out.

A comparison of the unsteady aerodynamic work per cycle obtained from the

TURBO-AE , *ADPAC*(vis) + *SLiQ*, and *ADPAC*(inv) + *SLiQ*, analyses is shown in Figure 7.11. The values presented for the *TURBO-AE* analyses are the mean values discussed above. Also shown with the *TURBO-AE* values are bars giving the maximum and minimum values of Ξ obtained from the 4^{th} through last cycle. Three sets of results are associated with the viscous *ADPAC*+ *SLiQ*predictions, one each corresponding to the flutter, non-flutter, and the point with the highest mass flow rate on the speed line (point 4), see Figure 7.3. These three points show that as mass flow is increased the blade vibration tends to becomes more stable. The least stable condition is associated with the flutter point for interblade phase angles between 0 and 50 degrees. However, the inviscid *ADPAC*+ *SLiQ*results for the flutter point indicate that the blade is stable for all interblade phase angles. This change in flutter behavior is related to the change in shock structure on the blade. The mean values of the *TURBO-AE* results are consistent with the viscous *ADPAC*+ *SLiQ*results in that the blade becomes unstable over a range of interblade phase angles. Comparing the viscous *ADPAC*+ *SLiQ*results to those obtained from *TURBO-AE* , it will be noticed that while both predict unstable behavior the *TURBO-AE* predictions indicate that the blade has a higher value of unsteady aerodynamic work over a wider range of interblade phase angles. This implies that when the blade's inherent mechanical damping is taken into account, the *TURBO-AE* predicted aerodynamic damping, Using Equation 6.1, is more likely to overcome this value resulting in a flutter situation.

The differences observed between the *TURBO-AE* , viscous *ADPAC*+ *SLiQ*, and inviscid *ADPAC*+ *SLiQ*results demonstrate the sensitivity of these predictions to the analysis method chosen. As the rig blade did exhibit flutter behavior, the *TURBO-AE* and viscous *ADPAC*results are encouraging. However the discrepancy between the *TURBO-AE* and inviscid *ADPAC*+ *SLiQ*results should be further investigated since both methods use an inviscid assumption and therefore would be expected to give similar results. At the very least, an viscous *TURBO-AE* analysis should be performed with a version of the code using an improved viscous flow model. This improved viscous model was incorporated into the latest version of the *TURBO*code. However, this version was not used in this study since it was not available until late in the program and it was not feasible to change versions and still complete our objectives before the program ended.

7.2.2 Time Mean Behavior

The *TURBO-AE* algorithm models the nonlinear unsteady response of a vibrating blade row. In order to compare the unsteady blade surface pressures predicted from *TURBO-AE* to those obtained from *SLiQ*the unsteady pressure must first be decomposed into its harmonic components. This section presents a comparison of the time mean, or 0^{th} harmonic, of the unsteady pressure obtained from *TURBO-AE* as a result of blade vibration to the steady blade surface pressure obtained when the blade was not vibrating. The next section will present the 1^{st} harmonic comparisons.

The time mean component of the unsteady blade surface pressure obtained from *TURBO-AE* is shown in Figures 7.12, 7.13, and 7.14. These figures present the time mean blade surface pressure for interblade phase angles of 0, 30, and 60 degrees for the 50%, 75%, and 88% span locations, respectively. The unsteady response in this case is obtained as a result of blade vibration in the first torsion mode. Also shown in these figures is the

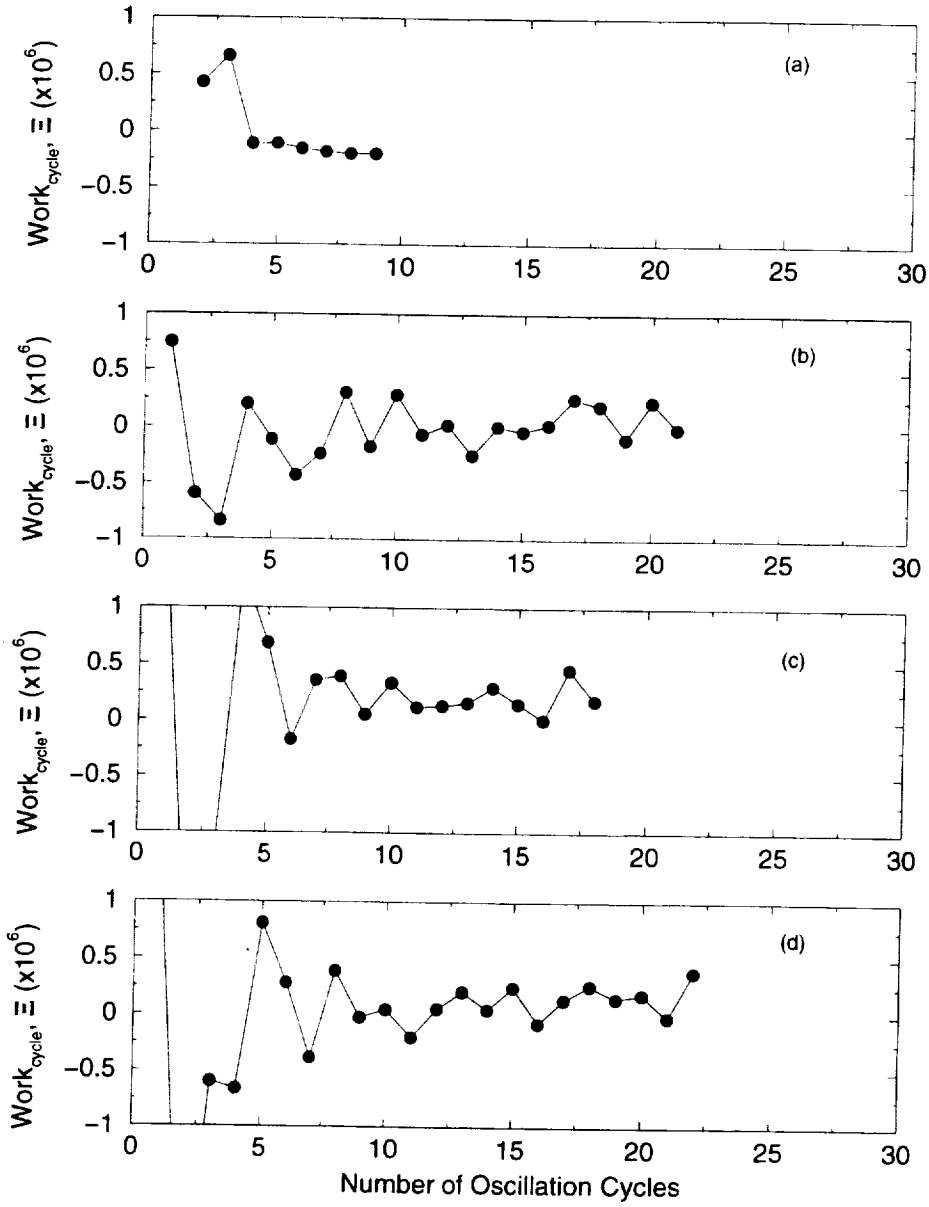

Figure 7.10: *TURBO-AE* predicted unsteady aerodynamic work-per-cycle as a function of the number of oscillation cycles, (a) 0, (b) 30, (c) 60, and (d) 90 degrees interblade phase angle.

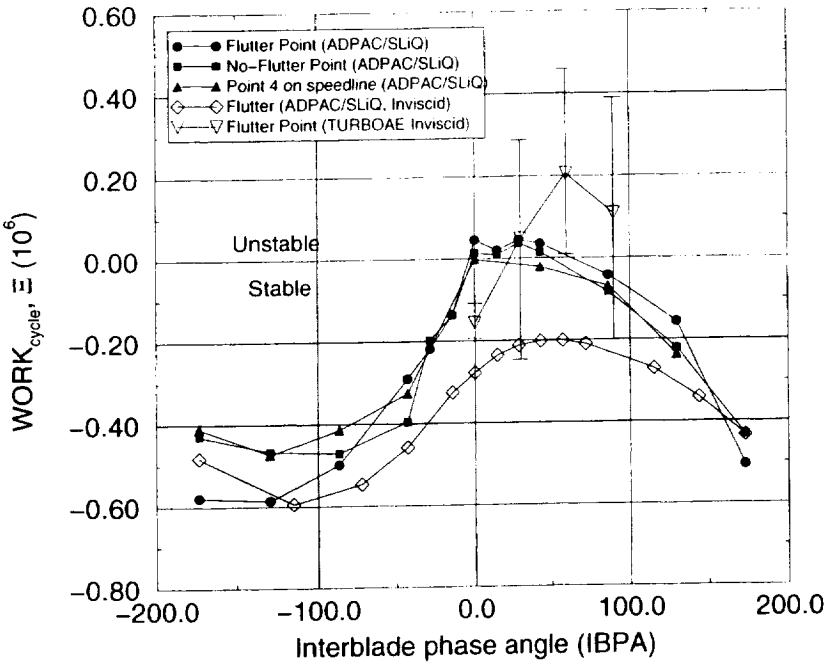

Figure 7.11: Comparison of the unsteady aerodynamic work-per-cycle as a function of interblade phase angle. Predictions made using viscous *ADPAC/SLiQ*, inviscid *ADPAC/SLiQ*, and *TURBO-AE* algorithms.

steady blade surface pressure obtained when the blade was not vibrating. These steady pressures are the same as were shown in Figures 7.4 through 7.6. In Figure 7.12, it is seen that the time mean component and the steady pressure do not agree over portions of both the suction and pressure surfaces. Two sets of curves are shown for the 30, 60, and 90 degrees interblade phase angles. One curve corresponds to a point near the minimum unsteady work per cycle, Ξ, and the other to a point near the maximum value shown in Figure 7.10. The 0 degree interblade phase angle curve shown in Figure 7.10 did not exhibit much change as a function of oscillation cycle and therefore only one curve is shown. The largest difference between the steady and time mean pressures occurs on the pressure side of the blade before and after the intersection of the reflected shock with the blade surface. This result is independent of the interblade phase angle being analyzed. The difference between the time mean and steady response appears to be the result of blade vibration. Similar behavior can be observed in Figures 7.13, and 7.14. If the unsteady response were truly linear, there should be no difference between the time mean and the steady pressure components. This difference may be the result of nonlinear behavior and will be investigated further in the next section.

7.2.3 Unsteady Harmonic Response

The unsteady blade surface pressure obtained from *TURBO-AE* was decomposed into the first and second harmonics of the blade vibration frequency, 564 Hz. The magnitude and phase for the 1^{st} harmonic of the unsteady pressure resulting from a 0 degree interblade

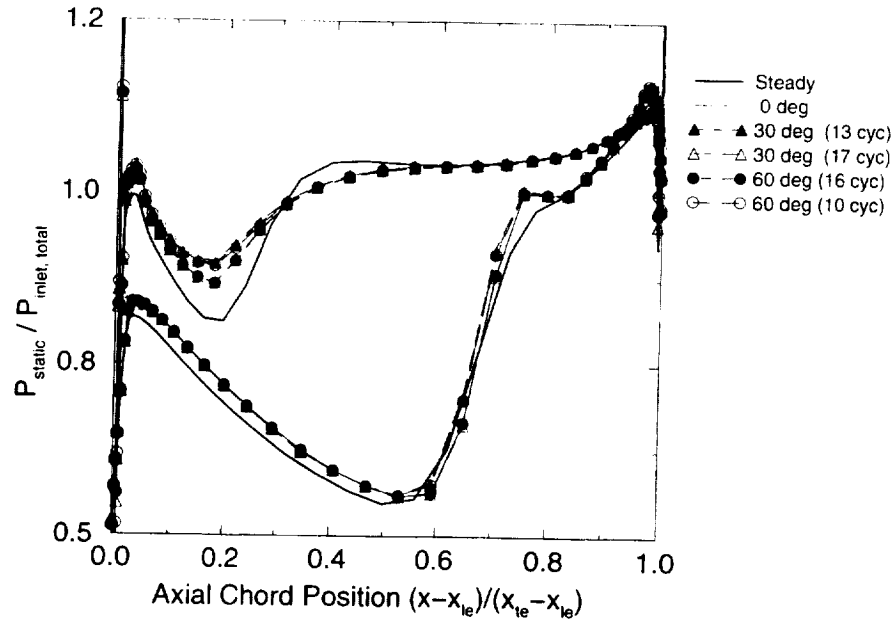

Figure 7.12: Comparison of the time mean and steady blade surface pressure distributions obtained from *TURBO-AE* at the 50% span location.

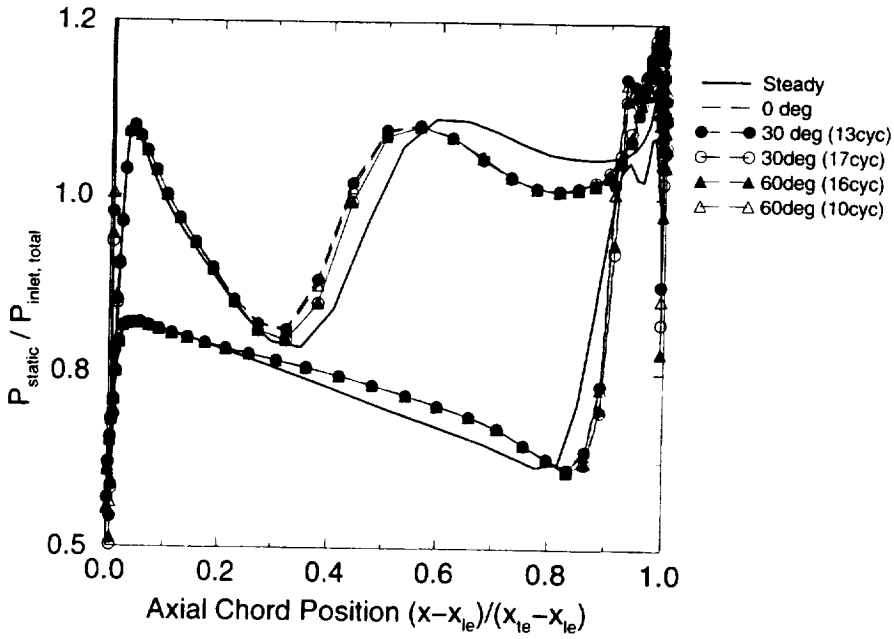

Figure 7.13: Comparison of the time mean and steady blade surface pressure distributions obtained from *TURBO-AE* at the 75% span location.

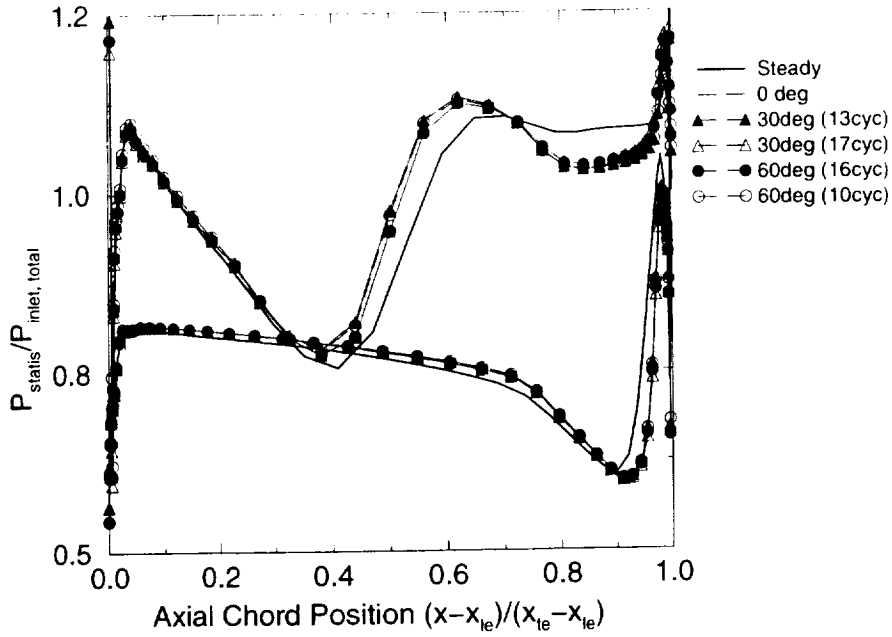

Figure 7.14: Comparison of the time mean and steady blade surface pressure distributions obtained from *TURBO-AE* at the 88% span location.

phase angle motion are shown in Figures 7.15 through 7.17. These figures present the results for the 50%, 75%, and 88% span locations. Predictions from inviscid *TURBO-AE* , viscous *ADPAC/ SLiQ*, and inviscid *ADPAC/ SLiQ*analyses are compared in these figures. As shown in Figure 7.15, the magnitude of the inviscid *TURBO-AE* predicted unsteady pressure is larger in the leading edge region of the pressure surface and the trailing edge region of the suction surface than either of the predictions obtained from the *ADPAC/ SLiQ*algorithms. This trend is similar for the 75% and 88% span locations, Figures 7.16, and 7.17, respectively. The regions over which this discrepancy occurs correspond to the intersection of the leading edge bow shock with the suction surface and the resulting reflected shock with the pressure surface.

The unsteady phase information presented in Figures 7.15, 7.16, and 7.17 indicate that at the 50% span location all three algorithms predict different phase behavior on both the suction and pressure surfaces. At the 75% and 88% span locations the viscous and inviscid *ADPAC/ SLiQ*phase predictions agree well on the suction surface, but they differ greatly from the *TURBO-AE* predicted phase distribution. The pressure surface phase predictions obtained from *ADPAC/ SLiQ*are not in as good agreement as was observed on the suction surface, but they are in better agreement with each other than with the *TURBO-AE* predicted phase distribution.

The 0 degree interblade phase angle results indicate that there is a large difference between the inviscid *TURBO-AE* and the viscous and inviscid *ADPAC/ SLiQ*predictions of unsteady magnitude and phase. The overall stability of the blade, as shown in Figure 7.11, however is not that much different for this interblade phase angle. A better approach for comparing the three predictions would be to use the work distribution on the

blade surface, see reference [18]. However, this parameter was not available from the *SLiQ*program in a manner that would allow direct comparison with the *TURBO-AE* predictions. Therefore, the comparison was not made during this study.

Comparisons of the magnitude and phase of the 1^{st} harmonic of the unsteady blade surface pressure for the 30, and 60 degree interblade phase angles are presented in Figures 7.18 through 7.23. As was observed for the 0 degree interblade phase angle case, the magnitude of the unsteady pressure predicted using the inviscid *TURBO-AE* approach differs from both the viscous *ADPAC/ SLiQ*and inviscid *ADPAC/ SLiQ*predictions in the vicinity of the shock intersections on the suction and pressure surfaces. The largest difference appears to occur at the 50% span location. The behavior of the unsteady pressure magnitude in the vicinity of the blade trailing edge is quite different than was observed for the 0 degree interblade phase angle. At the 50%, 75%, and 88% span locations a large discrepancy between the three sets of predictions occurs near the trailing edge. The inviscid *TURBO-AE* calculations show a much larger unsteady pressure magnitude at the trailing edge than does either of the *ADPAC/ SLiQ*predictions. This may be the result of the shock impingement and/or the rounded trailing edge geometry used for the *TURBO-AE* predictions. The viscous and inviscid *ADPAC*steady predictions, Figures 7.4, 7.5, and 7.6, do not show as high a gradient as do the *TURBO-AE* predictions at the trailing edge. This may explain why the *SLiQ*and *TURBO-AE* predictions are not in agreement in this region.

The unsteady phase comparisons for the 30, and 60 degree interblade phase angles are similar to those observed for the 0 degree case. At the 50% span location there is poor agreement among the three sets of predictions. While at the 75% and 88% span locations the two sets of *ADPAC/ SLiQ*predictions are in good agreement with each other but not with the *TURBO-AE* predictions. The largest difference between the two *ADPAC/ SLiQ*predictions occurs in the vicinity of the shock intersections on the pressure surface.

In order to investigate the possibility of nonlinear effects being responsible for the differences observed in the time mean and steady response, the second harmonic of the unsteady pressure response was examined. The resulting plots of magnitude and phase for the 50%, 75% and 88% span locations are shown in Figures 7.24 through 7.26. These unsteady response predictions were obtained for an interblade phase angle of 0 degrees. The magnitude of second harmonic response of the unsteady pressure for all three span locations is much smaller than that of the first, indicating no nonlinear interaction between the higher harmonics of the vibration frequency. It is possible that the differences observed could be the result of the unsteady boundary conditions changing the flow slightly and thus changing the position of the shocks. It should be noted that the observed differences in the steady and time mean loading are small.

7.3 Conclusions

The *TURBO-AE* algorithm was applied to the flutter analysis of the first-stage fan of the TF41-A100 rig. In addition, viscous and inviscid *ADPAC*steady flows were used together with the *SLiQ*algorithm to predict flutter behavior. Comparison of the steady inviscid blade surface predictions from *TURBO-AE* and *ADPAC*showed that they agreed quite well with each other. However, the inviscid blade loading did not agree with the viscous

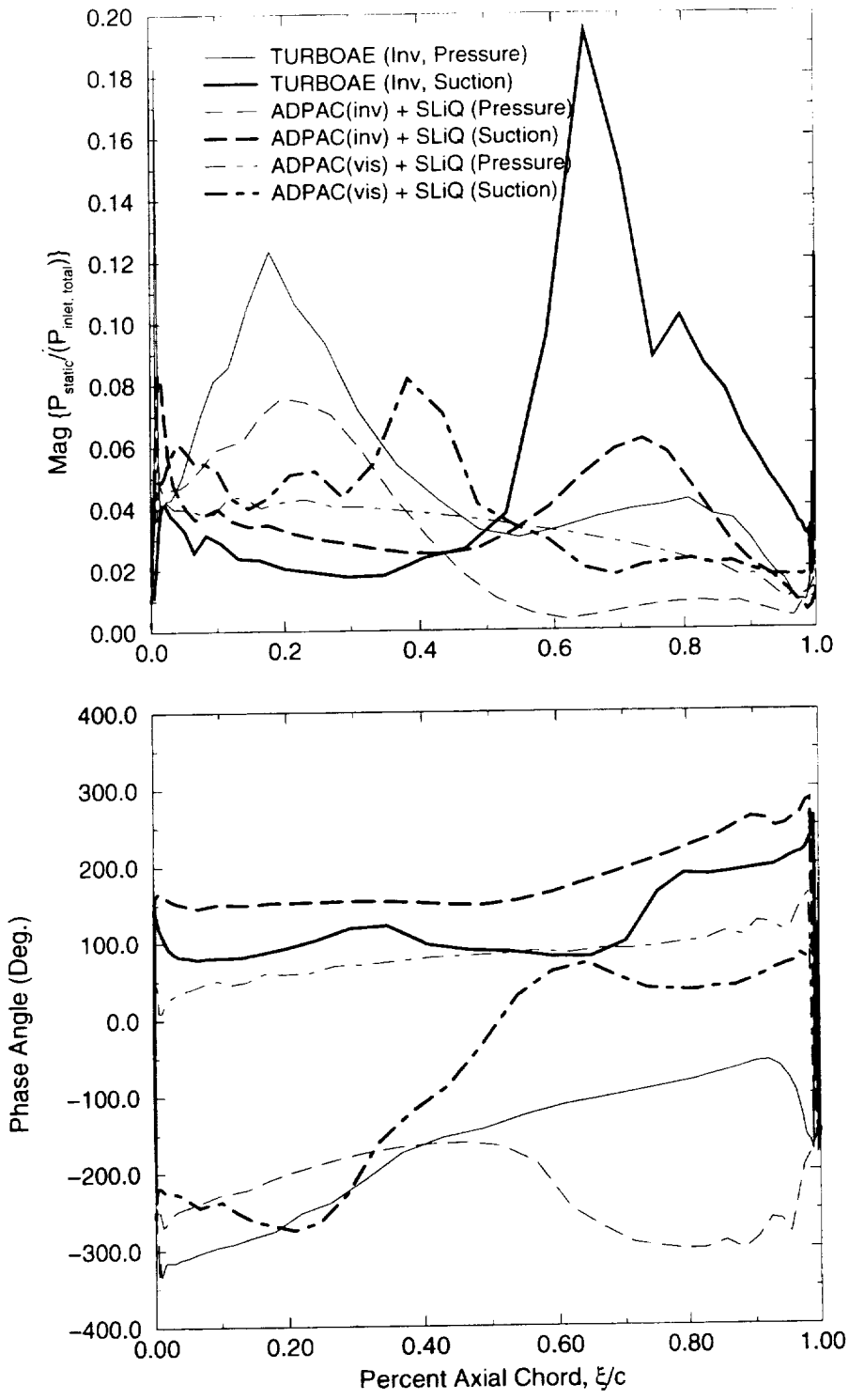

Figure 7.15: Comparison of the 1^{st} harmonic unsteady blade surface pressure distributions obtained from inviscid *TURBO-AE* , viscous *ADPAC/ SLiQ*, and inviscid *ADPAC/ SLiQ*calculations at the 50% span location, *upper* magnitude, and *lower* phase at an interblade phase angle of 0 degrees.

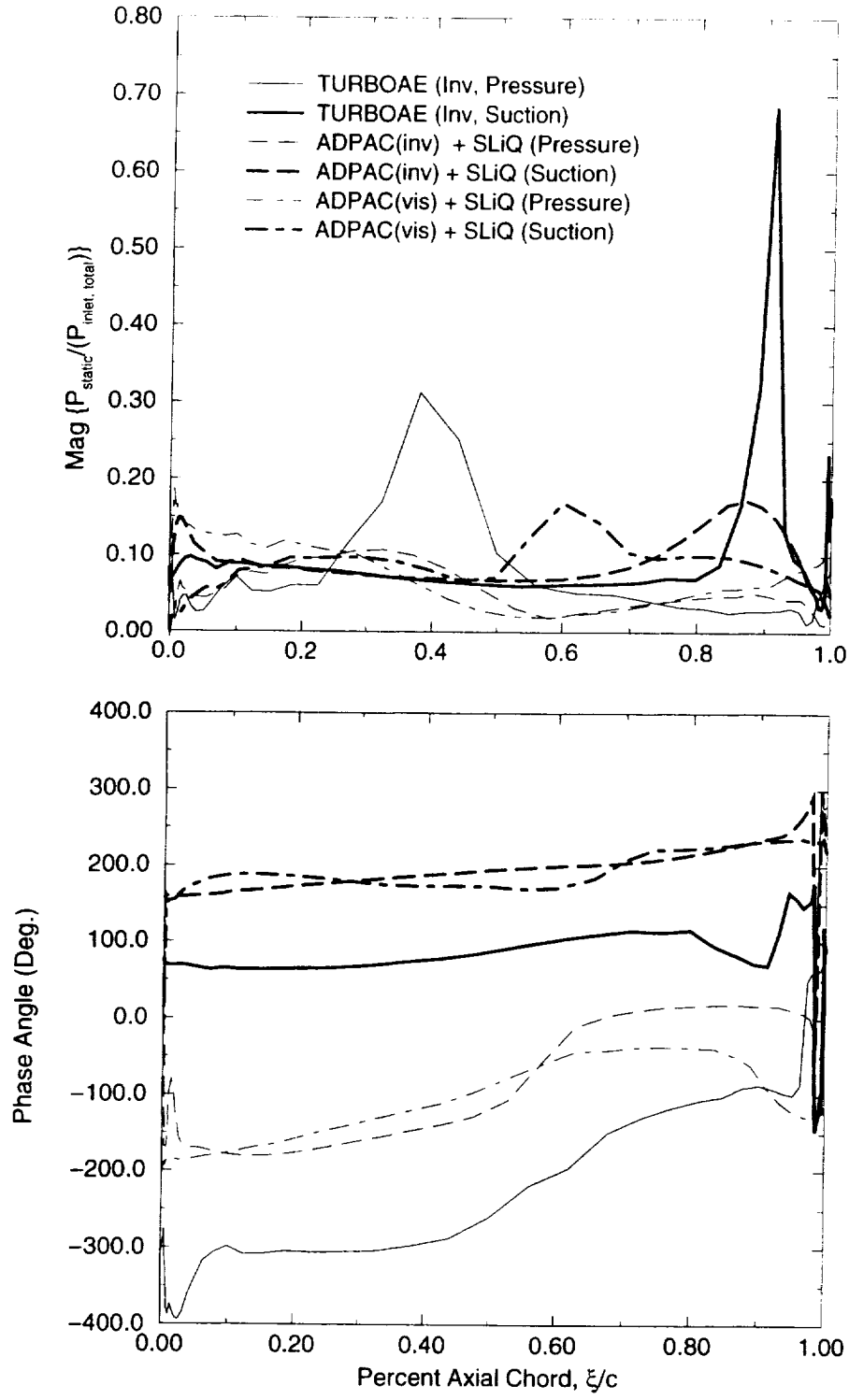

Figure 7.16: Comparison of the 1^{st} harmonic unsteady blade surface pressure distributions obtained from inviscid *TURBO-AE* , viscous *ADPAC/ SLiQ*, and inviscid *ADPAC/ SLiQ*calculations at the 75% span location, *upper* magnitude, and *lower* phase at an interblade phase angle of 0 degrees.

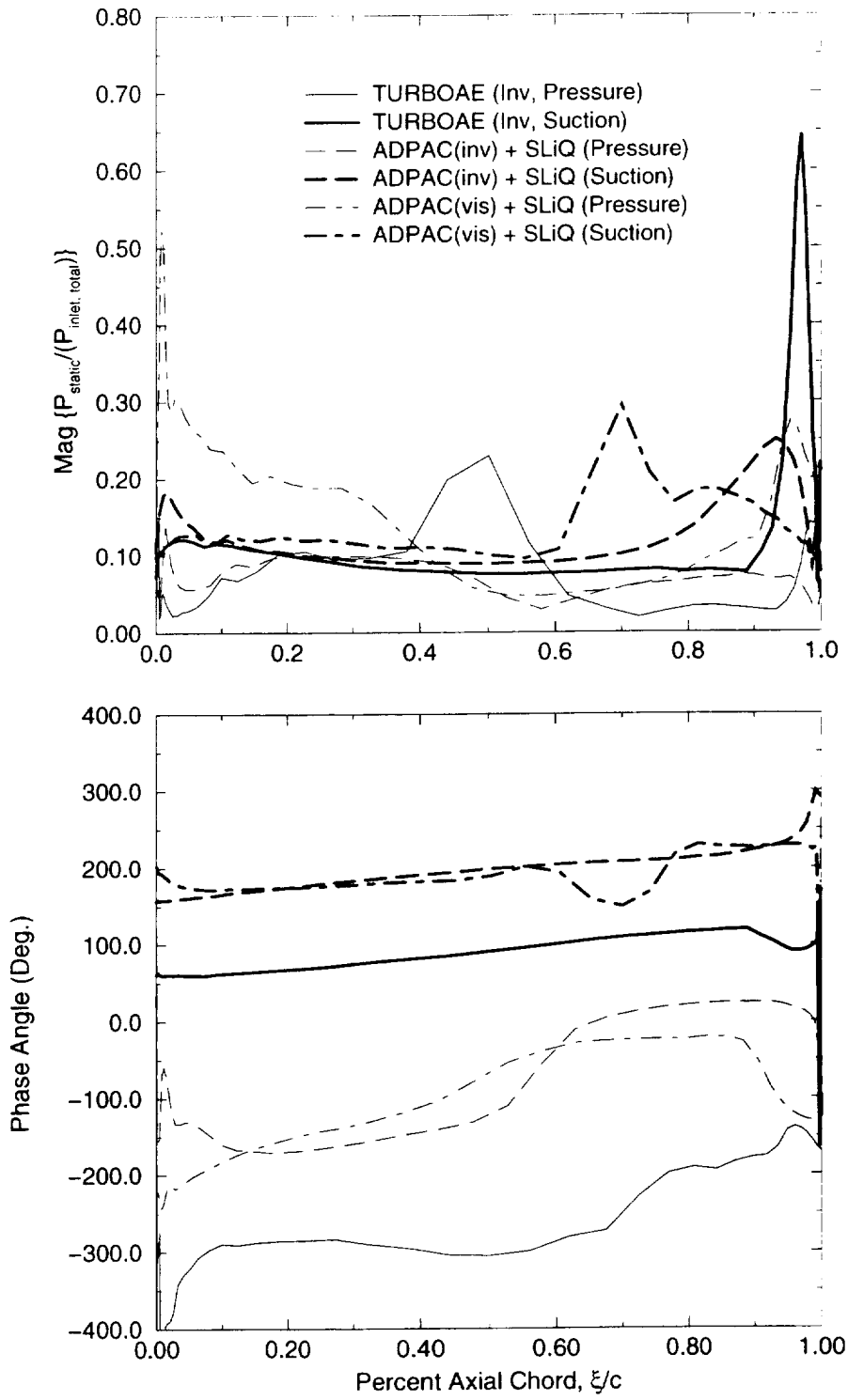

Figure 7.17: Comparison of the 1^{st} harmonic unsteady blade surface pressure distributions obtained from inviscid *TURBO-AE* , viscous *ADPAC/ SLiQ*, and inviscid *ADPAC/ SLiQ*calculations at the 88% span location, *upper* magnitude, and *lower* phase at an interblade phase angle of 0 degrees.

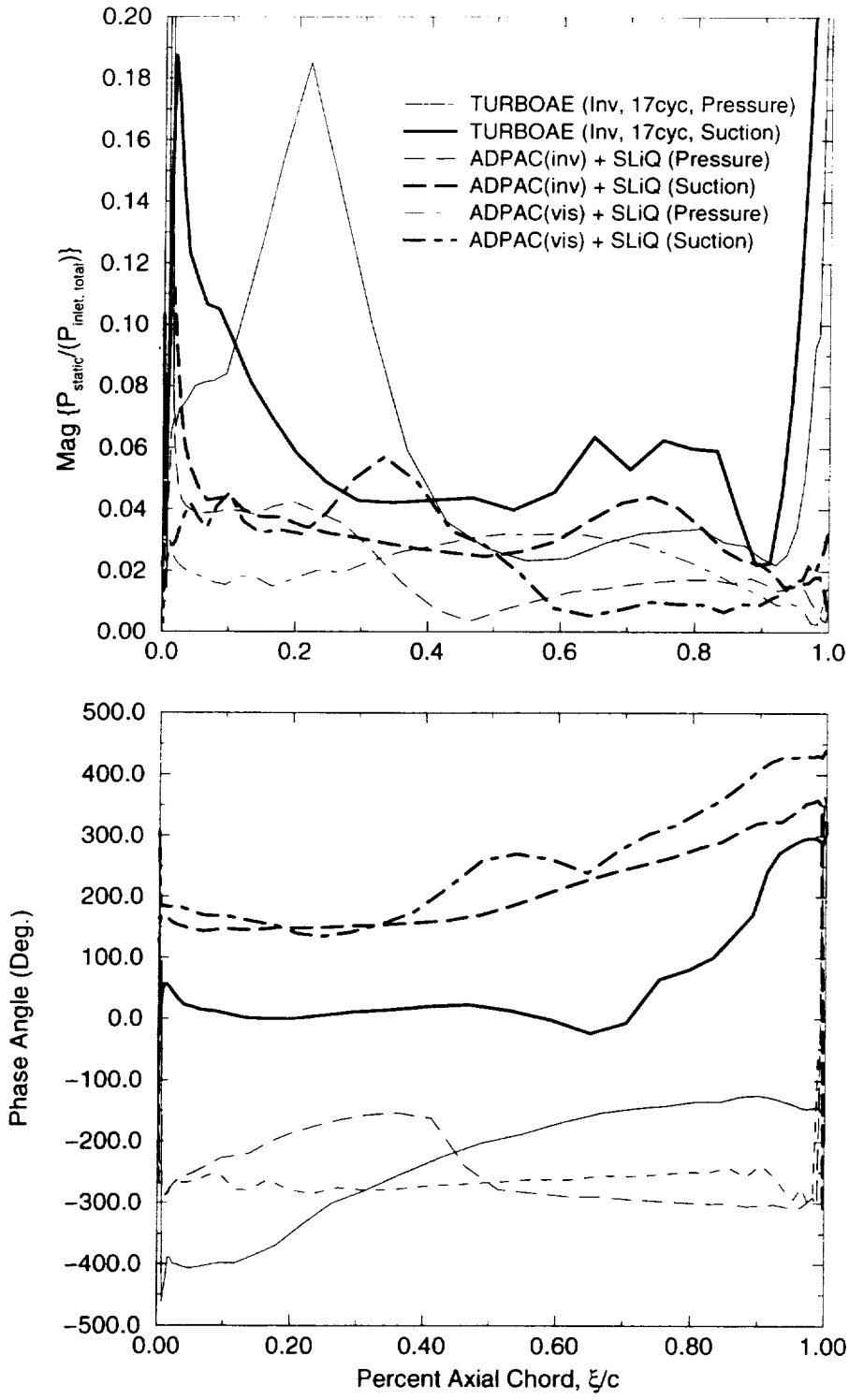

Figure 7.18: Comparison of the 1^{st} harmonic unsteady blade surface pressure distributions obtained from inviscid *TURBO-AE* , viscous *ADPAC/ SLiQ*, and inviscid *ADPAC/ SLiQ*calculations at the 50% span location, *upper* magnitude, and *lower* phase, at an interblade phase angle of 30 degrees.

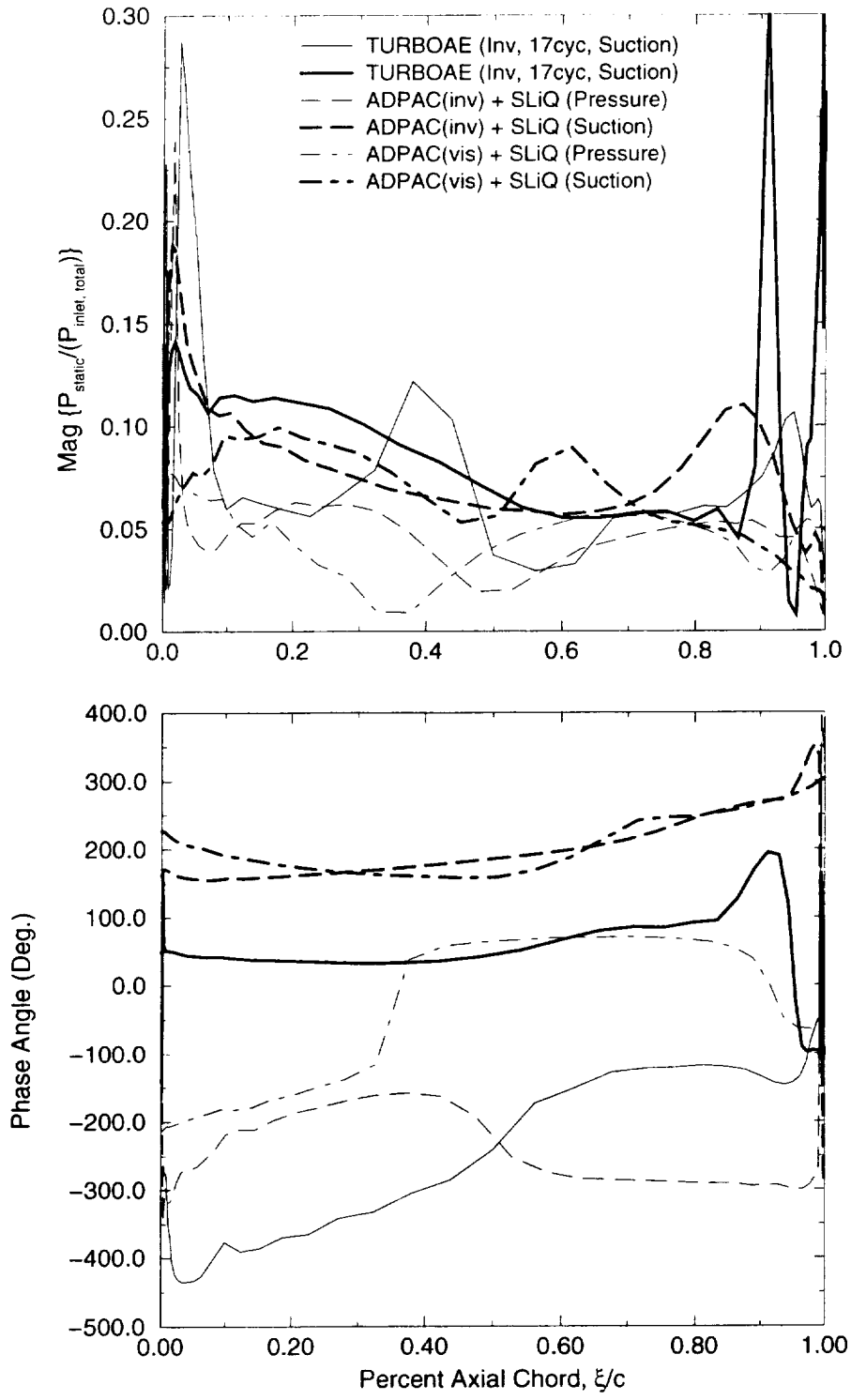

Figure 7.19: Comparison of the 1^{st} harmonic unsteady blade surface pressure distributions obtained from inviscid *TURBO-AE* , viscous *ADPAC/ SLiQ*, and inviscid *ADPAC/ SLiQ*calculations at the 75% span location, *upper* magnitude, and *lower* phase at an interblade phase angle of 30 degrees.

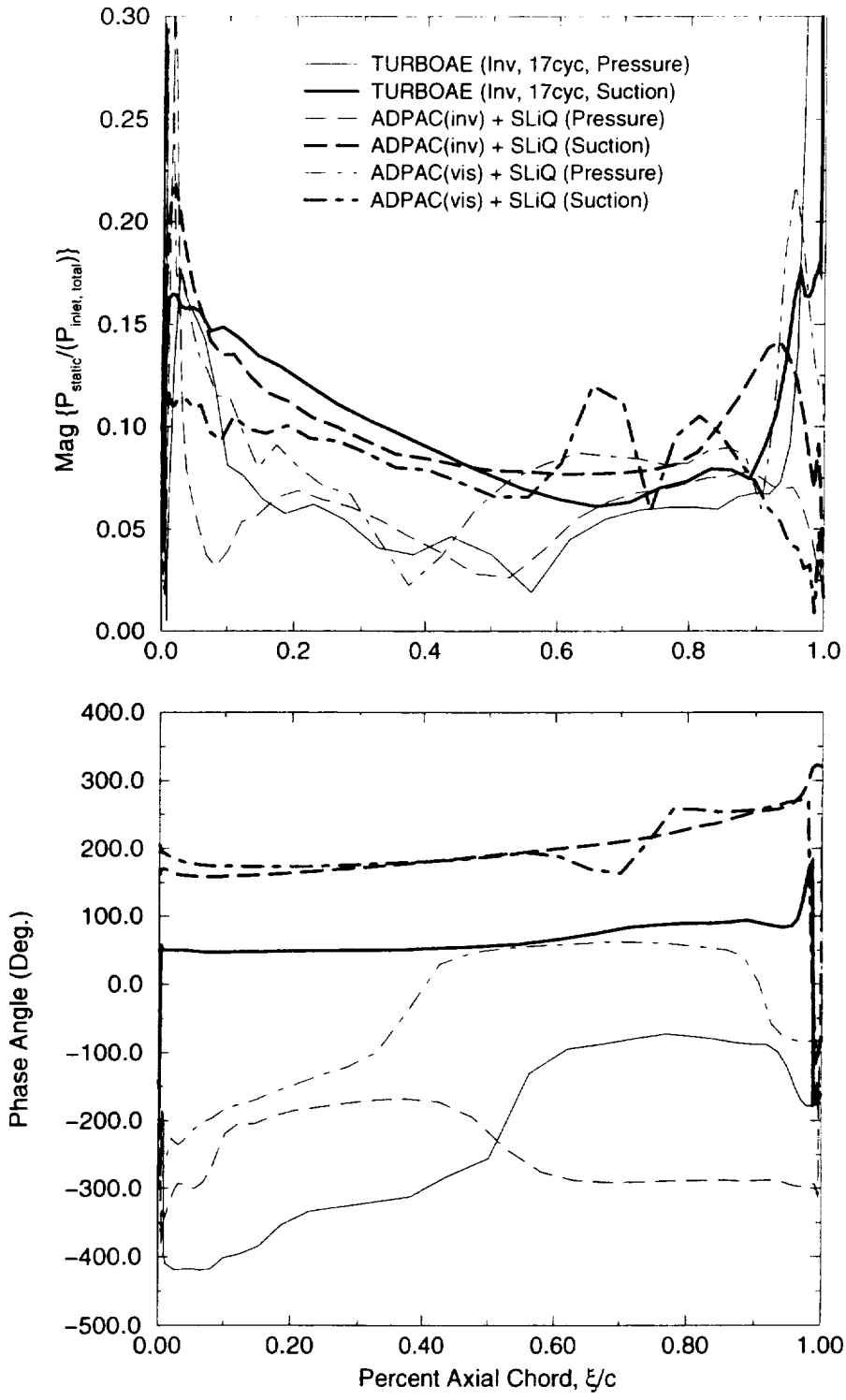

Figure 7.20: Comparison of the 1^{st} harmonic unsteady blade surface pressure distributions obtained from inviscid *TURBO-AE* , viscous *ADPAC/ SLiQ*, and inviscid *ADPAC/ SLiQ*calculations at the 88% span location, *upper* magnitude, and *lower* phase at an interblade phase angle of 30 degrees.

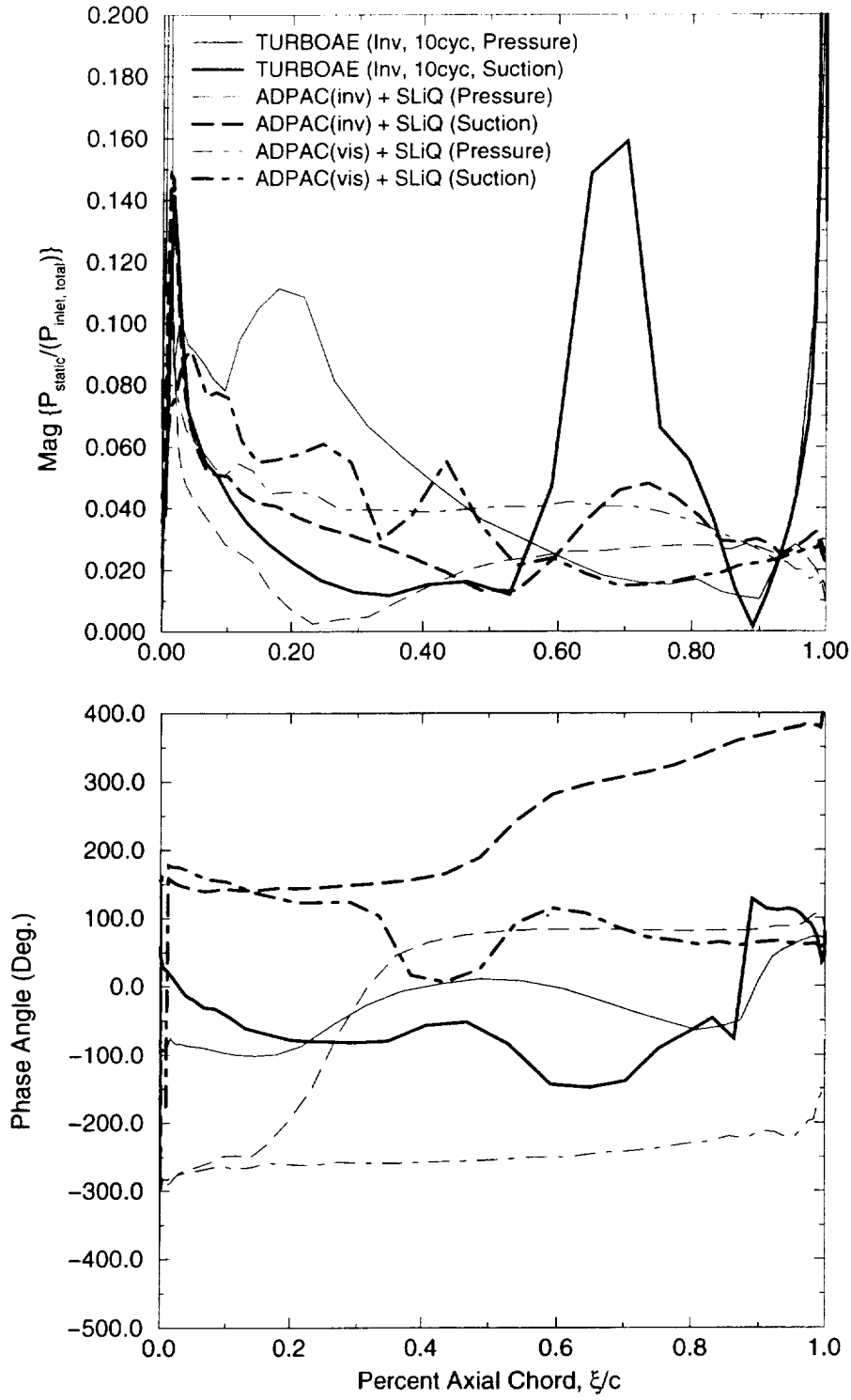

Figure 7.21: Comparison of the 1^{st} harmonic unsteady blade surface pressure distributions obtained from inviscid *TURBO-AE* , viscous *ADPAC/ SLiQ*, and inviscid *ADPAC/ SLiQ*calculations at the 50% span location, *upper* magnitude, and *lower* phase, at an interblade phase angle of 60 degrees.

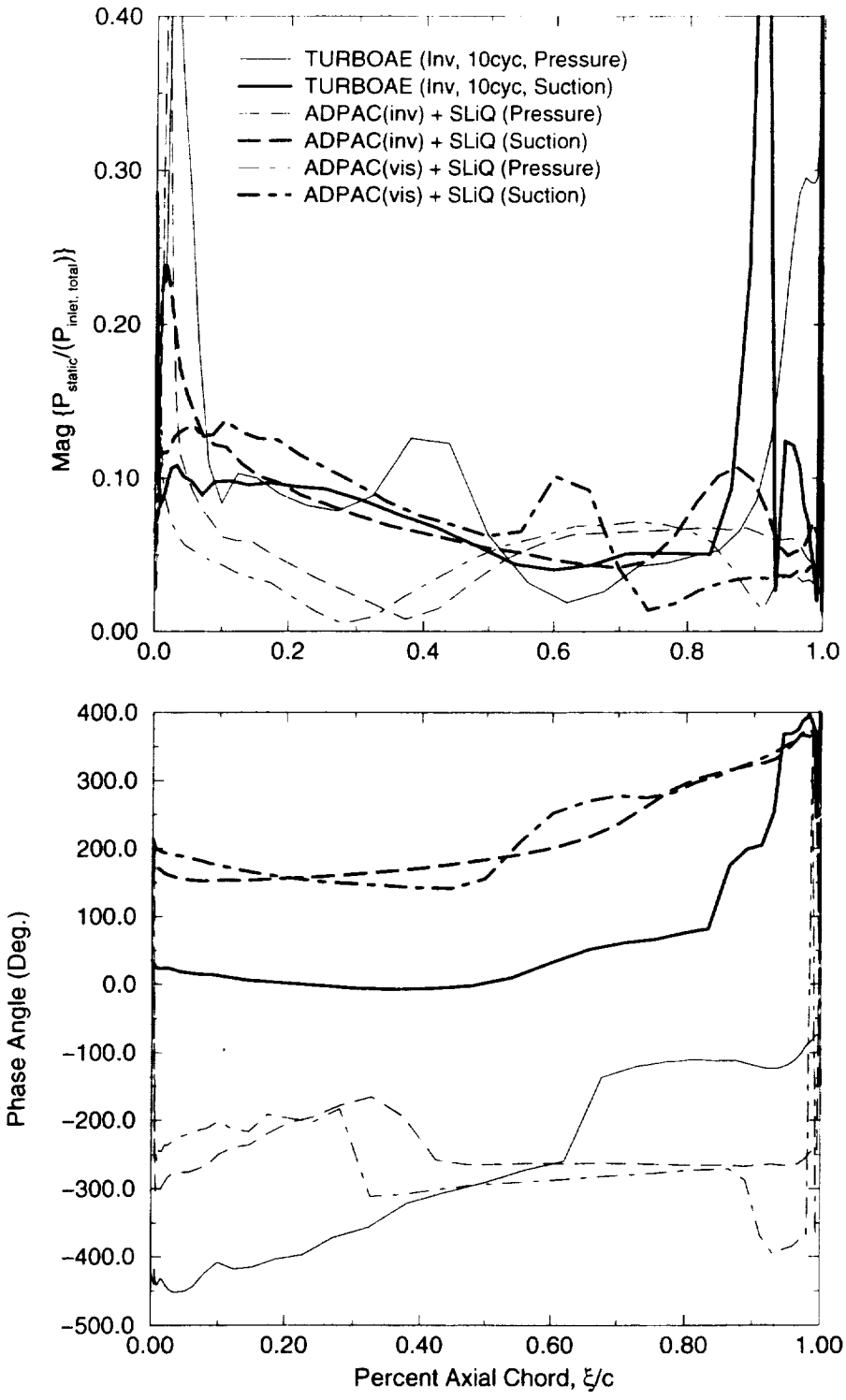

Figure 7.22: Comparison of the 1^{st} harmonic unsteady blade surface pressure distributions obtained from inviscid *TURBO-AE* , viscous *ADPAC/ SLiQ*, and inviscid *ADPAC/ SLiQ*calculations at the 75% span location, *upper* magnitude, and *lower* phase at an interblade phase angle of 60 degrees.

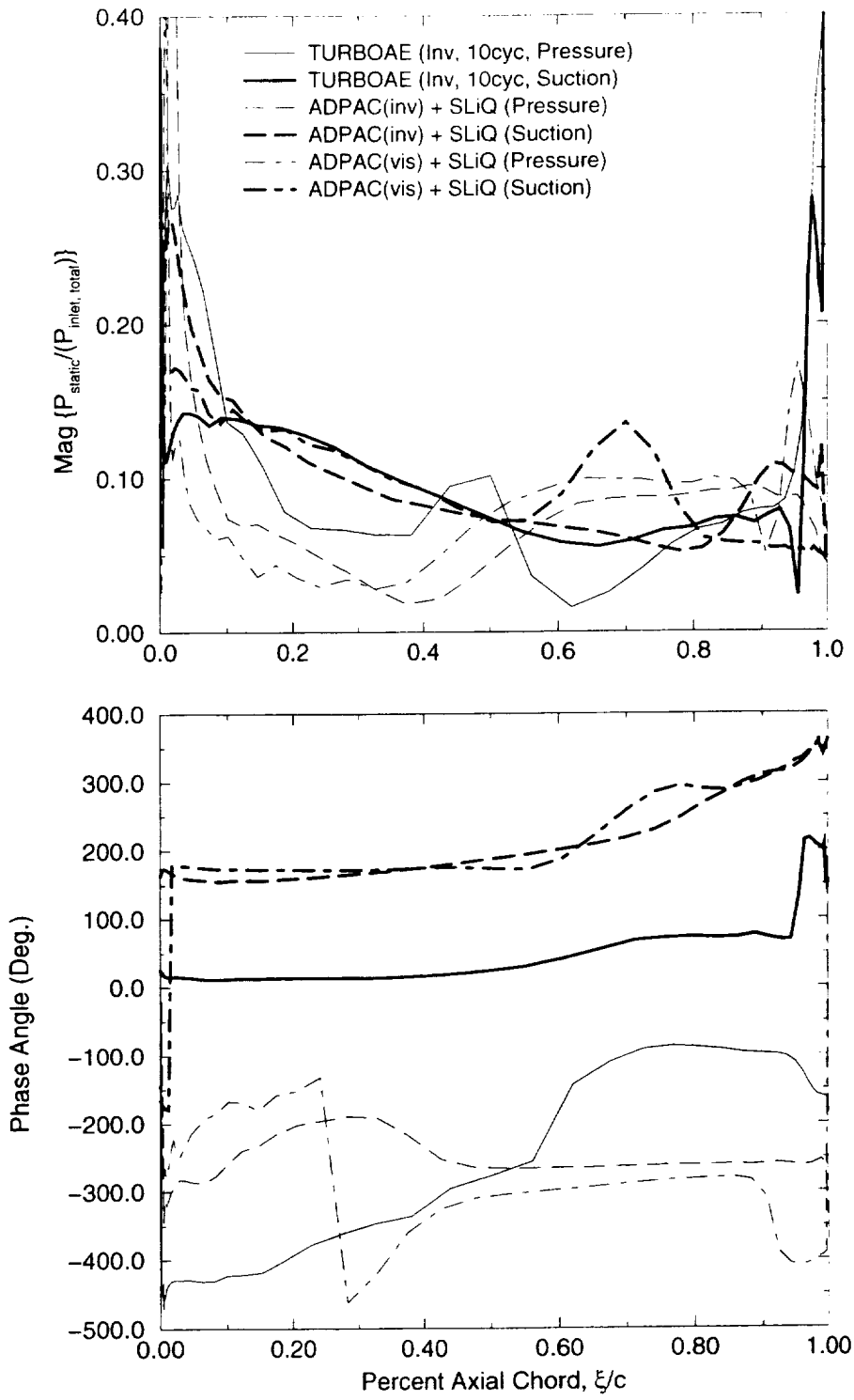

Figure 7.23: Comparison of the 1^{st} harmonic unsteady blade surface pressure distributions obtained from inviscid *TURBO-AE* , viscous *ADPAC/ SLiQ*, and inviscid *ADPAC/ SLiQ*calculations at the 88% span location, *upper* magnitude, and *lower* phase at an interblade phase angle of 60 degrees.

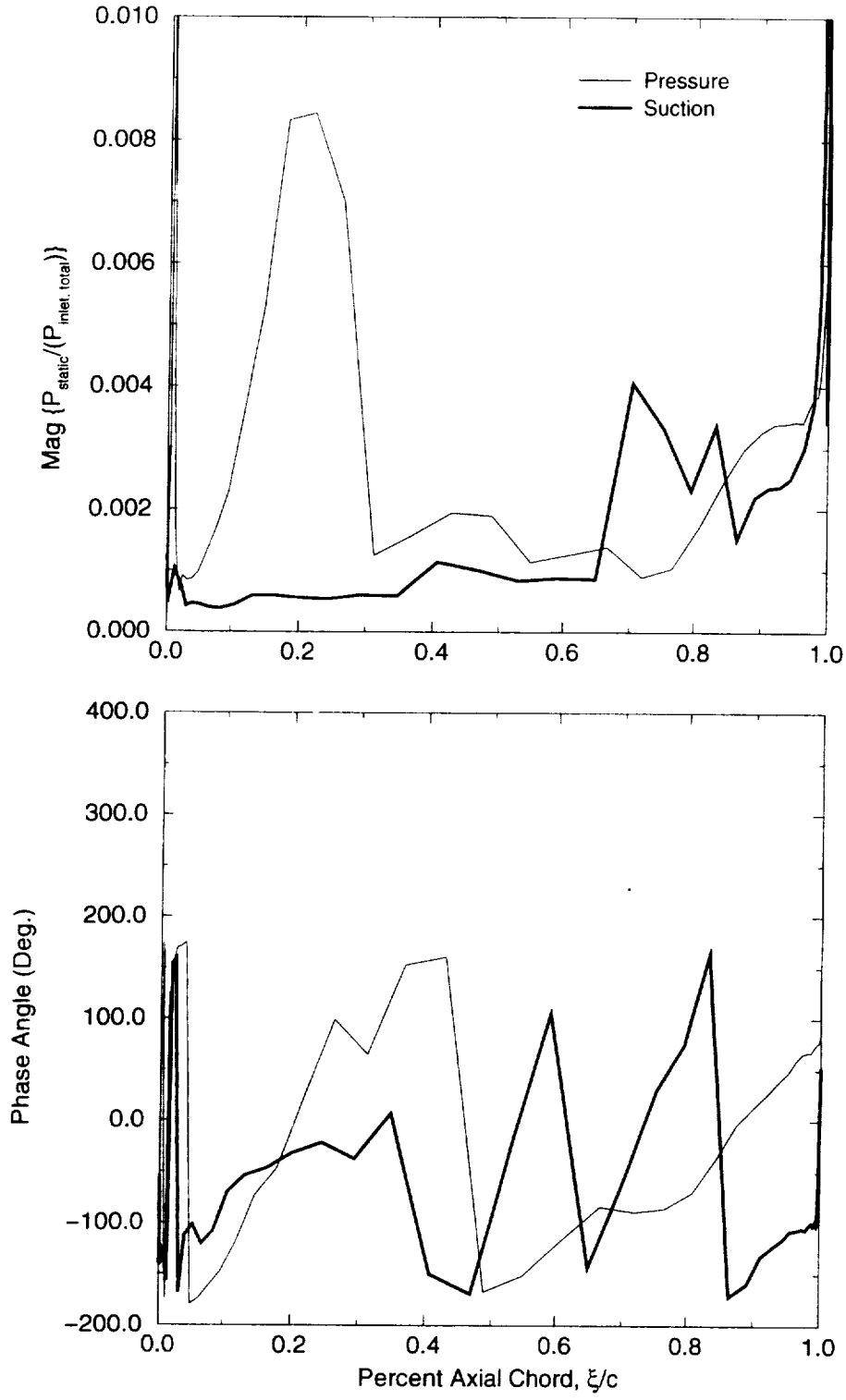

Figure 7.24: 2^{nd} harmonic unsteady blade surface pressure distributions obtained from inviscid *TURBO-AE* calculations at the 50% span location, *upper* magnitude, and *lower* phase at an interblade phase angle of 0 degrees.

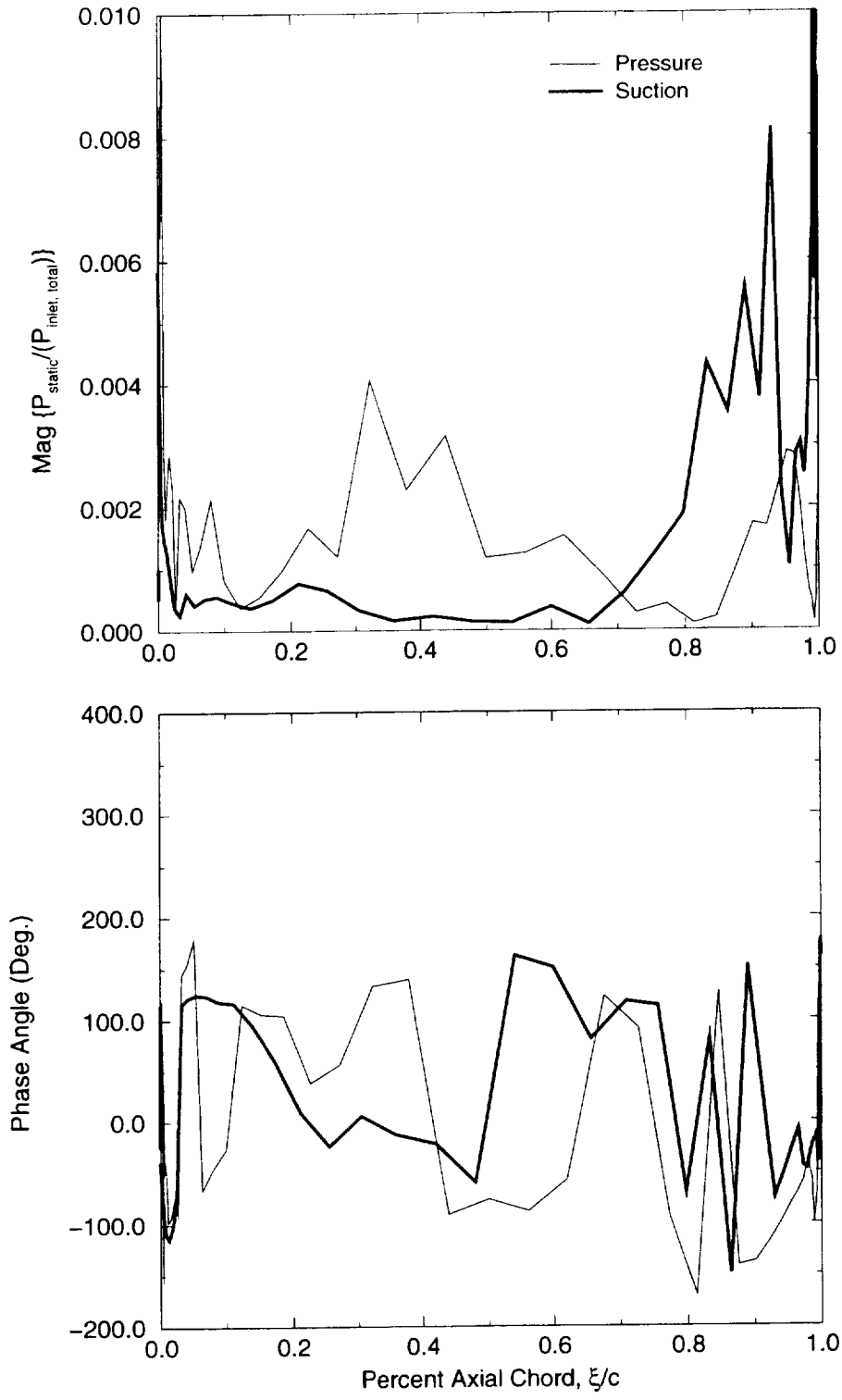

Figure 7.25: 2^{nd} harmonic unsteady blade surface pressure distributions obtained from inviscid *TURBO-AE* calculations at the 75% span location, *upper* magnitude, and *lower* phase at an interblade phase angle of 0 degrees.

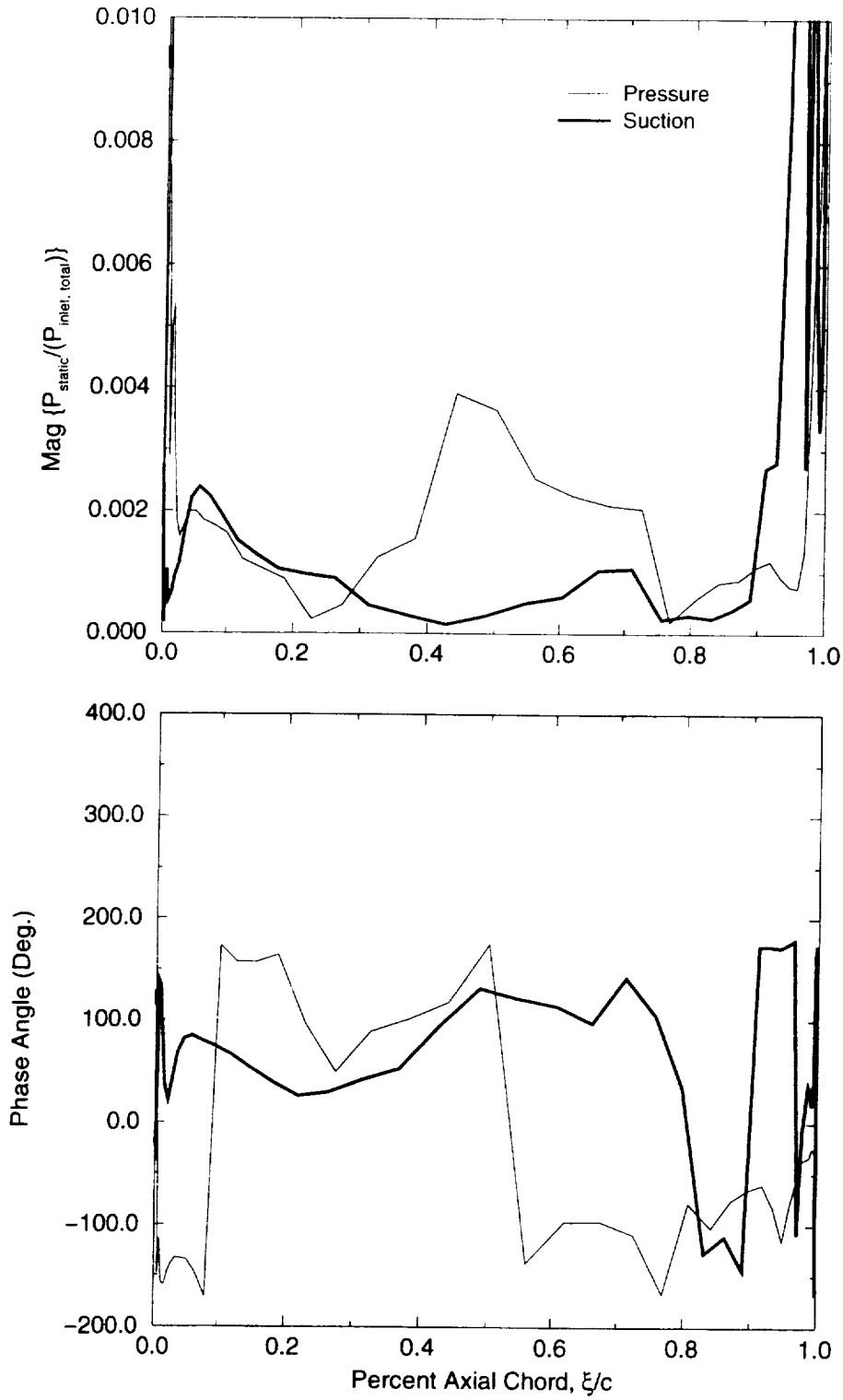

Figure 7.26: 2^{nd} harmonic unsteady blade surface pressure distributions obtained from inviscid *TURBO-AE* calculations at the 88% span location, *upper* magnitude, and *lower* phase at an interblade phase angle of degrees.

ADPAC results, the main difference being in the location of the shock structure. These differences are consistent with the change in flow due to the increased blockage in the viscous analysis. The unsteady response to a prescribed torsional motion was then investigated by comparing the nonlinear *TURBO-AE* and linear *SLiQ* predictions. Both the viscous *ADPAC+ SLiQ* and inviscid *TURBO-AE* flutter predictions indicated the fan would flutter at an operating point associated with a flutter condition in the rig. The inviscid *ADPAC+ SLiQ* flutter analysis however indicated that the fan was stable at this operating condition. The reason for the discrepancy between the inviscid *TURBO-AE* and inviscid *ADPAC+ SLiQ* solutions is not understood at this time. Based on the results obtained from this task it is concluded that *TURBO-AE* does predict the observed flutter behavior of the fan. However in order to obtain this result *TURBO-AE* had to be initialized using the inviscid *ADPAC* steady solution. The difficulty in getting a converged *TURBO-AE* steady flow that matched the rig measured flutter point is a drawback to its use in flutter prediction. Later versions of the code should address this problem.

References

[1] M.D. Rothrock, R.L. Jay, and R.E. Riffel. Time Variant Aerodynamics of High-turning Blade Elements. ASME Paper 81-GT-123, 1981.

[2] R.E. Riffel and M.D. Rothrock. Experimental Determination of Unsteady Blade Element Aerodynamics in Cascades. NASA Contractor Report CR-159831, June 1980.

[3] M.J. Janus. *Advanced 3-D CFD Algorithm for Turbomachinery.* PhD thesis, Mississippi State University, 1989.

[4] J.P. Chen. *Unsteady Three Dimensional Thin Layer Navier-Stokes Solutions for Turbomachinery in Transonic Flow.* PhD thesis, Mississippi State University, 1991.

[5] J.P. Chen and D.L. Whitfield. Navier-Stokes Calculations for the Unsteady Flowfield of Multi-stage Turbomachinery. AIAA Paper 93-0676, January 1993. 31th Aerospace Sciences Meeting and Exhibit, Reno, Nevada.

[6] B.S. Baldwin and H. Lomax. Thin Layer Approximation and Algebraic Model for Seperated Turbulent Flows. AIAA Paper 78-257, January 1978. 16th Aerospace Sciences Meeting, Huntsville, AL.

[7] M.A. Bakhle, R. Srivastava, G.L. Stefko, and M.J. Janus. Development of an Aeroelastic Code Based on an Euler/Navier-Stokes Aerodynamic Solver. ASME Paper 96-GT-311, 1996.

[8] M.A. Bakhle, R. Srivastava, T.G. Keith, and G.L. Stefko. A 3D Euler / Navier-Stokes Aeroelastic Code for Propulsion Applications. AIAA Paper 97-2749, 1997.

[9] W.S. Clark. *Investigation of Unsteady Viscous Flows in Turbomachinery Using a Linearized Navier-Stokes Analysis.* PhD thesis, Duke University, 1998.

[10] P.R. Spalart and S.R. Allmaras. A One Equation Turbulence Model for Aerodynamic Flows. AIAA Paper 92-0439, 1992.

[11] W.S. Clark and K.C. Hall. A Numerical Study of the Onset of Stall Flutter in Cascades. ASME Paper 95-GT-377, 1995.

[12] J.G. Marshall and M.B. Giles. Some Applications of a Time-Linearized Euler Method to Flutter and Forced Response in Turbomachinery. In *Unsteady Aerodynamics and Aeroelasticity of Turbomachines, Proceedings of the 8th International Symposium held in Stockholm, Sweden. Edited by T.H. Fransson*, pages 225–240. Kluwer Academic Publishers, Dordrecht, The Netherlands, 1997.

[13] E.J. Hall, N.J. Heidegger, and R.A. Delaney. ADPAC v1.0 - User's Manual. NASA Contractor Report CR-206600, 1998.

[14] A. Bölcs and T.H. Fransson. Aeroelasticity in Turbomachines Comparison of Theoretical and Experimental Cascade Results. Communication du laboratoire de thermique appliquee et de turbomachines, EPFL, Lausanne, Switzerland. 1986.

[15] V.R. Capece. Evaluation of Current State-Of-The-Art Unsteady Aerodynamic Models for the Prediction of Flutter and Forced Vibration Response. Guide consortium, carnegie mellon university, 1998.

[16] L.E. Snyder and D.W. Burns. Forced Vibration and Flutter Design Methodology. In *AGARD Manual on Aeroelasticity in Axial-Flow Turbomachines, Structural Dynamics and Aeroelasticity, AGARD-AG-298, Edited by M.F. Platzer and F.O. Carter*, volume 2, pages 22–1 – 22–28, 1988.

[17] F.O. Carta. Coupled Blade-Disk-Shroud Flutter Instabilities in Turbojet Engine Rotors. *Trans. ASME Journal of Engineering for Power*, 89A(3):419–426, July 1967.

[18] J.M. Verdon. Unsteady Aerodynamic Methods for Turbomachinery Aeroelastic and Aeroacoustic Applications. *AIAA Journal*, 31(2):235–250, 1993.

REPORT DOCUMENTATION PAGE

Form Approved
OMB No. 0704-0188

1. AGENCY USE ONLY (*Leave blank*)	2. REPORT DATE	3. REPORT TYPE AND DATES COVERED
	May 2001	Final Contractor Report

4. TITLE AND SUBTITLE

Application of TURBO-AE to Flutter Prediction
Aeroelastic Code Development

5. FUNDING NUMBERS

WU-708-28-13-00
NAS3-27725
Task 6

6. AUTHOR(S)

Daniel Hoyniak and Todd A. Simons

7. PERFORMING ORGANIZATION NAME(S) AND ADDRESS(ES)

Rolls-Royce Corporation
P.O. Box 420
Indianapolis, Indiana 46206–0420

8. PERFORMING ORGANIZATION REPORT NUMBER

EDR-19540

9. SPONSORING/MONITORING AGENCY NAME(S) AND ADDRESS(ES)

National Aeronautics and Space Administration
Washington, DC 20546–0001

10. SPONSORING/MONITORING AGENCY REPORT NUMBER

NASA CR—2001-210761

11. SUPPLEMENTARY NOTES

Project Manager, George Stefko, Structures and Ascoustics Division, NASA Glenn Research Center, organization code 5930, 216–433–3920.

12a. DISTRIBUTION/AVAILABILITY STATEMENT

Unclassified - Unlimited
Subject Category: 02 Distribution: Nonstandard

Available electronically at http://gltrs.grc.nasa.gov/GLTRS

This publication is available from the NASA Center for AeroSpace Information, 301–621–0390.

12b. DISTRIBUTION CODE

13. ABSTRACT ***(Maximum 200 words)***

The TURBO-AE program has been evaluated by comparing the obtained results to cascade rig data and to predictio made from various in-house programs. A high-speed fan cascade, a turbine cascade and a fan geometry that showe flutter in torsion mode were analyzed. The steady predictions for the high-speed fan cascade showed the TURBO-AE predictions to match in-house codes. However, the predictions did not match the measured blade surface data. Other researchers also reported similar disagreement with these data sets. Unsteady runs for the fan configuration were not successful using TURBO-AE. The turbine cascade results showed good agreement for steady data with those obtained from in-house codes and measurements. The unsteady pressure amplitudes were underpredicted by TURBO-AE as compared to data and in-house code, whereas the phase showed good agreement with in-house code and good to fair agreement with data. For the fan geometry, steady blade loading predictions showed good agreement with in-house code. Also, TURBO-AE successfully predicted the torsion mode flutter behavior that the in-house codes failed to predict.

14. SUBJECT TERMS

Turbomachinery; Aeroelasticity; Flutter; Computational

15. NUMBER OF PAGES

105

16. PRICE CODE

A06

17. SECURITY CLASSIFICATION OF REPORT	18. SECURITY CLASSIFICATION OF THIS PAGE	19. SECURITY CLASSIFICATION OF ABSTRACT	20. LIMITATION OF ABSTRACT
Unclassified	Unclassified	Unclassified	